



Applied Research Laboratory The Pennsylvania State University

12

POINT DEFECT STRUCTURE OF Cr_2O_3

by

M. Y. Su and G. Sinkovich

AD-A187 620

DTIC
ELECTE
NOV 20 1987
S
D

DISTRIBUTION STATEMENT A

Approved for public release
Distribution Unlimited

ARL

TECHNICAL REPORT

The Pennsylvania State University
APPLIED RESEARCH LABORATORY
P.O. Box 30
State College, PA 16804

DTIC
SELECTE
NOV 20 1987
S D

POINT DEFECT STRUCTURE OF Cr_2O_3

by

M. Y. Su and G. Zinkovich

Technical Report No. TR 87-008
October 1987

Supported by:
Naval Sea Systems Command

L. R. Hettche
Applied Research Laboratory

Approved for public release; distribution unlimited

87 11 14 025

AD-A187620

REPORT DOCUMENTATION PAGE				
1a. REPORT SECURITY CLASSIFICATION Unclassified			1b. RESTRICTIVE MARKINGS	
2a. SECURITY CLASSIFICATION AUTHORITY			3. DISTRIBUTION/AVAILABILITY OF REPORT (A) Unlimited	
2b. DECLASSIFICATION/DOWNGRADING SCHEDULE				
4. PERFORMING ORGANIZATION REPORT NUMBER(S) TR-87-00			5. MONITORING ORGANIZATION REPORT NUMBER(S)	
6a. NAME OF PERFORMING ORGANIZATION Applied Research Laboratory The Penna. State University		6b. OFFICE SYMBOL (If applicable) ARL	7a. NAME OF MONITORING ORGANIZATION Naval Sea Systems Command Department of the Navy	
6c. ADDRESS (City, State, and ZIP Code) P. O. Box 30 State College, PA 16804			7b. ADDRESS (City, State, and ZIP Code) Washington, DC 20362	
8a. NAME OF FUNDING/SPONSORING ORGANIZATION Naval Sea Systems Command		8b. OFFICE SYMBOL (If applicable) NAVSEA	9. PROCUREMENT INSTRUMENT IDENTIFICATION NUMBER N-00024-85-C-6041	
8c. ADDRESS (City, State, and ZIP Code) Department of the Navy Washington, DC 20362			10. SOURCE OF FUNDING NUMBERS	
			PROGRAM ELEMENT NO.	PROJECT NO.
			TASK NO.	WORK UNIT ACCESSION NO.
11. TITLE (Include Security Classification) POINT DEFECT STRUCTURE OF Cr_2O_3 (Unclassified)				
12. PERSONAL AUTHOR(S) M. Y. Su and G. Simkovich				
13a. TYPE OF REPORT Ph.D. Thesis		13b. TIME COVERED FROM TO	14. DATE OF REPORT (Year, Month, Day) October 1987	15. PAGE COUNT 165
16. SUPPLEMENTARY NOTATION				
17. COSATI CODES			18. SUBJECT TERMS (Continue on reverse if necessary and identify by block number)	
FIELD	GROUP	SUB-GROUP		
			Semiconductors, electrical conductivity, point defect structure, high temperature oxidation, thermoelectric power	
19. ABSTRACT (Continue on reverse if necessary and identify by block number)				
<p>Chromium oxide, Cr_2O_3 is of considerable technological importance because it provides a protective scale on important materials, such as stainless steels and superalloys; therefore, it is of interest to know its transport properties and how these properties may be altered. In order to obtain a better understanding of the defect structure of Cr_2O_3, the electrical conductivity and Seebeck coefficient of sintered high purity Cr_2O_3, TiO_2-doped Cr_2O_3 and MgO-doped Cr_2O_3 have been</p>				
20. DISTRIBUTION/AVAILABILITY OF ABSTRACT <input checked="" type="checkbox"/> UNCLASSIFIED/UNLIMITED <input type="checkbox"/> SAME AS RPT. <input type="checkbox"/> DTIC USERS			21. ABSTRACT SECURITY CLASSIFICATION Unclassified	
22a. NAME OF RESPONSIBLE INDIVIDUAL			22b. TELEPHONE (Include Area Code) 814/355-6344	22c. OFFICE SYMBOL ARL/PSU

SECURITY CLASSIFICATION OF THIS PAGE

measured as functions of temperature, oxygen partial pressure and different levels of dopant content. Results from these measurements show that the defect structure of Cr_2O_3 is relatively complicated. At high temperatures, depending upon the oxygen partial pressure different defects may present. In general, at high ^{phosphorous oxide} PO_2 , Cr_2O_3 is a P-type semiconductor with electron holes and chromium vacancies as the predominant defects; at intermediate PO_2 , Cr_2O_3 behaves as an intrinsic semiconductor with electrons and electron holes as the major defects; at low PO_2 , near the $\text{Cr}/\text{Cr}_2\text{O}_3$ equilibrium oxygen pressure, Cr_2O_3 changes to an N-type semiconductor with electrons and chromium interstitials as the dominant defects. Based on these results defect dependent properties, such as the parabolic growth of Cr_2O_3 during high temperature oxidation of Cr and the sintering of Cr_2O_3 , are discussed.

References →



Accession For	
NTIS	CRA&I <input checked="" type="checkbox"/>
DTIC	TAB <input type="checkbox"/>
Unannounced <input type="checkbox"/>	
Justification	
By	
Distribution	
Availability Codes	
Dist	Avail and/or Special
A-1	

ABSTRACT

Chromium oxide, Cr_2O_3 is of considerable technological importance because it provides a protective scale on important materials, such as stainless steels and superalloys; therefore, it is of interest to know its transport properties and how these properties may be altered. In order to obtain a better understanding of the defect structure of Cr_2O_3 , the electrical conductivity and Seebeck coefficient of sintered high purity Cr_2O_3 , TiO_2 -doped Cr_2O_3 and MgO -doped Cr_2O_3 have been measured as functions of temperature, oxygen partial pressure and different levels of dopant content. Results from these measurements show that the defect structure of Cr_2O_3 is relatively complicated. At high temperatures, depending upon the oxygen partial pressure different defects may present. In general, at high P_{O_2} , Cr_2O_3 is a P-type semiconductor with electron holes and chromium vacancies as the predominant defects; at intermediate P_{O_2} , Cr_2O_3 behaves as an intrinsic semiconductor with electrons and electron holes as the major defects; at low P_{O_2} , near the $\text{Cr}/\text{Cr}_2\text{O}_3$ equilibrium oxygen pressure, Cr_2O_3 changes to an N-type semiconductor with electrons and chromium interstitials as the dominant defects. Based on these results defect dependent properties, such as the parabolic growth of Cr_2O_3 during high temperature oxidation of Cr and the sintering of Cr_2O_3 , are discussed.

TABLE OF CONTENTS

	Page
ABSTRACT	iii
LIST OF TABLES	vii
LIST OF FIGURES	viii
ACKNOWLEDGEMENTS	xii
Chapter	
1 INTRODUCTION	1
1.1 Background Information	1
1.2 Research Objectives	2
1.3 Organization of the Thesis	2
2 THEORETICAL PRINCIPLES	4
2.1 Some General Aspects of Point Defects	4
2.2 Point Defect Theory	6
2.2.1 P-type Metal Deficit Semiconductor	8
2.2.2 N-type Metal Excess Semiconductor	9
2.2.3 Intrinsic Ionization of Electrons	9
2.2.4 Defect Structures Involving Both Cationic Vacancies and Interstitials	11
2.2.5 Effects of Impurities on Defect Equilibria	14
2.3 Electrical Conductivity	18
2.3.1 Electron and Electron Hole Concentrations	18
2.3.2 Electron and Electron hole Mobility	22
2.3.3 Electrical Conductivity and Point Defects	24
2.4 Seebeck Coefficient	26
2.5 Parabolic Scale Growth	29
3 LITERATURE REVIEW	35
3.1 Some General Aspects of Cr_2O_3	35

TABLE OF CONTENTS (continued)

Chapter		Page
	3.1.1 Thermodynamics of the Chromium-Oxygen System ...	35
	3.1.2 The Crystal Structure of Cr_2O_3	36
	3.2 Self-Diffusion in Cr_2O_3	38
	3.3 Sintering of Cr_2O_3	41
	3.4 High Temperature Oxidation of Chromium	43
	3.5 Electrical Conductivity and Seebeck Coefficient	46
	3.6 Summary	54
4	EXPERIMENTAL PROCEDURE	55
	4.1 Sample Preparation	55
	4.1.1 Sintering	56
	4.1.2 Atmosphere Control	56
	4.2 Sample Characterization	58
	4.3 Electrical Conductivity and Seebeck Coefficient Measurements	61
5	ELECTRICAL CONDUCTIVITY AND SEEBECK COEFFICIENT OF TiO_2 -DOPED Cr_2O_3	67
	5.1 Results	67
	5.1.1 Experimental Equilibrium Time	67
	5.1.2 Electrical Conductivity	68
	5.1.3 Seebeck Coefficient	74
	5.2 Analyses and Discussions	74
	5.2.1 Point Defect Structure of Cr_2O_3	74
	5.2.2 Defect Structure of TiO_2 -Doped Cr_2O_3	78
	5.2.3 Determination of the Intrinsic Electron Concentration n_i	83
	5.2.4 Construction of the Defect Concentration vs Oxygen Partial Pressure Diagram	85
	5.3 Summary	88
6	ELECTRICAL CONDUCTIVITY AND SEEBECK COEFFICIENT OF MgO -DOPED Cr_2O_3	94
	6.1 Results	94
	6.1.1 Solubility limit of MgO in Cr_2O_3	94
	6.1.2 Electrical Conductivity and Seebeck Coefficient	95

TABLE OF CONTENTS (continued)

Chapter	Page
6.2 Analyses and Discussions	100
6.2.1 Defect Structure of MgO-doped Cr ₂ O ₃	100
6.2.2 Calculation of Electron Hole Mobility	104
6.2.3 Construction of the Defect Concentration vs. Oxygen Pressure Diagram	107
6.3 Summary	108
7 POINT DEFECT STRUCTURE OF Cr ₂ O ₃	114
7.1 Point Defect Structure of Cr ₂ O ₃	114
7.2 Electrical Conductivity and Seebeck Coefficient of Cr ₂ O ₃	116
7.2.1 Electronic Conduction Mechanism	116
7.2.2 Electrical Conductivity and Seebeck Coefficient	118
7.3 Self Diffusion Coefficient of Cr in Cr ₂ O ₃	119
7.4 High Temperature Oxidation of Cr	128
7.5 Sintering of Cr ₂ O ₃	132
8 SUMMARY AND SUGGESTIONS FOR FUTURE RESEARCH	134
8.1 Summary of the results	134
8.2 Suggestions for Future Research	135
BIBLIOGRAPHY	137
Appendix A: COMPUTER PROGRAM FOR RESISTANCE MEASUREMENT	142
Appendix B: COMPUTER PROGRAM FOR SEEBECK COEFFICIENT MEASUREMENT	146

LIST OF TABLES

	Page
1. The listed purity of the raw material used in this study	55
2. Calculated defect concentrations as functions of different equilibrium constants	82
3. Mobilities of electrons and electron holes	85
4. Table of calculated intrinsic electron concentration n_i and the correspondence equilibrium K_i	85

LIST OF FIGURES

	Page
2.1 Compilation of the relationships between the point defect structure and the transport properties of crystalline solid.	7
2.2 Oxygen partial pressure dependence of the defect concentrations	10
2.3 Oxygen partial pressure dependence of the defect contrations for defect structure containing both cationic vacancies and interstitials.	15
2.4 The impurity effect on the defect structure of a P-type semiconductor	17
2.5 Schematic illustration of the energy band diagram for a semiconductor	20
2.6 Oxygen partial pressure dependence of the electrical conductivity of different defect structures	25
2.7 Seebeck effect of a semiconductor	27
2.8 Oxygen partial pressure dependence of the Seebeck coefficient of different defect structure	30
2.9 Oxygen partial pressure dependence of the parabolic rate constant of different defect structures	33
3.1 The crystal structure of Cr_2O_3	37
3.2 Comparison of diffusion coefficients in Cr_2O_3	40
3.3 Final density of Cr_2O_3 as a function of sintering atmosphere	42
3.4 Arrhenius plot of reported parabolic rate constants for the oxidation of pure Cr	44
3.5 Electrical conductivity of Cr_2O_3	48
3.6 Variation of electrical conductivity of Cr_2O_3 with $1/T$ for a range of oxygen pressures	49
3.7 Variation of thermoelectric power of Cr_2O_3 with temperature for a range of oxygen pressures	51
4.1 The final density of sintered samples of Cr_2O_3 as a function of the oxygen partial pressure	57
4.2 Oxygen pressures (atm) as a function of temperature and CO_2/CO ratios at a total pressure of 1 atm	59

LIST OF FIGURES (continued)

	Page
4.3 Entire gas atmosphere preparation arrangement.	60
4.4 Experimental arrangement for the electrical conductivity and Seebeck coefficient measurements.	62
4.5 Block diagram of the apparatus of the Seebeck coefficient measurement.	64
4.6 Determination of Seebeck coefficient from experimental data	65
5.1 Kinetic diagram of measured resistance of a porous Cr_2O_3 sample.	69
5.2 Electrical conductivity of TiO_2 -doped Cr_2O_3 at 1000°C	70
5.3 Electrical conductivity of TiO_2 -doped Cr_2O_3 at 1100°C	71
5.4 Electrical conductivity of TiO_2 -doped Cr_2O_3 at 1200°C	72
5.5 Electrical conductivity of TiO_2 -doped Cr_2O_3 at 1300°C	73
5.6 Electrical conductivity of TiO_2 -doped Cr_2O_3 as a function of temperature.	75
5.7 Seebeck coefficient of TiO_2 -doped Cr_2O_3 at 1200°C	76
5.8 Seebeck coefficient of TiO_2 -doped Cr_2O_3 as a function of temperature.	77
5.9 A model of the defect structure of TiO_2 -doped Cr_2O_3	81
5.10 Temperature dependence of the conductivity minimum and the calculated n_i	86
5.11 Temperature dependence of the electrical conductivity and the calculated mobilities.	87
5.12 Defect concentrations vs. oxygen partial pressure diagram of TiO_2 -doped Cr_2O_3 at 1000°C	89
5.13 Defect concentrations vs. oxygen partial pressure diagram of TiO_2 -doped Cr_2O_3 at 1100°C	90
5.14 Defect concentrations vs. oxygen partial pressure diagram of TiO_2 -doped Cr_2O_3 at 1200°C	91
5.15 Defect concentrations vs. oxygen partial pressure diagram of TiO_2 -doped Cr_2O_3 at 1300°C	92

LIST OF FIGURES (continued)

		Page
5.16	Point defect structure of pure Cr_2O_3 in the high oxygen partial pressure at 1100°C	93
6.1	Lattice parameters of MgO-doped Cr_2O_3	96
6.2	The X-ray powder diffraction patterns of MgO-doped Cr_2O_3	97
6.3	Oxygen partial pressure dependence of the electrical conductivity of MgO-doped Cr_2O_3 at 1300°C	98
6.4	Oxygen partial pressure dependence of the Seebeck coefficient of MgO-doped Cr_2O_3 at 1300°C	99
6.5	Oxygen partial pressure dependence of the electrical conductivity of 0.3mole% MgO-doped Cr_2O_3 at different temperatures	101
6.6	Oxygen partial pressure dependence of the Seebeck coefficient of 0.3mole% MgO-doped Cr_2O_3 at different temperatures	102
6.7	A model for the defect structure of MgO-doped Cr_2O_3	105
6.8	Temperature dependence of the electron hole mobility	106
6.9	Defect concentration vs. oxygen pressure diagram for MgO-doped Cr_2O_3 at 1100°C	109
6.10	Defect concentrations vs. oxygen pressure diagram for MgO-doped Cr_2O_3 at 1200°C	110
6.11	Defect concentrations vs oxygen pressure diagram for MgO-doped Cr_2O_3 at 1300°C	111
6.12	Defect concentrations vs oxygen pressure diagram for pure Cr_2O_3 in low oxygen partial pressure at 1100°C	112
7.1	Defect concentrations vs. oxygen partial pressure diagram for pure Cr_2O_3 at 1100°C	115
7.2	Defect concentrations vs. oxygen partial pressure diagram for pure Cr_2O_3 at temperatures between 1000° to 1600°C	117
7.3	Electrical conductivity vs. oxygen partial pressure diagram for pure Cr_2O_3 at temperatures between 1000° to 1600°C	120
7.4	Seebeck coefficient vs. oxygen partial pressure diagram for pure Cr_2O_3 at temperatures between 1000° to 1600°C	121
7.5	Experimental results of the electrical conductivity of pure Cr_2O_3 at temperatures between 1000° to 1400°C	122

LIST OF FIGURES (continued)

	Page
7.6 Seebeck coefficient vs. oxygen partial pressure diagram for pure Cr_2O_3 at temperatures between 1000° to 1600°C	123
7.7 Calculated diffusion coefficient vs. oxygen partial pressure diagram for pure Cr_2O_3 at 1100°C	125
7.8 Effect of higher valent cations on the diffusion coefficient of Cr in Cr_2O_3 at 1100°C	126
7.9 Effect of lower valent cations on the diffusion coefficient of Cr in Cr_2O_3 at 1100°C	127
7.10 Calculated parabolic rate constant vs. oxygen partial pressure diagram for pure Cr_2O_3 at 1100°C	129
7.11 Effect of higher valent cations on the parabolic rate constant of the growth of Cr_2O_3 at 1100°C	130
7.12 Effect of lower valent cations on the parabolic rate constant of the growth of Cr_2O_3 at 1100°C	131
7.13 Oxygen partial pressure dependence of the concentration of oxygen vacancies in Cr_2O_3 at 1600°C	133

ACKNOWLEDGEMENTS

The author wishes to express his sincere gratitude to his thesis advisor, Dr. George Simkovich, Professor of Materials Science and Engineering, for leading him into the field of thermodynamics and brightening him with the beauty of science. The persistent guidance and encouragement throughout this research work are also grateful.

Appreciation is also extended to Professors. W. Bitler, E. Ryba and R. H. Good for serving on the thesis committee. Helpful discussions with the author's research colleagues during the process of his study are also appreciated.

This research was supported by the Naval Sea System Command and the Applied Research Laboratory Exploratory and Foundational Research Program, the Pennsylvania State University. This support is greatly acknowledged.

The author would also like to thank Ms. S. L. Yin, an old friend of his since 1974, who motivated and encouraged the author for pursuing higher education during their younger age.

Finally, the author's deepest appreciation goes to his parents for their generous support and encouragement during the course of his entire education.

Chapter 1

INTRODUCTION

1.1 Background Information

The work presented in this thesis is concerned with the determination of the point defect structure of Cr_2O_3 . Several factors account for the reasons of the whole investigation.

Chromium sesquioxide (Cr_2O_3) is an oxide of extreme importance, mainly because it grows as a film on stainless steel and other technological alloys at elevated temperatures and protects the alloy with considerable resistance against rapid oxidation and corrosion. It has been known that small additions of impurities or active elements in either the metal or oxide may have significant effects on the oxidation rate of the metal. In order to elucidate the oxidation mechanism and the effects of the additions, it is necessary to know the transport properties of Cr_2O_3 and the manner in which these properties may be varied.

Recently, the rapid growth in the development of electrical conduction related devices (e.g., chemical and temperature sensors) for applications at elevated temperatures and severe environments has attracted many studies on the electrical properties of transition metal oxides. Chromium oxide with its high melting temperature, excellent corrosion resistance and behavior as a semiconductor appears to be a good candidate. It has also been found that many factors such as oxygen activity, temperature and the amount of dopant may have decisive influence on the electrical properties of these oxides. Therefore, studies of the electronic conduction mechanism of Cr_2O_3 and the effects of the various factors become of interest.

Furthermore, it has been found that a correct atmosphere control is very important during the sintering of Cr_2O_3 containing refractories. The theories of the sintering mechanism of Cr_2O_3 have not yet been fully understood.

Since all these properties, sintering, electronic conduction and atomic transport in oxidation are very closely related to the point defects present in the oxide, a complete knowledge of the point defect structure of the oxide is essential for understanding and improving these properties.

1.2 Research Objectives

This research work was undertaken with the following objectives.

- (1) To determine the point defect structure of Cr_2O_3 , that is,
 1. to deduce the types of point defects that occur in Cr_2O_3 .
 2. to examine the temperature and oxygen partial pressure dependence of the concentrations of these defects.
- (2) To determine the conduction mechanism of the electronic species in Cr_2O_3 .
- (3) To investigate the impurity effect on the defect structure of Cr_2O_3 .
- (4) To explain the high temperature oxidation mechanism of Cr_2O_3 .

1.3 Organization of the Thesis

The research work carried out is presented in this thesis in eight chapters. Chapter 1 gives a brief introduction of the research work and the thesis layout.

Chapter 2 describes theoretical principles pertaining to the point defect chemistry, electrical conductivity, the Seebeck coefficient, and other defect related properties of Cr_2O_3 .

Chapter 3 reviews the literature concerning the different physical and chemical properties of Cr_2O_3 that are related to its point defect structure.

Chapter 4 describes the experimental apparatus and procedures. Which includes sample preparation and characterization, and electrical conductivity and Seebeck coefficient measurements.

Results obtained from various types of experiments are discussed in Chapter 5 to 7. Chapter 5 presents the results of TiO_2 -doped Cr_2O_3 , Chapter 6 presents the results of MgO -doped Cr_2O_3 , and Chapter 7 presents the results of pure Cr_2O_3 .

The entire work is summarized in Chapter 8 along with suggestions for future research.

Chapter 2

THEORETICAL PRINCIPLES

It is desirable to discuss some basic theories about point defect structures and their related transport properties since such is the basis of this research. This chapter is organized into five sections. Section 1 gives some general descriptions about point defects and their relation to different transport properties in crystalline solids. Section 2 discusses the thermodynamics of point defects. Examples of point defect equilibrium based on the Me_2O_3 system are also examined. In section 3 and 4, theories of the electrical conductivity and Seebeck coefficient, respectively, are discussed more extensively in order to show how measurements of these two properties can be used to reveal the defect structure and the conduction mechanism of a particular material. Finally, the mechanism of the parabolic growth of oxides is briefly described in section 5.

2.1 Some General Aspects of Point Defects

The structure of an ideal crystalline solid is characterized by an orderly periodic arrays of atoms. In theory, the crystal lattice may have infinite repetition without any disturbance throughout the crystal. However, in real crystals, the periodic structure is always disturbed by some structural imperfections or defects. There are several types of such structural defects, and these are commonly categorized into three main groups, namely, 1) point defects, 2) line defects, and 3) planar defects. Numerous discussions on these subjects can be found in the literature (1-8). Among these imperfections, point defects are the most important defect species because of their strong relation to the transport properties in crystalline solids.

When the imperfection is limited to one structural or lattice site and its immediate vicinity, the imperfection is termed a point defect. Different types of point defects may occur in crystals and these are:

- (1) vacancies; these are sites where constituent atoms are missing from a normally occupied position.
- (2) interstitials; these are sites where atoms occupy the interstices between the regular lattice sites.
- (3) misplaced atoms; these are sites where one type of atom is found at a site normally occupied by another.
- (4) impurity atoms; these may occupy normally unoccupied positions (interstitial type) or positions normally occupied by one of the host atoms (substitutional type).

In addition to these atomic defects, there are electronic defects;

- (5) free electrons and electron holes; these may either be formed intrinsically through ionization of an electron from the valence to the conduction band or be formed in association with atomic defects.

Furthermore, interactions between these basic types of point defects may also occur, e.g. associates and clusters.

In a crystalline solid, the concentration of point defects is strongly dependent upon temperature, pressure and the chemical potentials of the crystal components. In general, the complete description of the point defects in a compound and their concentration variation as a function of temperature and partial pressure of the constituent atoms or molecules is termed the point defect structure of the compound (4).

Closely related to the point defect structure are some important and interesting properties of crystalline solids. A compilation of the relationships is

illustrated in Figure 2.1. For the point defect dependent properties, atomic defects are responsible for nonstoichiometry and solid state diffusion with the compound. Solid state diffusion, in turn, determines or strongly influences properties or processes such as solid state reaction, ionic conductivity, sintering, high temperature creep, etc.. And electronic defects determine properties such as electrical conductivity, thermoelectric power (Seebeck coefficient), Hall coefficient, etc.. For mass transport in electrochemical potential gradients occurring, for example, during relaxation of the concentrations of point defects or during parabolic scale growth, the migration of ions is generally determined by the mobility of both atomic and electronic defects.

Theoretically, with a priori knowledge of the point defect structure of a compound, one may predict the different transport properties occurring in the compound. Improvements or alterations of these properties can then be achieved by simply modifying the defect structure. Conversely, from directly measurable quantities characterizing the transport properties, one may reveal the defect structure of the compound. In this study, two type of measurable properties, electrical conductivity and Seebeck coefficient, were utilized to achieve this objective.

2.2 Point Defect Theory

A useful tool to quantitatively describe the relationships between the different defect concentrations and the thermodynamic variables is given by point defect thermodynamics, also denoted as the point defect theory. In this section, several examples of defect equilibria are demonstrated to show how this theory is applied to different situations. In view of the many types of defects that may be

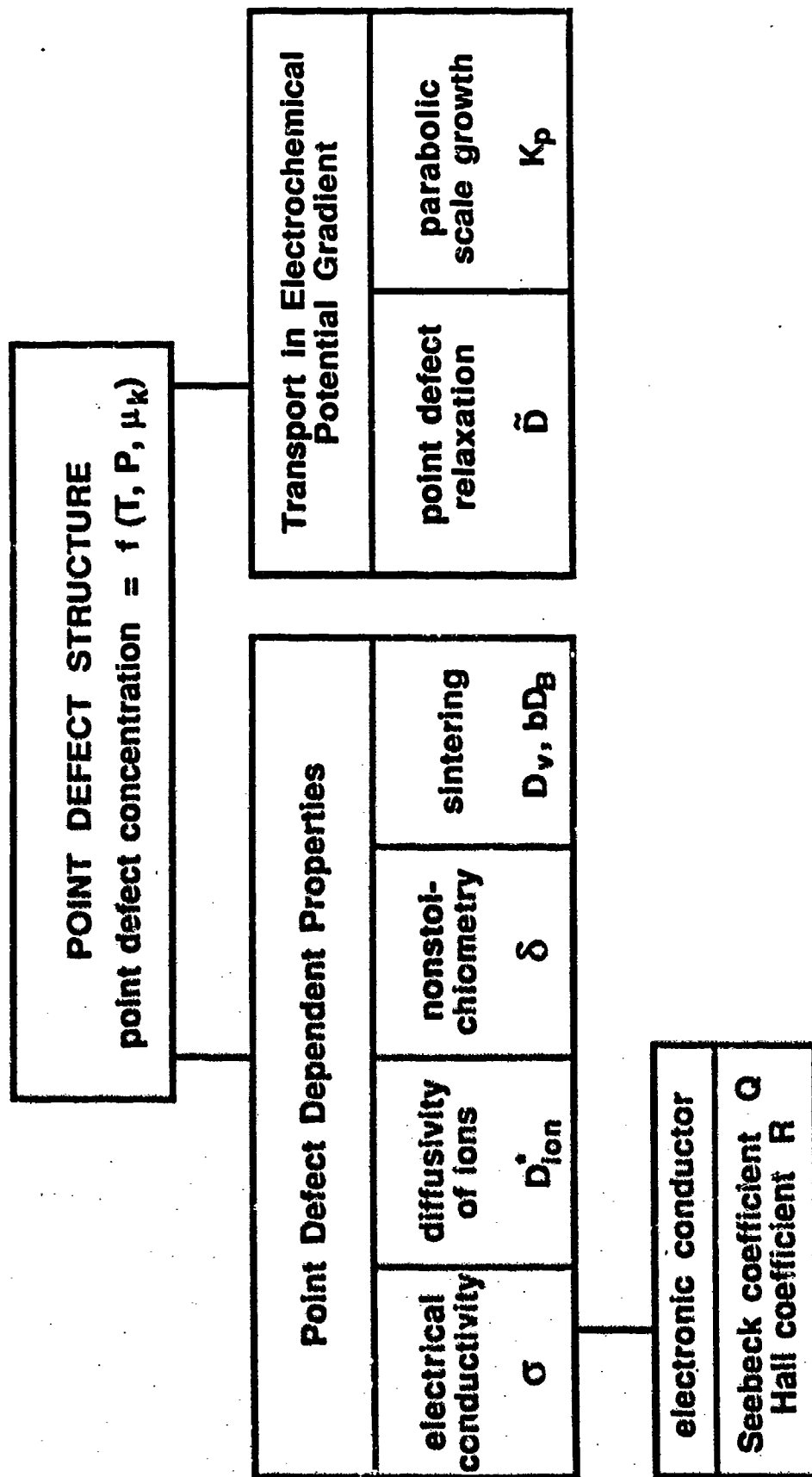


Figure 2.1: Compilation of the relationships between the point defect structure and the transport properties of crystalline solid.

formed and the numerous defect equilibria that may occur in different materials, the examples given will be restricted to systems of binary oxides containing transition metals.

It is generally agreed that in oxides containing transition metals, the predominating defects are nonstoichiometry defects, and these defects are either an excess or a deficit of cations or anions. If the predominating types of defects are charged, complementary electronic defects are created in order to conserve electrical neutrality. The extent of nonstoichiometry and the defect concentrations are usually functions of temperature and partial pressure of their constituents.

In the following discussions, different cases of defect equilibria are presented. It is assumed that in an oxide Me_2O_3 , the major defects essentially occur only in the cationic sublattice and these atomic defects are completely ionized.

2.2.1 P-type Metal Deficit Semiconductor

In metal deficit oxides where the deviation from nonstoichiometry δ is positive, metal vacancies and complementary electron holes may be formed through the reaction of oxygen with the oxide. The defect formation relation can be expressed as



For small defect concentrations the activities of the defects can be replaced by their concentrations and the equilibrium constant is given by

$$KV_{Me}'' = [V_{Me}']^2 \cdot [h']^6 \cdot P_{O_2}^{-3/2} \quad (2.2)$$

and the electroneutrality condition gives

$$[h'] = 3[V_{Me}'] \quad (2.3)$$

By solving Equations. 2.2 and 2.3, it is found

$$\delta = [V_{Me}^{''}] = 1/3 [h^{\cdot}] = 3^{-3/4} \cdot K_{V_{Me}^{''}}^{1/8} \cdot P_{O_2}^{3/16} \quad (2.4)$$

Shown in Figure 2.2(a) is the oxygen partial pressure dependence of the defect concentrations as illustrated by a plot of $\log[V_{Me}^{''}]$ vs $\log P_{O_2}$. A straight line of a positive slope of 3/16 characterizes the P-type metal-deficit behavior of Me_2O_3 type compounds.

2.2.2 N-type Metal Excess Semiconductor

In metal excess oxides, $\delta < 0$, the major defects are cation interstitials and electrons, and the defect equation is given as



The equilibrium constant of Equation 2.5 is

$$K_{Me_i^{''}} = [Cr_i^{''}]^2 \cdot [e^{\cdot}]^6 \cdot P_{O_2}^{3/2} \quad (2.6)$$

Combining with the electroneutrality equation

$$[e^{\cdot}] = [Me_i^{''}] \quad (2.7)$$

one obtains

$$\delta = [Me_i^{''}] = 1/3[e^{\cdot}] = 3^{-3/4} \cdot K_{Me_i^{''}}^{1/8} \cdot P_{O_2}^{-3/16} \quad (2.8)$$

In this case, the defect structure is characterized by a straight line of a negative slope -3/16 on the plot of $\log [Me_i^{''}]$ vs $\log P_{O_2}$ (Figure 2.2(b).)

2.2.3 Intrinsic Ionization of Electrons

In addition to the electronic defects that are created in association with the formation of the atomic defects, electronic defects are also formed through intrinsic ionization of electrons. In this process, electrons are excited from the valence band to the conduction band, and leave electron holes in the valence band.

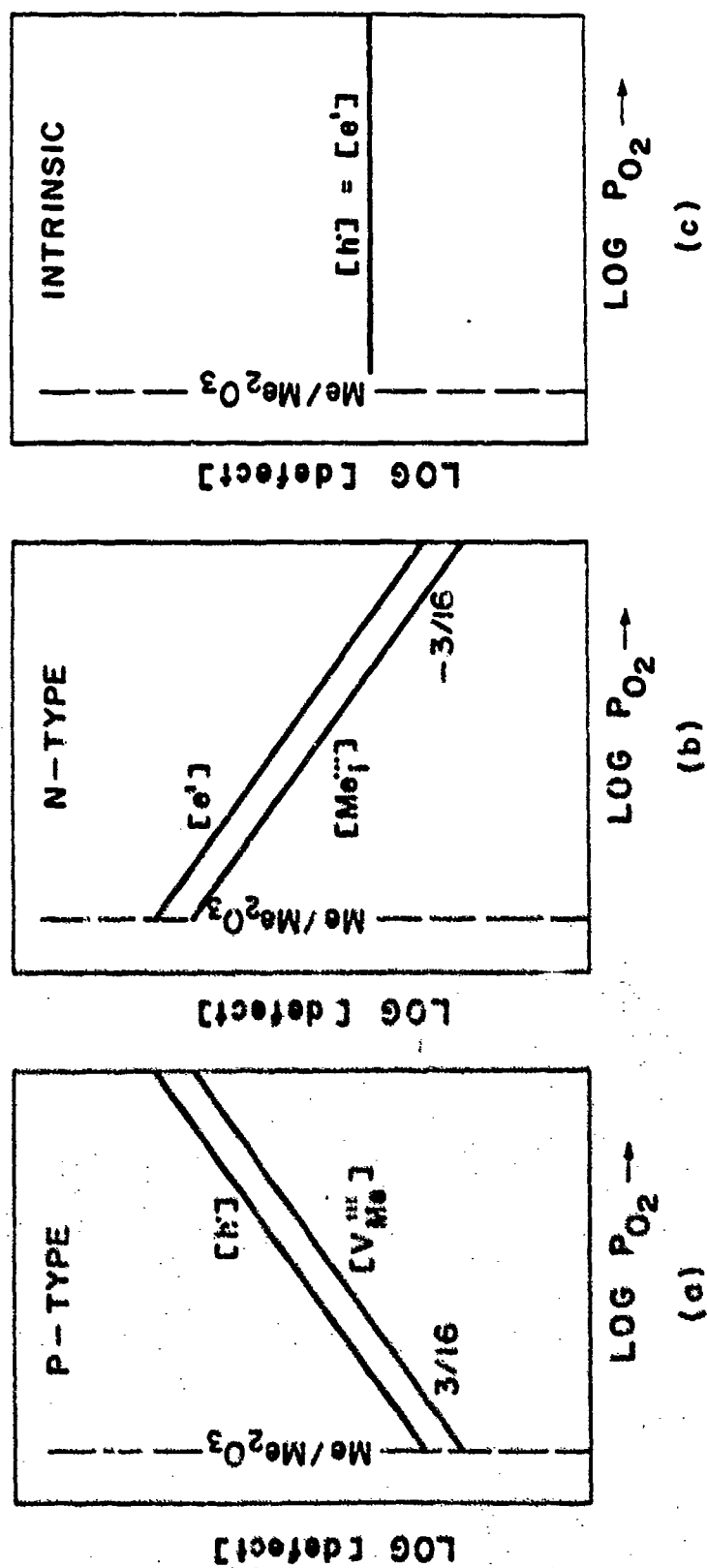


Figure 2.2: Oxygen partial pressure dependence of the defect concentrations.
 (a) P-type (b) N-type (c) Intrinsic Semiconductors.

The defect equilibrium can be expressed as

$$\text{Null} = e' + h' \quad (2.9)$$

$$K_i = [e'] \cdot [h'] \quad (2.10)$$

and the electroneutrality condition is

$$[e'] = [h'] = K_i^{1/2} \quad (2.11)$$

In this case, the concentrations of electrons and electron holes are not functions of oxygen partial pressure (Figure 2.2(c)).

2.2.4 Defect Structures Involving Both Cationic Vacancies and Interstitials

In the preceding considerations the oxide has been assumed to have a single type of defect with either a cation deficit or a cation excess as predominant throughout the whole P_{O_2} range. In many oxides, depending on the partial pressure of oxygen different types of defects may in principle occur. As an illustration a special case where an oxide containing metal vacancies at high P_{O_2} and metal interstitials at low P_{O_2} will be considered. In the intermediate P_{O_2} region the oxide will be stoichiometric or close to stoichiometric. The system $Me_{2.5}O_3$ and the assumption of complete ionization of the defects are still used. In this case the following defect equilibria need to be considered :



$$\text{Null} = e' + h' \quad (2.14)$$



The corresponding equilibrium constants are

$$K_{V_{Me}'''} = [V_{Me}''']^2 \cdot [h']^6 \cdot P_{O_2}^{-3/2} \quad (2.16)$$

$$K_{Me_i'''} = [Me_i''']^2 \cdot [e']^6 \cdot P_{O_2}^{3/2} \quad (2.17)$$

$$K_i = [e'] \cdot [h'] \quad (2.18)$$

$$K_F = [V_{Me}'''] \cdot [Me_i'''] \quad (2.19)$$

It should be noted that the above defect equilibria are interrelated, and it may be shown that $K_i^6 \cdot K_F^2 = K_{V_{Me}'''} \cdot K_{Me_i'''}$ through a combination of the equations.

Now the electroneutrality equation becomes more complicated and is given as

$$[h'] + 3[Me_i'''] = [e'] + 3[V_{Me}'''] \quad (2.20)$$

At high P_{O_2} , where the metal vacancy defect is predominant, the electroneutrality equation is reduced to

$$[V_{Me}'''] = 1/3[h'] \gg [Me_i'''], [e'] \quad (2.21)$$

and the defect concentrations are given by

$$[V_{Me}'''] = 1/3[h'] = 3^{-3/4} \cdot K_{V_{Me}'''}^{1/8} \cdot P_{O_2}^{3/16} \quad (2.22)$$

$$[Me_i'''] = 3^{3/4} \cdot K_F \cdot K_{V_{Me}'''}^{-1/8} \cdot P_{O_2}^{-3/16} \quad (2.23)$$

$$[e'] = 3^{1/4} \cdot K_i \cdot K_{V_{Me}'''}^{-1/8} \cdot P_{O_2}^{-3/16} \quad (2.24)$$

By combining Equations 2.21 to 2.23, it may be seen that the condition $[V_{Me}'''] \gg [Me_i''']$ may be replaced by $P_{O_2} \gg 3^4 \cdot K_F^{8/3} \cdot K_{V_{Me}'''}^{-2/3}$.

At low P_{O_2} , where the metal excess is predominant. The condition

$$[Me_i'''] = 1/3[e'] \gg [V_{Me}'''], [h'] \quad (2.25)$$

is applied and the following relations will be obtained.

$$[Me_i'''] = 1/3[e'] = 3^{-3/4} \cdot K_{Me_i'''}^{1/8} \cdot P_{O_2}^{-3/16} \quad (2.26)$$

$$[V_{Me}'''] = 3^{3/4} \cdot K_F \cdot K_{Me_i'''}^{-1/8} \cdot P_{O_2}^{3/16} \quad (2.27)$$

$$[h] = 3^{-1/4} \cdot K_i \cdot K_{Mei} \dots^{-1/8} \cdot P_{O_2}^{3/16} \quad (2.28)$$

Combining Equations 2.25 to 2.27, shows that the condition

$$[Me_i^{\prime\prime}] \gg [V_{Me}^{\prime\prime\prime}] \text{ is equal to } P_{O_2} \ll 3^4 \cdot K_F^{3/8} \cdot K_{Mei} \dots^{-2/3}$$

At or close to stoichiometry, the following limiting conditions must be considered.

Case I. Intrinsic ionization predominates, thus

$$[h] = [e] = K_i^{1/2} \gg [V_{Me}^{\prime\prime\prime}], [Me_i^{\prime\prime}] \quad (2.29)$$

Since $[h]$ and $[e]$ are independent of P_{O_2} , the point defect concentrations are given by

$$[V_{Me}^{\prime\prime\prime}] = K_i^{-3/2} \cdot K_{VMe}^{\prime\prime\prime 1/2} \cdot P_{O_2}^{3/4} \quad (2.30)$$

$$[Me_i^{\prime\prime}] = K_i^{-3/2} \cdot K_{Mei} \dots^{1/2} \cdot P_{O_2}^{-3/4} \quad (2.31)$$

Case II. Internal disorder (Frenkel defects) dominates, and thus

$$[V_{Me}^{\prime\prime\prime}] = [Me_i^{\prime\prime}] = K_F^{1/2} \gg [h], [e] \quad (2.32)$$

$[V_{Me}^{\prime\prime\prime}]$ and $[Me_i^{\prime\prime}]$ are now independent of P_{O_2} , while the concentrations of electronic defects are given by

$$[h] = K_F^{-1} \cdot K_{VMe}^{\prime\prime\prime 1/6} \cdot P_{O_2}^{1/4} \quad (2.33)$$

$$[e] = K_F^{-1} \cdot K_{Mei} \dots^{1/6} \cdot P_{O_2}^{-1/4} \quad (2.34)$$

Case III. A very special situation occurs when

$$[V_{Me}^{\prime\prime\prime}] = [Me_i^{\prime\prime}] = 1/3 [h] = 1/3 [e] \quad (2.35)$$

Combining Equations 2.16 to 2.19 and 2.35, shows that

$$K_i = 9K_F \quad (2.36)$$

In this case, a degenerate situation of case I and II occurs. The intermediate P_{O_2} region disappears and the high P_{O_2} metal deficit region joins with the low P_{O_2} metal excess region at a $P_{O_2} = (K_{Mei} \dots / K_{VMe}^{\prime\prime\prime})^{1/3}$.

In Figure 2.3, the variations of the point defect concentrations with oxygen partial pressure for the three cases are illustrated. It is quite clear that case I and III behave essentially as pure electronic conductors at all P_{O_2} . However in case II, the oxide may exhibit appreciable ionic conductivity at or close to stoichiometry.

2.2.5 Effects of Impurities on Defect Equilibria

In the previous examples discussion has been limited to pure materials and no account has been taken of impurities and their effects on defect equilibria. Under real conditions the impurities may have significant effects on the defect concentrations of the crystal. When impurities are incorporated into a crystal, they may occupy either the normal cation or anion lattice sites or interstitial sites depending upon the energy involved. In general, the incorporation at interstitial sites is possible only when the foreign atoms have a relatively smaller size than the native atoms. When foreign atoms are incorporated substitutionally, the difference in valence between impurity and native atoms will strongly affect the electroneutrality condition of the crystal. If the valence of the impurity is greater than that of the substituted atom, the impurity will behave as a donor; if the valence is smaller, the impurity will behave as an acceptor. In the following, the impurity effect is illustrated by adding either higher valent cations or lower valent cations to a metal-deficit oxide.

Case 1. Effect of higher valent cation impurity.

It has been mentioned that in a metal-deficit oxide $Me_{2-\delta}O_3$ with predominant metal vacancies the defect equilibrium can be expressed as



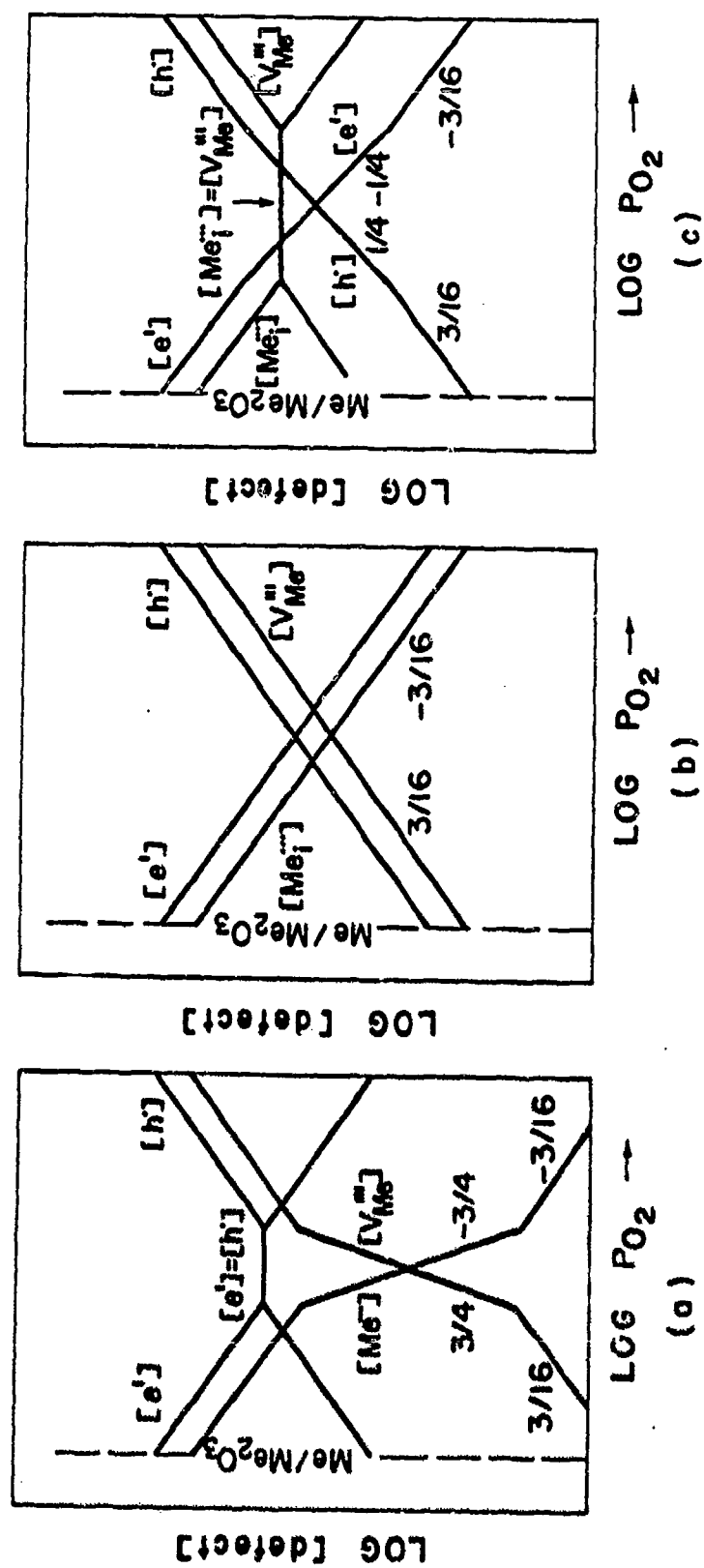
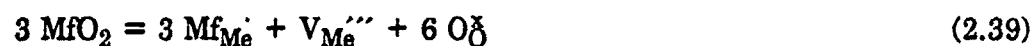


Figure 2.3: Oxygen partial pressure dependence of the defect concentrations for defect structure containing both cationic vacancies and interstitials.

$$K_{V_{Me}'''} = [V_{Me}''']^2 \cdot [h']^6 \cdot P_{O_2}^{-3/2} \quad (2.38)$$

The incorporation of a higher valent cation Mf^{4+} can be represented by the reaction



$$K_{Mf_{Me}} = 3 [Mf_{Me}] + [V_{Me}'''] \quad (2.40)$$

In this case, the impurity behaves as a donor. A positive charge and a metal vacancy are created by the substitution of an Mf^{4+} ion in the Me^{3+} site. The electroneutrality condition becomes

$$[h'] + [Mf_{Me}] = 3[V_{Me}'''] \quad (2.41)$$

In regions where $[Mf_{Me}] \gg [h']$, the amount of the impurity will then control the concentration of the metal vacancy, that is,

$$[V_{Me}'''] = 1/3[Mf_{Me}] = \text{constant} \quad (2.42)$$

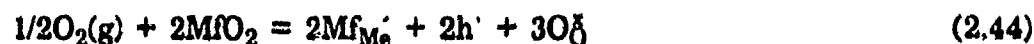
Combining with Equation 2.38, one obtains

$$[h'] \propto P_{O_2}^{1/4} \quad (2.43)$$

The results are illustrated in Figure 2.4(a).

Case 2. Effect of lower valent cation impurities.

When a lower valent cation impurity Mf^{2+} substitutes for Me^{3+} in the oxide $Me_{2.5}O_3$, the following reaction occurs



$$K_{Mf_{Me}} = [Mf_{Me}]^2 \cdot [h']^2 \cdot P_{O_2}^{-1/2} \quad (2.45)$$

In this case, a negative charge and an electron hole are created. The electroneutrality equation gives

$$[h'] = [Mf_{Me}] + 3[V_{Me}'''] \quad (2.46)$$

In regions where $[Mf_{Me}] \gg 3[V_{Me}''']$, the impurity content controls the concentration of the electronic species $[h']$.

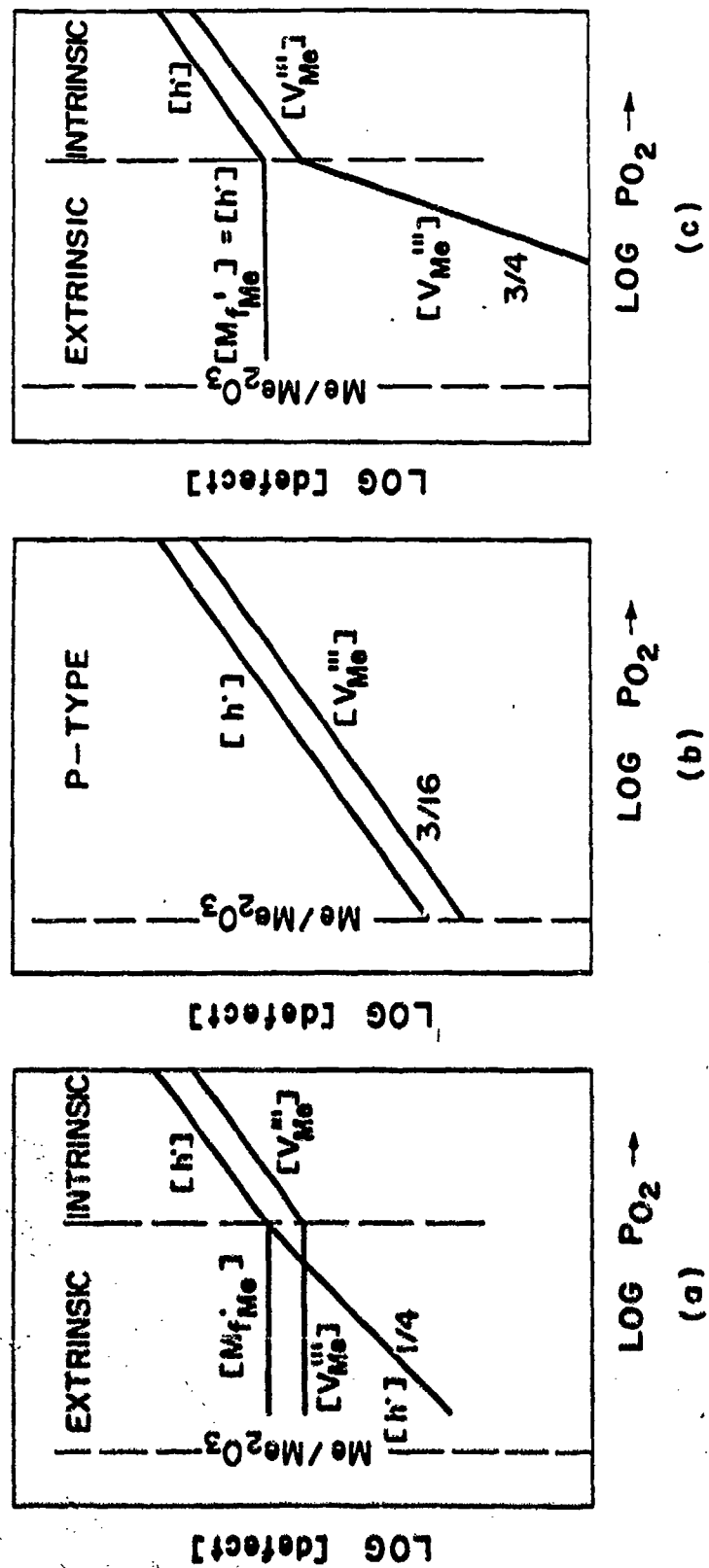


Figure 2.4: The impurity effect on the defect structure of a P-type semiconductor. (a) with higher valent cation impurity (b) with no impurity (c) with lower valent cation impurity.

$$[h'] = [Mf_{Me}'] = \text{constant} \quad (2.47)$$

Substituting into (Equation 2.38) gives

$$[V_{Me}'] \propto P_{O_2}^{3/4} \quad (2.48)$$

The results are illustrated in Figure 2.4(c).

2.3 Electrical Conductivity

The electrical conductivity of an oxide is given by the sum of the partial conductivities of all mobile charged species, i.e. the different ions, electrons and electron holes :

$$\sigma = \sum \sigma_{ion} + \sigma_n + \sigma_p \quad (2.49)$$

In general, for nonstoichiometric oxides, the ionic conduction is usually negligibly small, and Equation 2.49 becomes

$$\sigma = \sigma_n + \sigma_p = e \cdot n \cdot \mu_n + e \cdot p \cdot \mu_p \quad (2.50)$$

Where n and p are the concentrations of the electrons and electron holes (in $\#/cm^3$) respectively, μ_n and μ_p are the mobilities (in $cm^2/V\text{-sec}$) of electrons and electron holes, and e is the electronic charge (in coulombs).

It is clear from Equation 2.50 that studies of the electrical conductivity yield information only about the product of the charge carrier concentration and drift mobility. The objective of this section will be to discuss the nature of the charge carrier concentration and drift mobility individually, and to examine the relationship between the electrical conductivity and the defect structure.

2.3.1 Electron and Electron hole Concentrations

The electronic structure of semiconductors is usually explained by the band theory (9). As illustrated in the Figure 2.5, where the vertical axis represents the

electron energy and the horizontal axis represents the distance through the solid, the valence band and conduction band are separated by an energy gap, $E_g = E_c - E_v$, where E_c is the energy of the lowest level in the conduction band and E_v is the energy of the highest level in the valence band. The conduction in N- or P-type semiconductors is usually categorized according to the origin of the free charge-carrier concentration, intrinsic conduction arising from excitation across the band gap and extrinsic conduction arising from excitation from localized states within the band gap. For a given semiconductor the type observed will depend on the concentration of point defects, impurities and temperature.

Regardless of the detailed conductivity mechanism, the equilibrium constant for the intrinsic ionization and other excitation processes are determined by the electron population or distribution among the energy levels in a crystal. By Fermi statistics it may be shown that the concentration of free electrons is

$$n = [e'] = N_c / (1 + \exp[(E_c - E_f) / kT]) \quad (2.51)$$

Where k is Boltzmann's constant, E_f is the Fermi energy, and N_c is the density of available states in the conduction band. When $E_c - E_f \gg kT$, the Fermi statistics reduces to classical statistics and Equation 2.51 may be written

$$n = N_c \exp[-(E_c - E_f) / kT] \quad (2.52)$$

For the case of a spherical energy surface, assuming that the electrons occupy a narrow band of energies close to E_c , then N_c is given by

$$N_c = (8\pi m_e^* kT / h^2)^{3/2} \quad (2.53)$$

Where m_e^* is the effective mass of the electron and h is Planck's constant.

A corresponding relation holds for the population of electron holes in the valence band.

$$p = [h'] = N_v \exp[-(E_f - E_v) / kT] \quad (2.54)$$

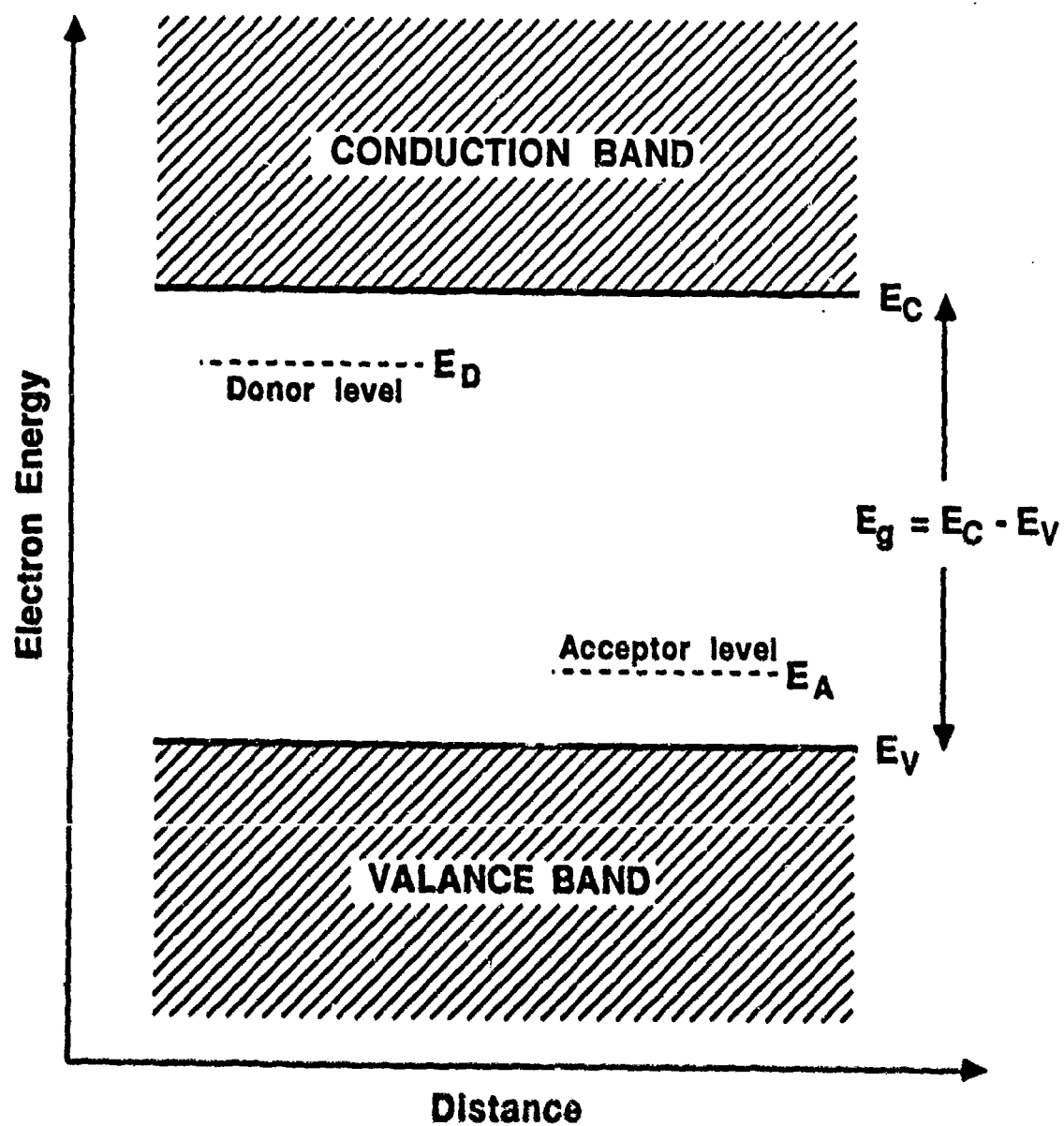


Figure 2.5: Schematic illustration of the energy band diagram for a semiconductor. The donor and the acceptor levels are in the forbidden energy band.

where N_v represents the effective density of states in the valence band. When the effective density of states is located in a narrow region close to E_v , N_v is, corresponding to Equation 2.53, given by

$$N_v = (8\pi m_h^* kT / h^2)^{3/2} \quad (2.55)$$

Where m_h^* is the effective mass of the hole. The equilibrium constant for the intrinsic ionization is then given by

$$K_i = n \cdot p = N_c N_v \cdot \exp(-E_g / kT) \quad (2.56)$$

Where $E_g = E_c - E_v$ is the band gap between the conduction and the valence band. In an intrinsic conductor, $n = p$, and by combining Equations 2.52 to 2.55 we may solve for E_f , the Fermi energy level, which is given by

$$E_f = (E_v + E_c)/2 + 3/4 kT \cdot \ln(m_e^* / m_h^*) \quad (2.57)$$

When the effective masses of the electron and hole are equal, the Fermi level in an intrinsic conductor lies halfway between the valence and conduction band.

In many compounds and particularly in ionic compounds, periodic fluctuations of the electric potential associated with each ion become too large (and energy bands too narrow), so that the band model provides an inadequate description or theory. In this case the electrons or holes may be considered to be localized at the defects or the lattice atoms (valence defects). In such a case electronic conductivity involves a "hopping" of electrons from site to site. And Equations 2.53, 2.55 and 2.57 are no longer valid, however Equations 2.52 and 2.54 are still applicable but N_v and N_c then represent the total number of the atoms at which the electronic species may be localized, multiplied by the degeneracy of the atom states.

2.3.2 Electron and Electron hole Mobility

In an ideal covalent semiconductor, electrons in the conduction band and holes in the valence band may be considered as quasi-free particles. The environment of a periodic lattice and its potential may account for the effective masses of the electron m_e^* and hole m_h^*

In this case the carriers have high drift mobilities in the range of 10 to 10^4 $\text{cm}^2/\text{V}\cdot\text{sec}$. Two types of scattering effect the motion of electrons and electron holes. In a pure semiconductor lattice scattering results from thermal vibrations of the lattice, where the temperature dependence of the drift mobility is given by

$$\mu_L = \mu_{oL} \cdot T^{-3/2} \quad (2.58)$$

Where μ_{oL} is a constant. The mobility decreases with increasing temperature.

In impure semiconductors ionized donor and acceptor centers are positively and negatively charged, respectively, and will serve as scattering centers, which tend to limit the drift mobility. The temperature dependence of the mobility is then given by

$$\mu_I = \mu_{oI} \cdot T^{3/2} \quad (2.59)$$

Where μ_{oI} is a constant. The mobility increases with increasing temperature.

If both mechanisms are present, the mobility is given by

$$\mu = (1/\mu_L + 1/\mu_I)^{-1} \quad (2.60)$$

Apparently, the temperature dependence of the mobility term for the non-polar broad-band semiconductor is much smaller than that for their concentration. As a result, the temperature dependence of the electrical conductivity is mainly determined by the concentration term.

In compounds with predominantly ionic character the mobility of an electron is determined to a large extent by its interaction with the polar modes of the

crystal. In contrast to the classical band theory, the polaron theory (10-13) is utilized. In this case, the electron is considered to interact coulombically with the ions, producing a potential well surrounding the electron which is then self-trapped within it. The electron and its surrounding polarization cloud is commonly described as a quasiparticle and referred as a "polaron". Two different kinds of polarons can be distinguished.

When the association of the electron and the polarization of the lattice is weak, that is, when the lattice distortion extends over several lattice constants a designation of "large polaron" is applied. The large polaron mobility at temperatures above the Debye temperature is given by

$$\mu = \mu_0 \cdot T^{-1/2} \quad (2.61)$$

and is expected to be $\approx 1-100 \text{ cm}^2/\text{V-sec}$ at elevated temperature.

When the electronic carrier plus the lattice distortion has a linear dimension smaller than the lattice parameter, it is referred to as a "small polaron". The mobility is so strongly affected by the lattice distortion that conduction occurs via a thermally activated diffusion process (hopping mechanism). This mechanism is characterized by a very low carrier mobility that increases exponentially with increasing temperature :

$$\mu = (1-c) e a^2 v_0 / kT \cdot \exp(-E_H/kT) \quad (2.62)$$

in which E_H is the hopping energy, $(1-c)$ the fraction of sites unoccupied, a the jump distance and v_0 the attempt frequency. Values of the small polaron mobility are generally found to be on the order of 10^{-4} to $10^{-2} \text{ cm}^2/\text{V-sec}$ at elevated temperatures --- hundreds to thousands of times smaller than in normal band conduction.

2.3.3 Electrical Conductivity and Point Defects

The electrical conductivity and the point defect structure of oxides are closely related. This mainly arises from the fact that most defects are themselves the charge carriers. The relationship between the electrical conductivity and the concentration of defects can be easily demonstrated by examining their oxygen partial pressure dependence. In Figure 2.6, the electrical conductivities are plotted versus oxygen partial pressures according to the various defect structure discussed in section 2.2. In (a) and (c), the $\log \sigma$ vs. $\log P_{O_2}$ plots of two simple types of defect structure, N-type and P-type, show a direct correspondence to the $\log[\text{defect}]$ vs. $\log P_{O_2}$ plots in Figure 2.2(a) and (b). However, in the central region of (b) where both electrons and electron holes contribute to the conductivity, the electrical conductivity does not reflect the defect concentrations in a straight forward manner. These facts indicate that in order to reveal the true defect structure of a material by using the electrical conductivity measurement, one needs to be very cautious. In cases of complicated defect structures, other techniques may be needed along with the conductivity measurement.

It has also been mentioned that the measurement of the electrical conductivity gives only the sum of the concentration-mobility products. In order to achieve a detailed interpretation of the electrical conductivity, it is necessary to determine the mobility and concentration of electrons and electron holes separately. One technique that can be used to determine the mobility is by intentional doping. As discussed in section 2.2.5, impurities may have significant effects on altering the defect concentrations. By choosing the correct type and amount of dopant, one may then fix the charge-carrier concentration and determine the mobility through the conductivity measurement.

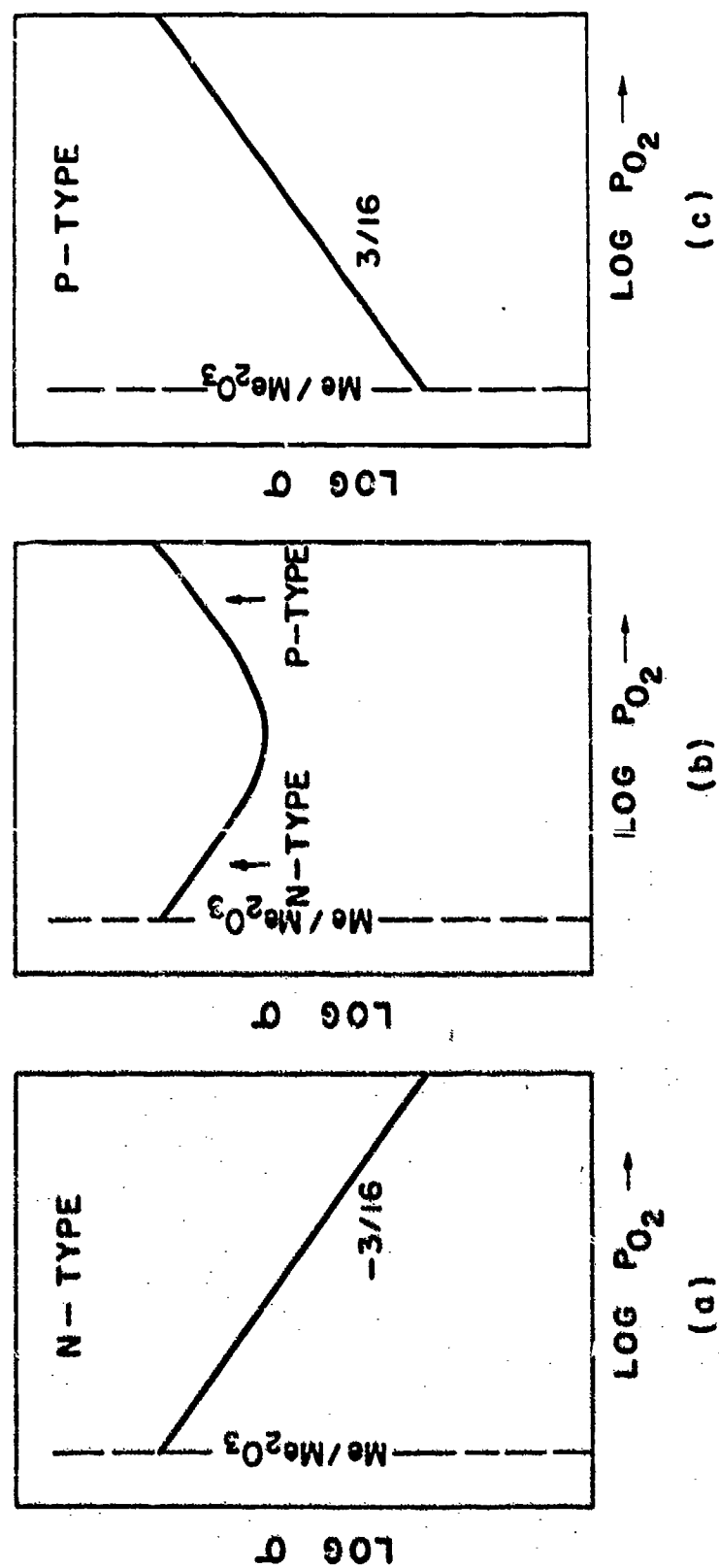


Figure 2.6: Oxygen partial pressure dependence of the electrical conductivity of different defect structure. (a) N-type (b) Mixed-type (c) P-type semiconductors.

2.4 Seebeck Coefficient

Another property which can be utilized to obtain information about the free charge-carrier concentration in a semiconductor is the thermoelectric power, also known as the Seebeck coefficient. The theories of the Seebeck coefficient have been discussed in several articles (2,4-7,13-18). When a N-type semiconductor is subject to a temperature gradient (Figure 2.7(a)), more electrons are excited into the conduction band at high temperature, but the hot electrons tend to diffuse to the cold region. In order to balance the chemical potential gradient due to the temperature difference and the charge concentration gradient, an electrical-field gradient in the opposite direction is created. As a consequence, when the system reaches steady state, the majority carrier (electron) accumulates at the cold end, and a potential difference is set up. Thus when electrons are the majority carrier, the cold end is negative with respect to the hot end. If holes are the majority carriers, the sign of the voltage is opposite.

The Seebeck coefficient Q , V/deg, is defined as

$$Q = dV/dT \quad (2.63)$$

when measured under conditions such that no electrical current flows through the specimen. If Q is taken as

$$Q = -(V_h - V_c) / (T_h - T_c) \quad (2.64)$$

Where $V_h - V_c$ and $T_h - T_c$ are the emf and temperature differences between the hot and cold ends of the specimen, then the sign of the charge carrier corresponds to the sign of Q .

The relationship between the Seebeck coefficient and the concentration of charge carrier can be derived from the transport equations of the electron-current density. It has been shown that for a N-type semiconductor,

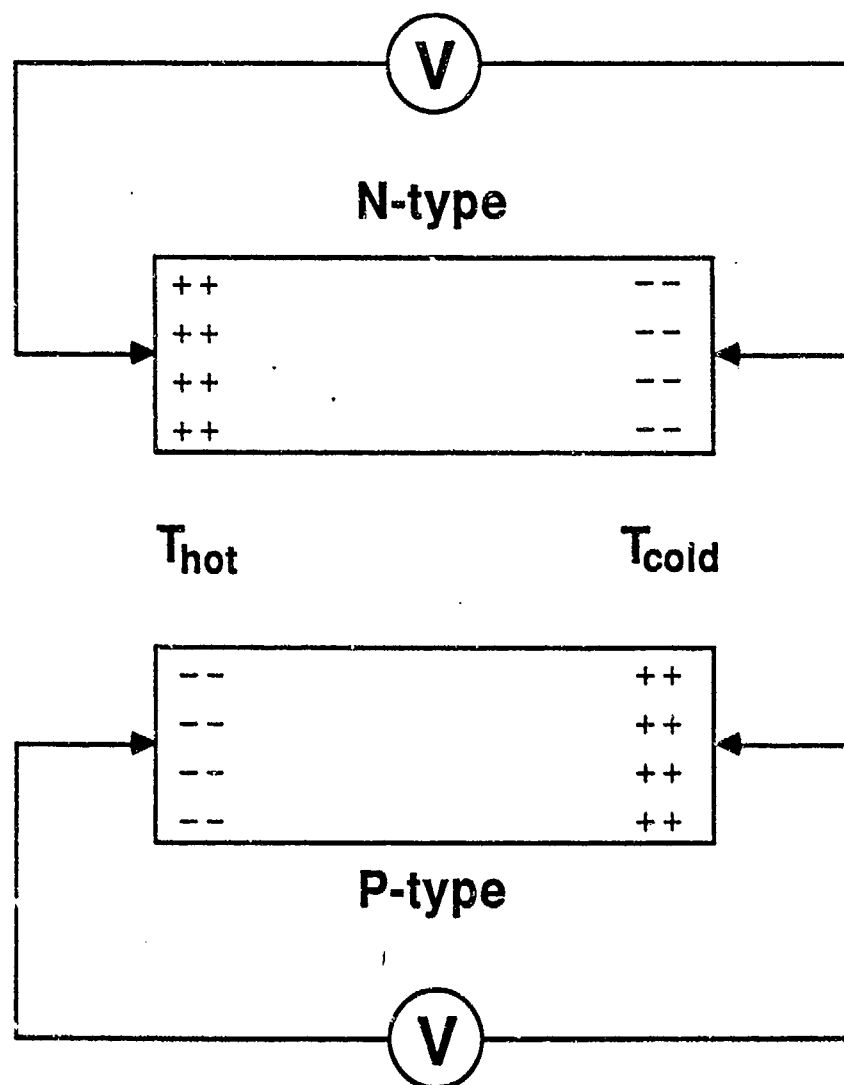


Figure 2.7: Seebeck effect of a semiconductor. The majority carrier diffuses to the cold end, giving a $\Delta V/\Delta T$.

$$Q_n = -(k/e) \cdot (\ln(N_c/n) + A_n) \quad (2.65)$$

and for a P-type semiconductor,

$$Q_p = (k/e) \cdot (\ln(N_v/p) + A_p) \quad (2.66)$$

Where Q_n and Q_p are the Seebeck coefficients of the electrons and holes; N_c and N_v are the density of states of the conduction and valence bands; A_n and A_p are the heats of transport of electrons and holes; and $k/e = 86 \times 10^{-6}$ V/deg.

When electrons and electron holes both contribute to conduction, the Seebeck voltage is

$$Q = (\sigma_n Q_n + \sigma_p Q_p) / (\sigma_n + \sigma_p) \quad (2.67)$$

Thus in order to determine the charge-carrier concentration from the Seebeck coefficient measurement, a knowledge of the effective density of states and the transport-energy term A is required. It has been shown that these parameters can be determined based on the conduction mechanism of the semiconductor. In a broad spherical band conduction, N_c and N_v are related to the effective masses of electron and hole through equations 2.53 and 2.55. Since $A \cdot kT$ represents the kinetic energy of the charge carrier, a value of $A=2$ has been obtained with the assumption that the mean free path is independent of energy. In a narrow band conduction where all the available states are within an energy interval of kT , the density of states is equal to the number of equivalent available sites and is expected to be of the order of 10^{22} cm^{-3} . In this case, the kinetic energy of the charge carrier is much smaller than kT and $A=0$ is obtained. In polaron conduction, similar analysis and results as the narrow band conduction have been obtained.

The Seebeck coefficient measurement has been proved to be an excellent technique in determination of the sign of the charge-carrier present in a semiconductor. However, because of its logarithmic relation to the carrier

concentration this technique is rather insensitive to actually determine the carrier concentration. Especially, it is not easy to examine the oxygen pressure dependence of the carrier concentration through the Seebeck coefficient measurement. In Figure 2.7, the oxygen partial pressure dependence of the Seebeck coefficient is plotted in regard to the different defect structures discussed earlier. An important feature is noticed in Figure 2.7(b). There is a dramatic change in both the value and the sign of the Seebeck coefficient when a transition from P-type to N-type occurs. This fact suggest that the Seebeck coefficient measurement may be superior than the conductivity measurement in dealing with a more complicated defect structure.

2.5 Parabolic Scale Growth

The parabolic scale growth during high temperature oxidation of metals is one of the many properties of crystalline solids that are closely related to their defect structures. In this section the theory of the parabolic scale growth and its relationship to the defect structure of the oxide are discussed. In general, the process of the scale growth can be explained by solid state diffusion theory. Since the diffusion distance increases as the scale grows in thickness, the rate of reaction will decrease with time. When the diffusion process is governed solely by the volume diffusion of the constituent atoms of the scale, the rate of growth of the scale thickness, x , is inversely proportional to the oxide thickness:

$$dx/dt = K_p \cdot (1/x) \quad (2.68)$$

In the integrated form, Equation 2.68 becomes

$$x^2 = 2K_p t + C_0 = K'_p t + C'_0 \quad (2.69)$$

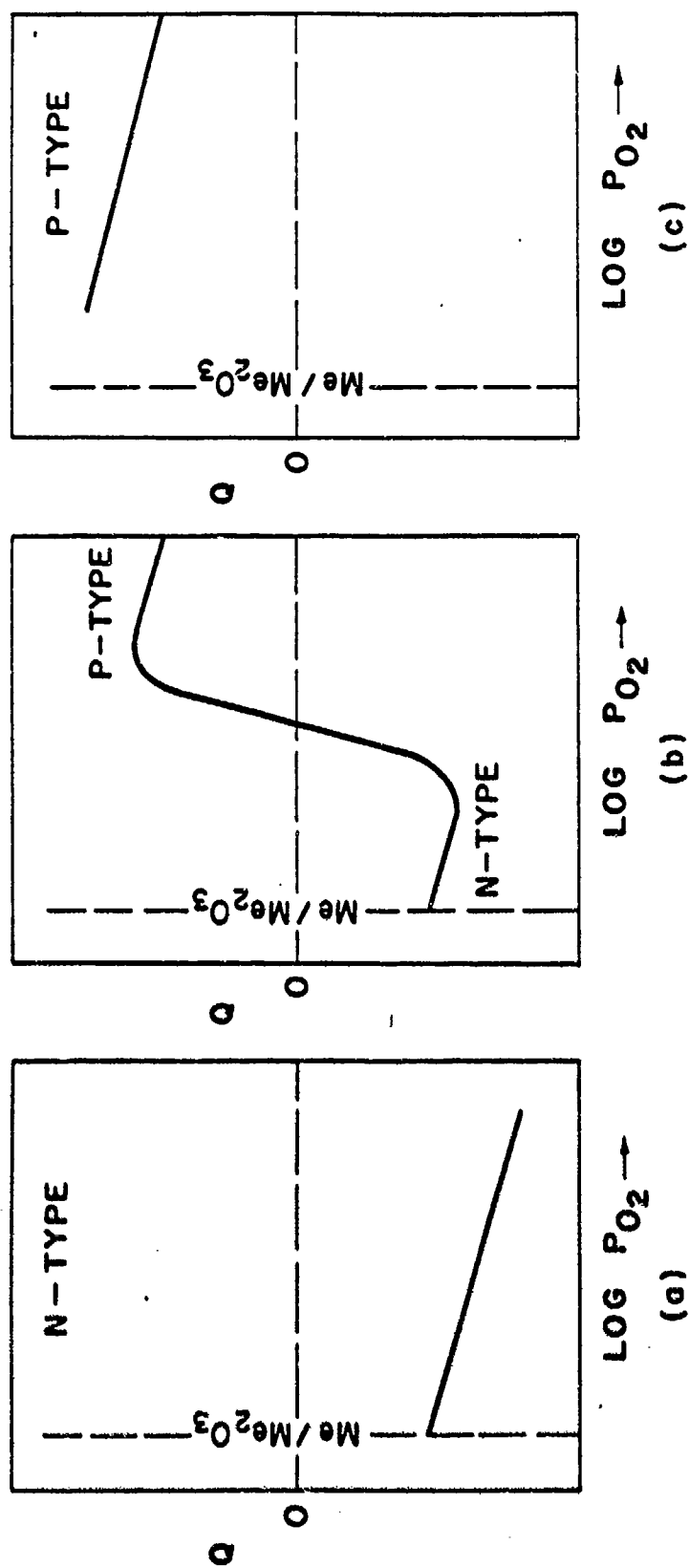


Figure 2.8: Oxygen partial pressure dependence of the Seebeck coefficient of different defect structure. (a) N-type (b) Mixed-type (c) P-type semiconductors.

where C_0 and C'_0 are integration constants. Thus the oxide thickness grows parabolically with reaction time, the oxidation is termed parabolic and K_p (cm^2/sec) is the parabolic rate constant.

The theory of the parabolic oxidation was initially developed by Wagner (20,21), and has recently been extended by several investigators (22-24). Basically, in the case of forming an electronically conducting oxide Me_aO_b , the rate constant can be expressed as

$$K_p = \frac{1}{2} \int_{P_{\text{O}_2}^{(i)}}^{P_{\text{O}_2}^{(o)}} (D_{\text{O}} + (z_c/z_a) \cdot D_{\text{Me}}) d \ln P_{\text{O}_2} \quad (2.70)$$

where $P_{\text{O}_2}^{(o)}$ and $P_{\text{O}_2}^{(i)}$ are the oxygen partial pressures at the oxide/gas and metal/oxide interfaces, respectively; z_c and z_a are the absolute valences of cations and anions; and D_{O} and D_{Me} are the self-diffusion coefficients of oxygen and metal atoms in the oxide. Based on this equation, the parabolic rate constant is then obtained by the integration of the self-diffusion coefficients over the scale. Since the self-diffusion coefficients are directly related to the defect concentrations in the oxide, the rate constant is in turn dependent upon the defect structure of the oxide. When $D_{\text{Me}} \gg D_{\text{O}}$, Equation 2.70 reduces to

$$K_p = \frac{1}{2} (z_c/z_a) \int_{P_{\text{O}_2}^{(i)}}^{P_{\text{O}_2}^{(o)}} D_{\text{Me}} d \ln P_{\text{O}_2} \quad (2.71)$$

It is of interest to examine the oxygen partial pressure dependence of K_p in regarding to the different types of point defect structures discussed in early sections.

In the case of a P-type oxide (Me_2O_3), the self-diffusion coefficient of Me is related to the diffusion coefficient of metal vacancies $D_{V_{\text{Me}}''}$ by

$$D_{\text{Me}} = D_{V_{\text{Me}}''} [V_{\text{Me}}''] \quad (2.72)$$

Since

$$[V_{Me}'''] = [V_{Me}''']^0 \cdot P_{O_2}^{3/16} \quad (2.73)$$

where $[V_{Me}''']^0$ is the vacancy concentration at $P_{O_2} = 1$ atm., one obtains

$$D_{Me} = D_{Me}^0 \cdot P_{O_2}^{3/16}, \quad D_{Me}^0 = D_{V_{Me}'''} [V_{Me}''']^0 \quad (2.74)$$

D_{Me}^0 is then the self-diffusion coefficient of the metal at $P_{O_2} = 1$ atm. Putting Equation 2.74 into Equation 2.71 and performing the integration gives

$$K_p = 4D_{Me}^0 \cdot (P_{O_2}^{(o)})^{3/16} - (P_{O_2}^{(i)})^{3/16} \quad (2.75)$$

When $P_{O_2}^{(o)} \gg P_{O_2}^{(i)}$,

$$K_p = 4D_{Me}^0 \cdot (P_{O_2}^{(o)})^{3/16} \quad (2.76)$$

The parabolic rate constant is then dependent upon the external oxygen partial pressure to the 3/16 power (Figure 2.9(c)).

In the case of N-type oxides, the self-diffusion coefficient D_{Me} is related to the diffusion coefficient of metal interstitials $D_{Mei''}$ by

$$D_{Me} = D_{Mei''} \cdot [Me_i''] \quad (2.77)$$

From

$$[Me_i''] = [Me_i'']^0 \cdot P_{O_2}^{-3/16} \quad (2.78)$$

where $[Me_i'']$ is the metal interstitial concentration at $P_{O_2} = 1$ atm., then

$$D_{Me} = D_{Me}^0 \cdot P_{O_2}^{-3/16}, \quad D_{Me}^0 = D_{Mei''} \cdot [Me_i'']^0 \quad (2.79)$$

D_{Me}^0 is then the self-diffusion coefficient of the metal at $P_{O_2} = 1$ atm.. Putting Equation 2.79 into Equation 2.71, and performing the integration, gives

$$K_p = 4D_{Me}^0 \cdot (P_{O_2}^{(i)})^{-3/16} - (P_{O_2}^{(o)})^{-3/16} \quad (2.80)$$

When $P_{O_2}^{(o)} \gg P_{O_2}^{(i)}$

$$K_p = 4D_{Me}^0 \cdot (P_{O_2}^{(i)})^{-3/16} = 4D_{Me}^i \quad (2.81)$$

where D_{Me}^i is the self-diffusion coefficient of Me in Me_2O_3 in equilibrium with Me, i.e., at $a_{Me} = 1$. Thus the rate constant is independent of the external oxygen partial pressure. (Figure 2.9(a))

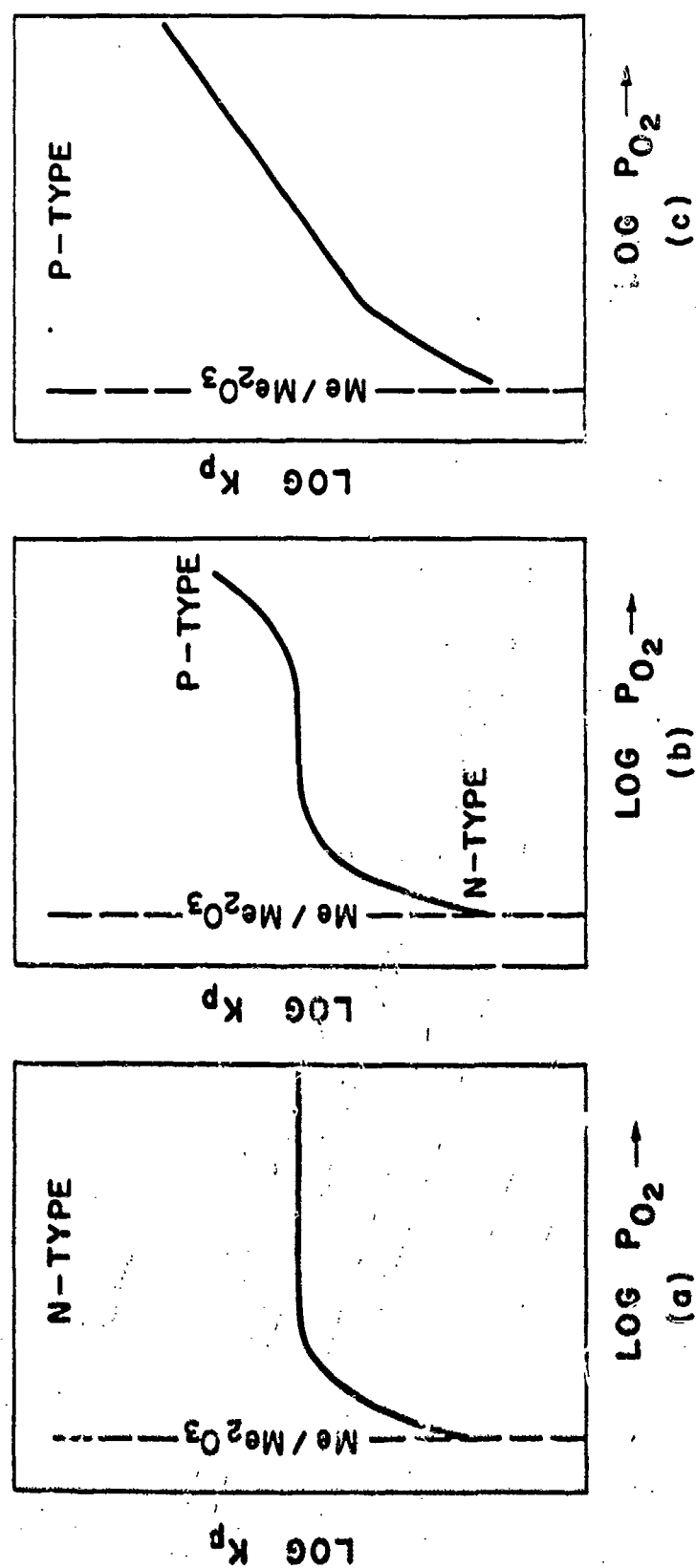


Figure 2.9: Oxygen partial pressure dependence of the parabolic rate constant of different defect structures. (a) N-type (b) Mixed-type (c) P-type semiconductors.

In the case of a complex defect structure, it has been shown (21-22) that the self-diffusion coefficient of the metal in oxide can be expressed by

$$D_{Me} = \sum D_{def} \cdot [defect] \quad (2.82)$$

When the cationic defects are fully ionized,

$$D_{Me} = D_{V_{Me}^{''}} \cdot [V_{Me}^{''}] + D_{Me_i^{''}} \cdot [Me_i^{''}] \quad (2.83)$$

Assuming that $D_{V_{Me}^{''}} = D_{Me_i^{''}}$ then the parabolic rate constant will be

$$K_p = 4D_{Me}^0 \cdot \left\{ \frac{(P_{O_2}^{(o)})^{3/16} - (P_{O_2}^{(i)})^{3/16}}{(P_{O_2}^{(i)})^{3/16} - (P_{O_2}^{(o)})^{3/16}} \right\} \quad (2.84)$$

This equation is illustrated in Figure 2.9(b).

Chapter 3

LITERATURE REVIEW

The purpose of this chapter is to survey the literature which has a bearing on the present study. This chapter is organized into six sections, each section reviews different defect dependent properties of Cr_2O_3 . Section 1 reviews the thermodynamics of the chromium-oxygen system, the crystal structure of Cr_2O_3 and the extent of its nonstoichiometry. Section 2 presents the reported self-diffusion coefficients of chromium and oxygen in Cr_2O_3 . The sintering of Cr_2O_3 is discussed in section 3. In section 4 the high temperature oxidation of chromium is reviewed, while a comparison of different proposed oxidation mechanisms are also discussed. Section 5 reviews the electrical conduction behavior of Cr_2O_3 . The reported electrical conductivities and Seebeck coefficients are also discussed in this section. Finally, a summary based on the available information is given in section 6.

3.1 Some General Aspects of Cr_2O_3

3.1.1 Thermodynamics of the Chromium-Oxygen System

Chromium sesquioxide (Cr_2O_3) is the only solid chromium oxide that is thermodynamically stable at high temperatures. At low temperatures ($<400\text{-}500^\circ\text{C}$) various oxygen-rich phases, e.g., CrO_2 , CrO_3 exist. Although these solid oxides are not important in the high temperature oxidation of chromium, volatile chromium oxide species may be important (25-28). It is generally agreed that CrO_3 is the important species to be considered. In an oxidizing atmosphere it evaporates from Cr_2O_3 based on the reaction



Accordingly, the evaporation rate is proportional to $P_{\text{O}_2}^{3/4}$. Thus at high temperatures CrO_3 evaporation becomes important at high partial pressures of oxygen, i.e., at atmospheric or near-atmospheric oxygen pressure.

3.1.2 The Crystal Structure of Cr_2O_3

Cr_2O_3 possesses the corundum structure, and can be in this respect grouped with oxides such as $\alpha\text{Al}_2\text{O}_3$, Fe_2O_3 , Ti_2O_3 , etc. As shown in Figure 3.1(a) this structure can be considered to consist of hexagonally close-packed oxygen ions where trivalent Cr-atoms occupy two-thirds of the octahedral sites. In Figure 3.1(b), the [210] projection of this structure illustrates the relative positions of the atoms (29).

The extent of nonstoichiometry in Cr_2O_3 was first studied by Cojocaru (30) in 1968 who reported a value of excess oxygen to a fraction of 0.06 per Cr_2O_3 molecule. However questions have been raised with regard to the purity of the sample and the thermodynamic stability of the experiment. Recently Geskovich (31) measured the nonstoichiometry by a tensivolumetric method in the high P_{O_2} range of $\approx 10^1$ to 10^4 Pa at 1100°C , and reported a chromium vacancy concentration of $\approx 9 \times 10^{-5}$ mol/mol Cr_2O_3 in air for Cr_2O_3 with 99.999% purity. Apparently, the extent of the nonstoichiometry in Cr_2O_3 is very small.

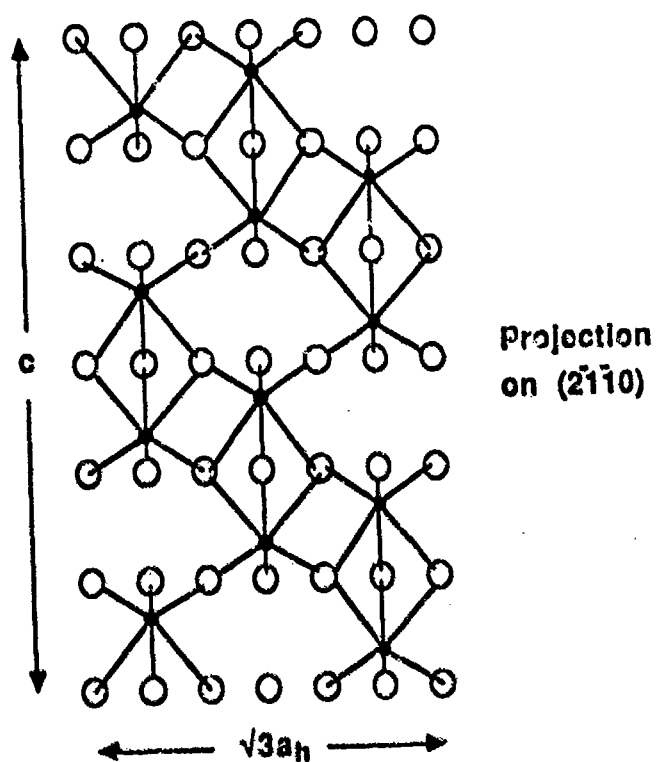
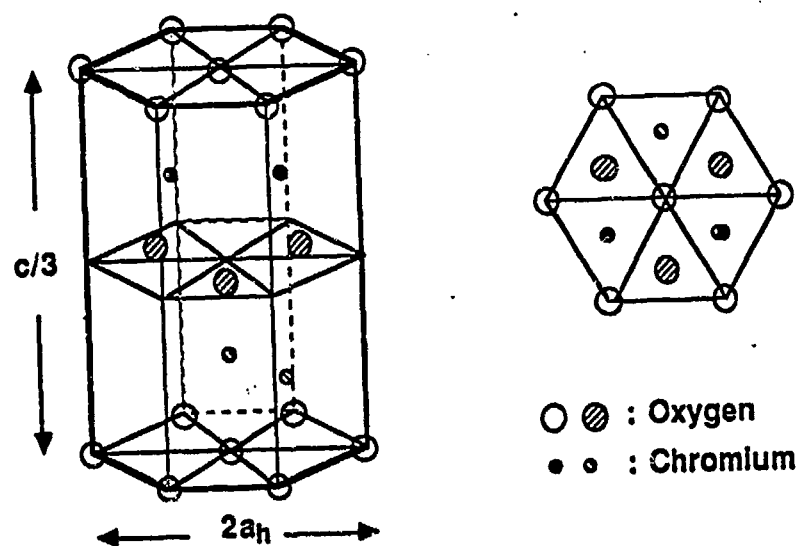
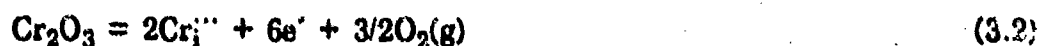


Figure 3.1: The crystal structure of Cr_2O_3 . (a) the hexagonal packing (b) the $[210]$ projection (Ref. 29).

3.2 Self-Diffusion in Cr_2O_3

The early tracer diffusion studies of Cr and O in Cr_2O_3 have been summarized by Kofstad (32). Lindner and Akerstrom (33) and Hagel and Seybolt (34) measured ^{51}Cr diffusion in sintered polycrystalline material at temperatures between 1000° and 1500°C . By using the Nernst-Einstein relation, Hagel and Seybolt (34) were able to calculate the cation transference number $t_{\text{Cr}^{3+}}$ of values in the range of 10^{-3} to 10^{-4} . From these results, it was concluded that Cr_2O_3 behaves almost like a pure electronic conductor.

Walters and Grace (35) measured the diffusion of Cr in single crystal of Cr_2O_3 at 1300°C in $\text{H}_2 + \text{H}_2\text{O}$ gas mixtures within a narrow oxygen partial pressure range of 1×10^{-11} to 5×10^{-11} Pa, and interpreted their results based on a Cr-vacancy defect model. Hagel (36) later measured ^{18}O diffusion in Cr_2O_3 and concluded that oxygen diffusion is about three orders of magnitudes slower than chromium diffusion. Kofstad and Lillernd (37) have analyzed all diffusion data in relation to the oxidation of chromium, and suggested that the self-diffusion occurs by an interstitial mechanism. Considering these results (37) the ionic point defects on the Cr sublattice are Cr interstitials formed by the reaction



Based on this model, Cr_2O_3 may behave as a n-type semiconductor with

$$[\text{Cr}_i^{\bullet\bullet}] = 1/3[e^-] = 3^{-3/4} \cdot K_{\text{Cr}_i^{\bullet\bullet}} \cdot P_{\text{O}_2}^{-3/16} \quad (3.3)$$

and $D_{\text{Cr}}^{\bullet} = f \cdot D_{\text{Cr}_i^{\bullet\bullet}} \cdot [\text{Cr}_i^{\bullet\bullet}]$, where f is the correlation factor, and $D_{\text{Cr}_i^{\bullet\bullet}}$ is the diffusion coefficient of $\text{Cr}_i^{\bullet\bullet}$. One would then expect that the diffusivity of Cr at a given temperature will be proportional to $P_{\text{O}_2}^{-3/16}$.

Recently Hoshino and Peterson (38) have measured the self-diffusion of ^{51}Cr in single crystals of Cr_2O_3 as a function of oxygen partial pressure at 1490° and

1570°C. They found that the values of the self-diffusion coefficients are about 10^4 times smaller than those early reported. Also, at 1570°C their data show a relationship of $D \propto P_{O_2}^{3/16}$ over the P_{O_2} range from 10^{-5} to 10^{-9} atm. A vacancy mechanism expressed by the reaction



is utilized in their interpretation.

In Atkinson and Taylor's study (39), similar measurements were performed. Their data at temperatures of 1100 and 1300°C also show much smaller values compared with those of earlier studies. However they found that the dependence of D_{Cr}^* on P_{O_2} is consistent with diffusion by vacancies at high P_{O_2} and by interstitials at low P_{O_2} . At 1100°C, a transition from F-type behavior at high P_{O_2} to N-type at low P_{O_2} was observed at an oxygen partial pressure of 10^{-10} atm..

By combining the data from the chemical diffusion coefficients and the measurement of the nonstoichiometry, Greskovich (31) was able to estimate the self-diffusion of Cr in Cr_2O_3 . A value of $D_{Cr} = 0.8 \times 10^{-17}$ cm²/sec at 1100°C and 10^{-6} atm. P_{O_2} was reported which is similar to Atkinson and Taylor's measurements. Their data on the deviation from the nonstoichiometry also show a vacancy mechanism in the high P_{O_2} region at 1100°C.

In Figure 3.2, a compilation of the reported diffusion coefficients of Cr and O in Cr_2O_3 are plotted in Arrhenius form. It is quite clear that the values of recent measurements are much lower than those of early studies. Two major reasons can be accounted for this discrepancy. First, the impurity contents in early studies were much higher which may have greatly affected the defect concentrations. Second, short circuit diffusion, such as, grain boundaries and dislocations, could contribute to a great extent to the total diffusion process.

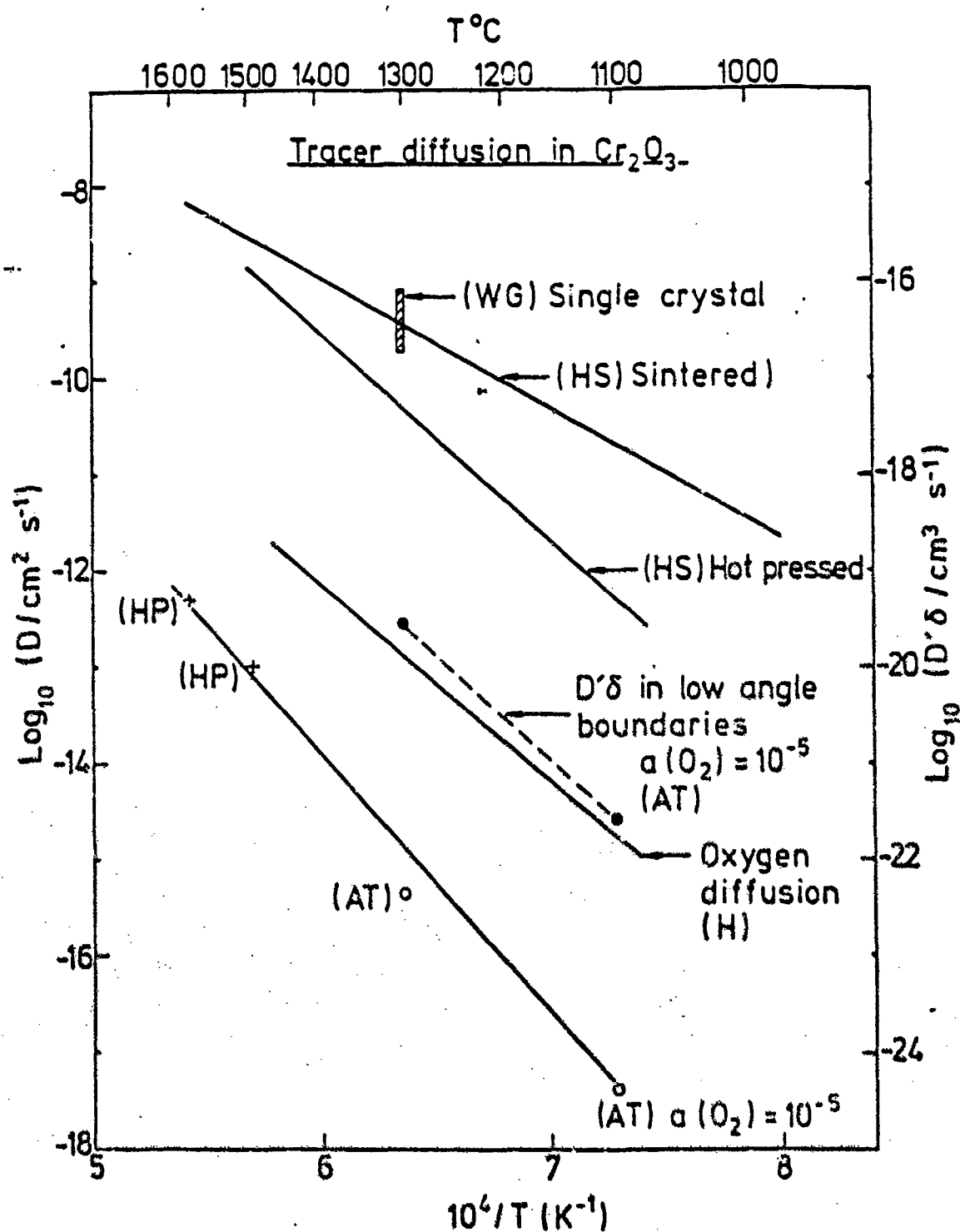


Figure 3.2: Comparison of diffusion coefficients in Cr_2O_3 . The data are labelled by authors' initials (Ref. 39).

3.3 Sintering of Cr₂O₃

Sintering of Cr₂O₃ at atmospheric or near-atmospheric pressure of oxygen yields fine grained, highly porous structures with poor densification (40-45). However, when the partial pressure of oxygen is reduced, sintering rates are markedly increased (Figure 3.3). Ownby and Jungquist (40) studied the final sintering of Cr₂O₃ at 1600°C. After a sintering time of 1 hr, the theoretical density only reached 63% at 10⁵ Pa. O₂ while essentially 100% density was reached at partial pressures of oxygen close to the decomposition pressure of Cr₂O₃. A particularly rapid increase in densification took place when oxygen pressures close to the decomposition pressure were approached.

Halloran and Anderson (42) and Neve and Coble studied the initial sintering mechanism of Cr₂O₃ by a volume diffusion model, and concluded that the rate of sintering is determined by the migration of the oxygen atoms. In recent studies of Su et al. (45), it was found that both volume diffusion and grain boundary diffusion are important. All these results indicated that oxygen vacancies formed by



are involved. Since diffusion-controlled sintering is governed by the transport of the slower diffusion species (46), i.e., the oxygen atoms, it is tentatively agreed that oxygen vacancies constitute the oxygen point defects, and that these are the minority defects in Cr₂O₃, at least at partial pressures of oxygen near the decomposition pressure of Cr₂O₃.

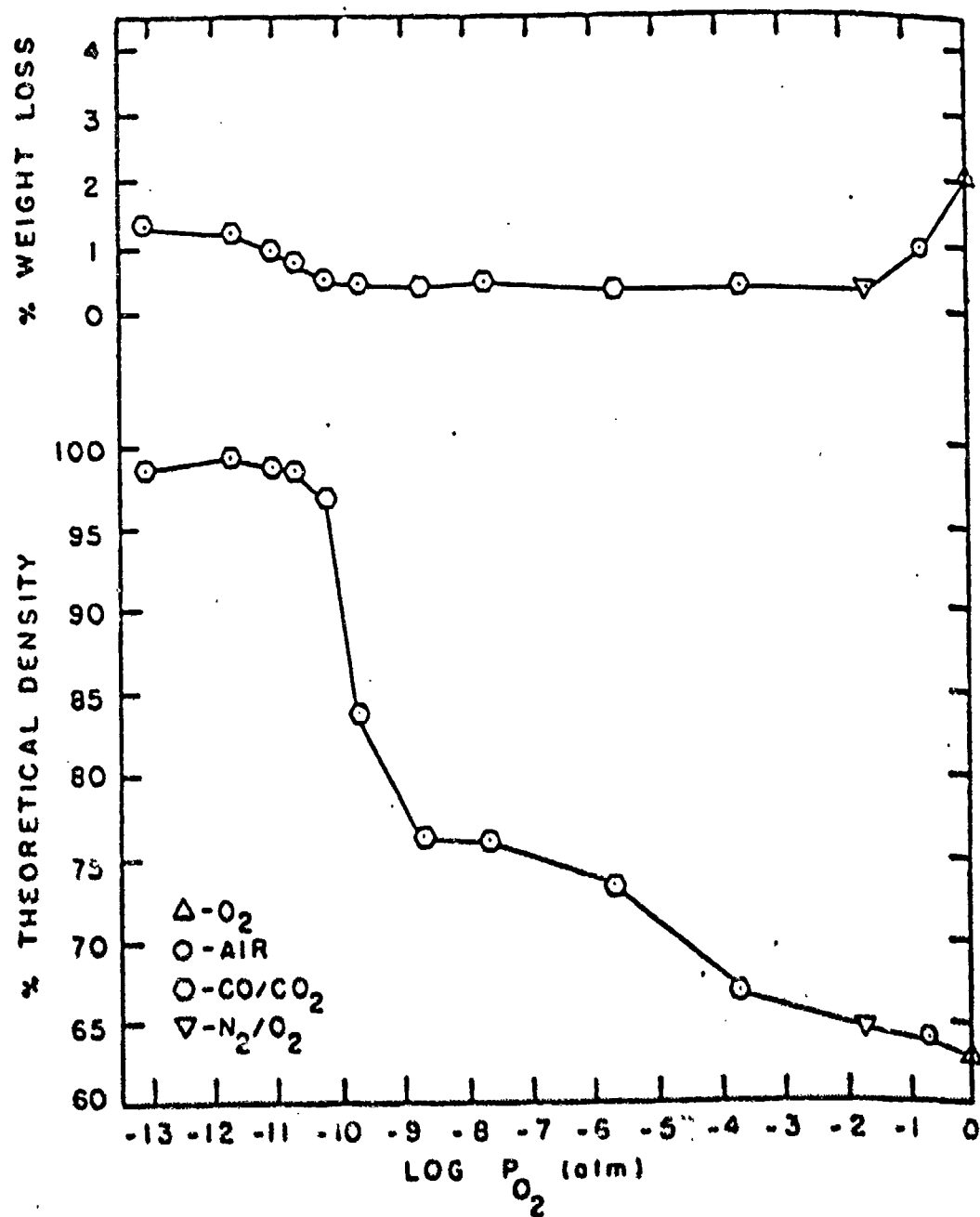


Figure 3.3: Final density of Cr_2O_3 as a function of sintering atmosphere

3.4 High Temperature Oxidation of Chromium

The high temperature oxidation of chromium has been investigated very extensively (47-59) at temperatures up to 1400°C. The kinetics of the growth of Cr_2O_3 scale above 700°C are generally interpreted as parabolic. Reported values of corresponding parabolic rate constants have recently been summarized by Hindom and Whittle (52). As shown in Figure 3.4, it is very striking to find that the K_p values vary by more than four orders of magnitudes in the temperature range 1000 - 1200°C. Several factors may have contributed to the inconsistency of the various determinations.

The defects arising from sample preparation and exposure techniques during oxidation experiment have been discussed by Caplan et al. (53), and Lillernd and Kofstad (47). Although remarkable differences in oxidation behavior were attributed to a strong dependence on scale morphology (grain size, orientation, etc.) and on the surface preparation techniques (mechanical abrasion, eletropolishing, etching, etc.), no direct correlation was established. As a general feature, a fine-grained scale grew considerably faster than that composed of a few, large, well-oriented crystallites. Caplan and Sproule (54) in turn deduced that the monocrystalline oxide grows by cation lattice diffusion. Nonuniform growth in the form of nodules, blisters and multilayered ballons take place by a two-way transport : metal ion (lattice) diffusion outward and oxygen ion diffusion inward along grain boundaries.

The formation of volatile oxide species during the course of reaction is also an important factor. Whereas the oxidative vaporization of Cr_2O_3 at reduced P_{O_2} is negligible, it becomes significant at high oxygen pressures for temperatures >

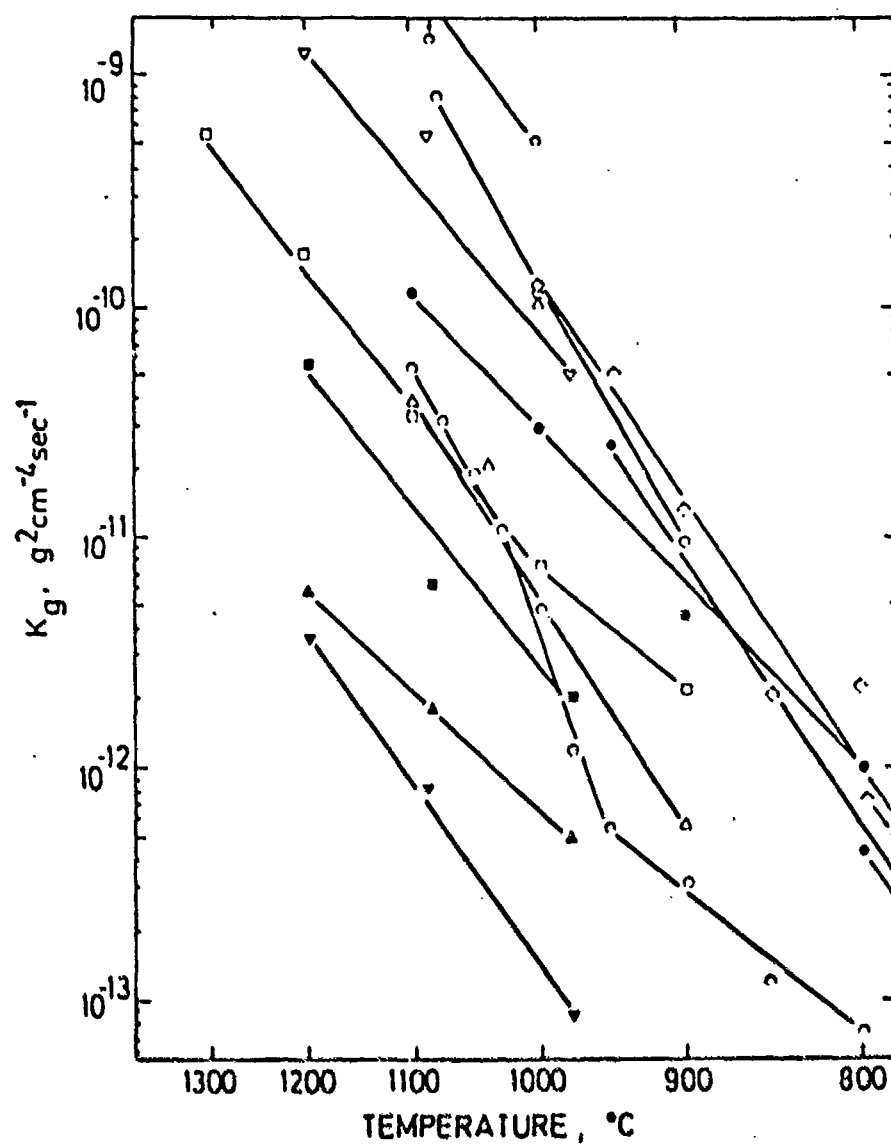


Figure 3.4: Arrhenius plot of reported parabolic rate constants for the oxidation of pure Cr

1000°C. Since in thermogravimetric studies of chromium oxidation one measures the net weight difference between oxygen uptake and oxide evaporation, corrections of the kinetic data for the evaporation losses are necessary. The discrepancy in different studies can be attributed to the ignorance of or the inaccuracy of this correction.

It has been suggested that differences in the impurity levels of the chromium metal used in different studies may also be responsible. Small alloy additions to chromium may significantly affect the oxidation mechanism by modifying the point defect concentrations in Cr_2O_3 . Hagel (55) found that Li-doped chromium and Cr-0.5wt.% Fe had smaller rate constants compared to unalloyed chromium. Trivalent alloying additions (0.9 and 4.7% Al) to chromium did not significantly affect the oxidation rate. McPherson and Fontana (56) found that Ti alloying additions increase the oxidation rate. However, in order to interpret the impurity effect, a complete knowledge of the point defect structure of Cr_2O_3 is necessary.

According to the Wagner's theory, the parabolic growth rate constant for scales with predominant cation transport (Cr) can be related to the cation (Cr) diffusion coefficient by

$$K_p \propto \int_{P_{\text{O}_2}^{(i)}}^{P_{\text{O}_2}^{(o)}} D_{\text{Cr}} d(\ln P_{\text{O}_2}) \quad (3.6)$$

where $P_{\text{O}_2}^{(o)}$ and $P_{\text{O}_2}^{(i)}$ are the oxygen partial pressure in the ambient gas and at the scale-metal interface, respectively. Depending upon the type of the defect structure of Cr_2O_3 , D_{Cr} may have different oxygen pressure dependence. Accordingly, the rate constant K_p may vary with oxygen partial pressure in a different manner.

Hagel (55) measured the oxidation of chromium at 750° and 1100°C at oxygen pressures ranging from 10^2 to 1 Pa O_2 . He observed either a slight or

increase in the K_p with increasing P_{O_2} , and estimated the lowest limit of n in the relationship $K_p \propto P_{O_2}^{1/n}$ to be about 40.

Kassner, Walters and Grace (58) studied the reaction rate at 700° to 990°C in H_2/H_2O mixtures with partial pressures close to those of the decomposition pressure of Cr_2O_3 . The parabolic rate constant increased with increasing partial pressure of oxygen, and they interpreted the oxygen pressure dependence as

$$K_p \propto P_{O_2}^{3/16} \quad (3.7)$$

This relationship is expected if Cr vacancies (Equation 3.4) predominate in the scale. On the other hand, in a recent study by Hindom and Whittle (59), the growth rate of Cr_2O_3 on pure Cr, Ni-25 and 50%Cr and Co-25% Cr were measured at 1000°C in flowing CO/ CO_2 mixtures of P_{O_2} in the range 8.4×10^{-15} to 8.3×10^{-9} atm.. The parabolic growth constant was found to be virtually independent of oxygen potential for both Cr and the alloys. They interpreted their results in terms of the Cr interstitial model (Equation 3.2), and concluded

$$K_p \propto D_{Cr}^0 \cdot (P_{O_2}^{(i)})^{-3/16} = D_{Cr}^i \quad (3.8)$$

where D_{Cr}^0 is the self-diffusion coefficient of Cr in Cr_2O_3 in equilibrium with oxygen at unit activity, $P_{O_2}^{(i)}$ is the oxygen pressure at the scale-metal interface, and D_{Cr}^i is the self-diffusion coefficient of Cr in Cr_2O_3 in equilibrium with Cr (i.e., at $a_{Cr} = 1$).

3.5 Electrical Conductivity and Seebeck Coefficient

The electrical conductivity of Cr_2O_3 has been studied by a number of investigators (60,73). Crawford and Vest (61) made their measurement on single crystals while the other investigators used sintered and hot-pressed specimens. In Figure 3.5, the electrical conductivities measured in air and at 1 atmosphere of

P_{O_2} and are plotted in Arrhenius form. The behavior may be divided into two main regions, (1) a high temperature region above 1000° to 1200°C with an activation energy of 1.6 to 1.8 eV (155 to 175 KJ/mole), and (2) a low temperature region with an appreciably smaller activation energy. The results for the low temperature region show much larger discrepancies than that of the high temperature region.

Hicks et al. (65) and Memdoweroft and Hicks (66) have measured the electrical conductivity as a function of both oxygen partial pressure and temperature. Their results are shown in Figure 3.6. At high temperatures the electrical conductivity is independent of the oxygen partial pressure. At low temperatures the electrical conductivity decreases as the oxygen partial pressure is decreased.

It is generally concluded that the high temperature regions reflect the intrinsic electronic equilibrium in the oxide, and the conduction process can be expressed as

$$\text{Null} = e' + h' \quad (3.9)$$

and $n = p = n_i$ where n_i = intrinsic electron concentration one obtain

$$K_i = n_i^2 \quad (3.10)$$

According to the broad band theory, the temperature dependence of the electrical conductivity will come mainly from the concentration of electrons and electron holes. Thus the activation energy of the electrical conductivity will be expected to be one-half of the value of the band-gap. As a rough estimation, an energy gap of $E_g = 3.4$ eV is obtained. Accordingly one may estimate the intrinsic electron concentration from the equation

$$K_i = n_i^2 = N_c \cdot N_v \cdot \exp(-E_g/kT) \quad (3.11)$$

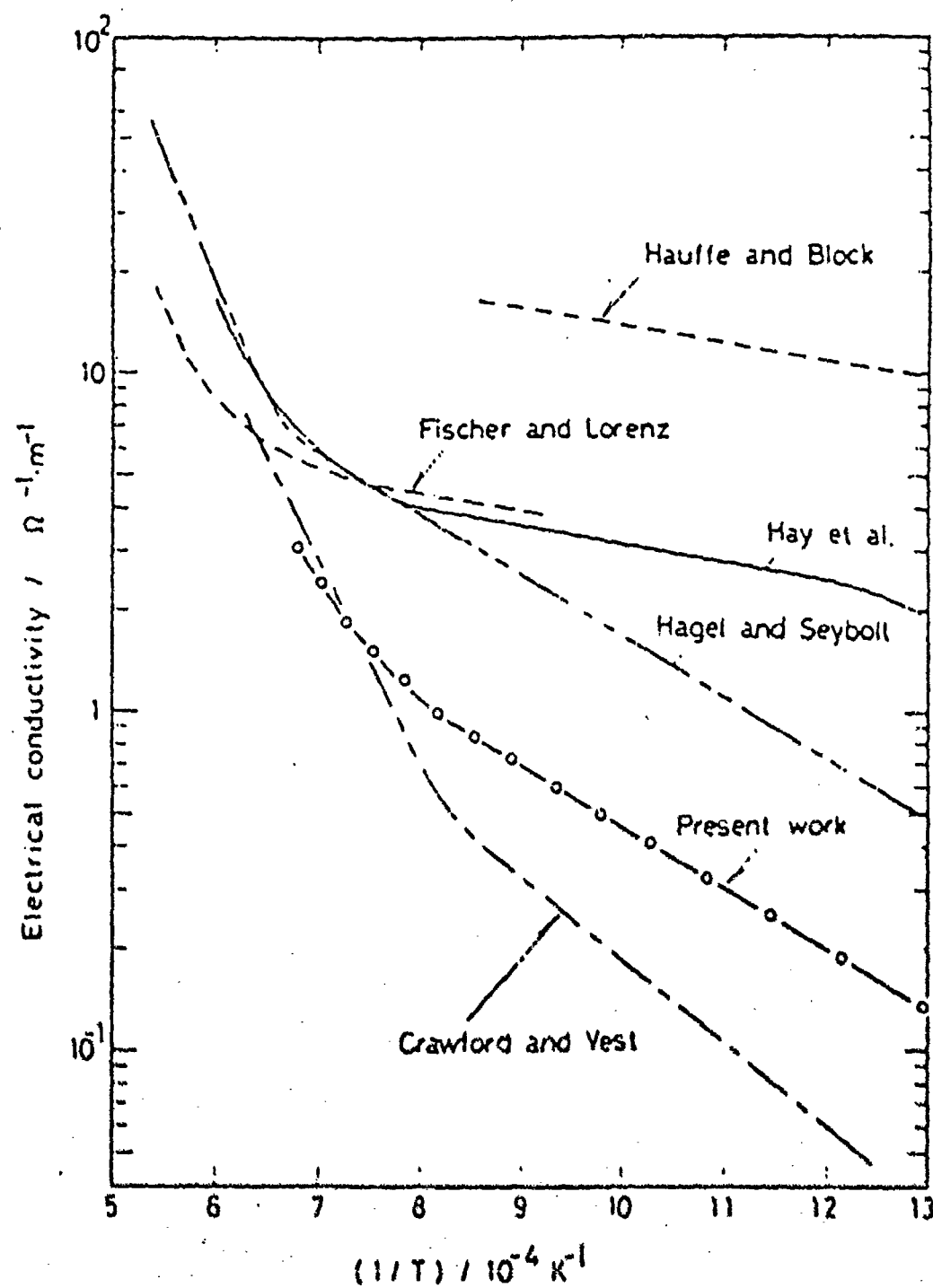


Figure 3.5: Electrical conductivity of Cr_2O_3 . Results by Hauffe and Block (62), Fischer and Lorenz (63), Hay et al. (67), Hagel and Seybolt (34), and Crawford and Vest (61) are also included.

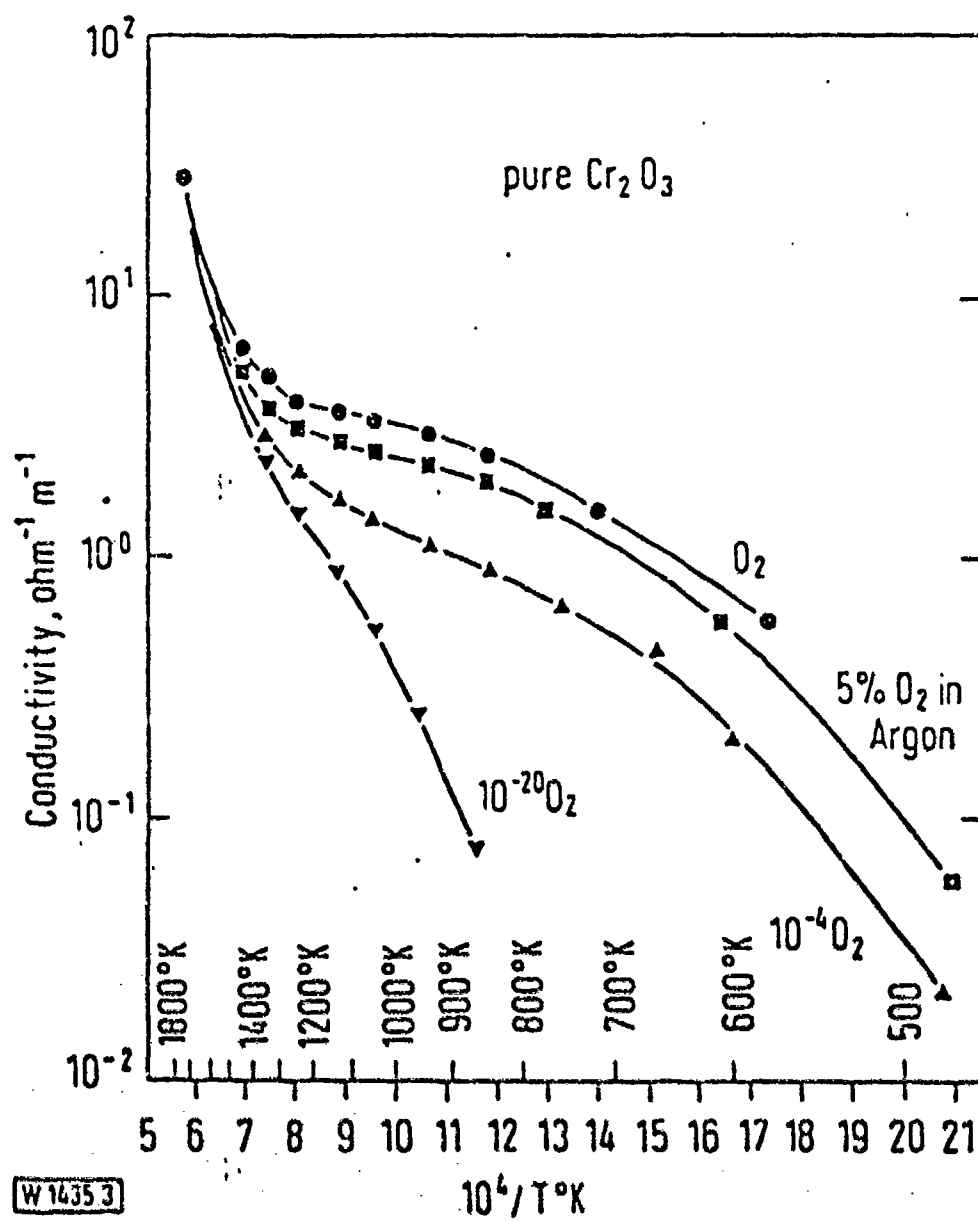


Figure 3.6: Variation of electrical conductivity of Cr_2O_3 with $1/T$ for a range of oxygen pressures

where N_C and N_V are the effective densities of states in the conduction and valence bands, and k is Boltzman constant. If one assumes $N_C = N_V$ and is equal to twice of the total number of cation sites ($\approx 4 \times 10^{22} \text{cm}^{-3}$), (the two comes from the degeneracy of the electronic spin state) then at $T = 1500^\circ\text{C}$,

$$n_i = (2 \times 4 \times 10^{22})^2 \cdot \exp(-3.4/86 \times 10^{-6} \times 1673) = 1.37 \times 10^{36} \quad (3.12)$$

and the maximum intrinsic electron concentration will then be equal to 10^{18}cm^{-3} . However, a much larger value of the electron hole concentration $p = 2 \times 10^{20} \text{cm}^{-3}$ has been reported by Hay et al. (65) from thermoelectric power measurements. Apparently, more investigation is required in order to clarify this conflict.

The thermoelectric power (Q) of Cr_2O_3 measured by Hay et al. (65) is shown in Figure 3.7. While the results show positive values at all temperatures and P_{O_2} 's, the Q values decrease more rapidly in the high temperature region than in the low temperature region. At high temperatures unusual behavior is observed when the P_{O_2} dependence is considered. As P_{O_2} is decreased Q decreases but only to a certain point. At low temperatures as P_{O_2} is decreased, Q first increases and then decreases. Although it is difficult to interpret the low temperature behavior, the positive values of the thermoelectric power indicate that Cr_2O_3 may behave as a P-type semiconductor. The conduction mechanism may be expressed by consideration of Equation 3.4, i.e.,



$$K_{V_{\text{Cr}}^{\bullet\bullet}} = [V_{\text{Cr}}^{\bullet\bullet}]^2 \cdot [h^{\bullet}]^6 \cdot P_{\text{O}_2}^{-3/2} \quad (3.14)$$

In the high temperature region where intrinsic behavior is expected, the positive Q 's indicate that electron holes may have a higher mobility than electrons.

When the low temperature region is considered, several reasons have been suggested for the transition of the electronic behavior. Hagel and Seybolt (34)

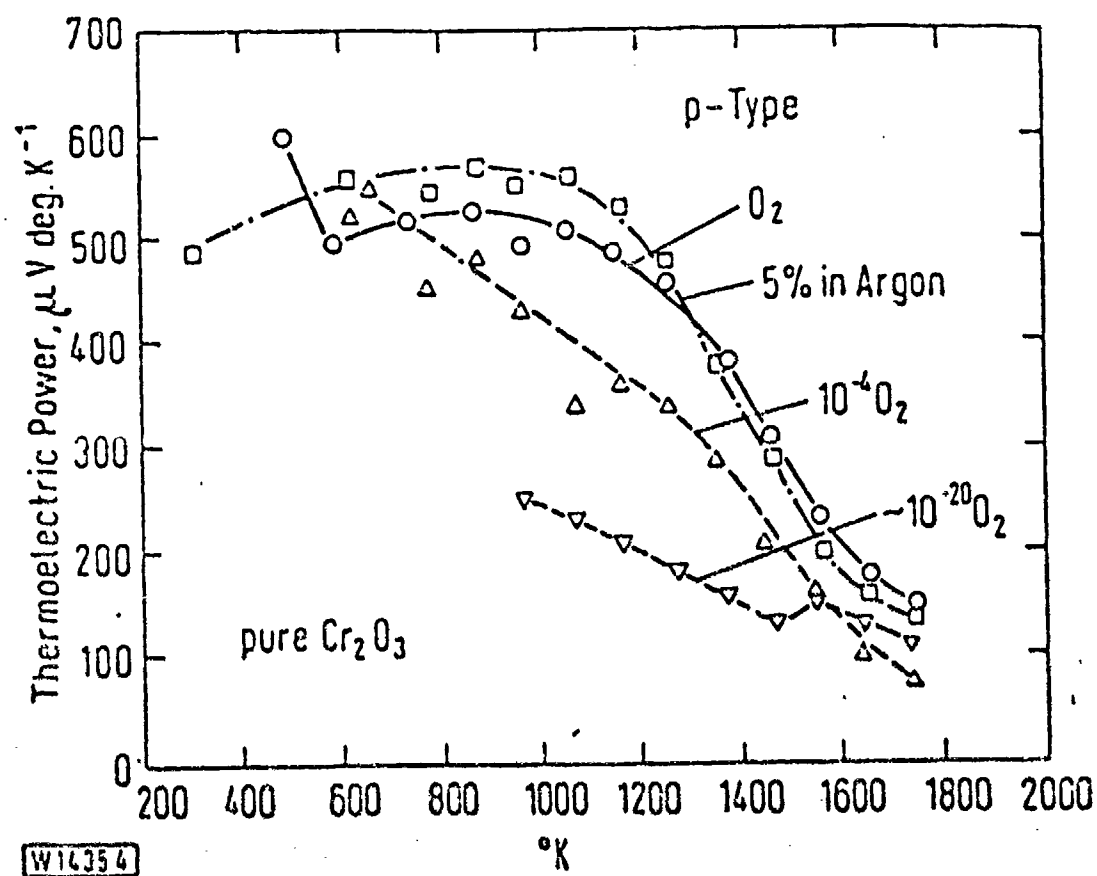


Figure 3.7: Variation of thermoelectric power of Cr_2O_3 with temperature for a range of oxygen pressures

suggested that the defect structure may be "frozen in" and that the associated activation energy represents that of the hole motion.

Recently, Young et al. (68) measured the Seebeck coefficients on sintered compacts of Cr_2O_3 . When the compacts were sintered under a very low oxygen partial pressure (2×10^{-12} atm) at high temperature (1920°K) and quenched to room temperature, a n-type behavior was observed. These results suggest that Cr interstitials may be the predominant point defects in Cr_2O_3 at low oxygen partial pressures.

It has also been pointed out by other investigators (61,65) that at low temperatures complete ionic equilibrium was difficult to achieve. As stated by Hay et al. (65), considerable equilibrium time was necessary even at high temperatures (> 16 hours for 4 mm thick specimens at 1570°K). This interpretation appears to be consistent with the low diffusion coefficient of Cr in Cr_2O_3 .

Fischer and Lorenz (69,70), on the other hand, concluded that the observed behavior is extrinsic and controlled by impurities in the low temperature region, i.e., that low-valent cation impurities predominate and that

$$[\text{Mf}_{\text{Cr}}] = p \quad (3.15)$$

This interpretation explains very nicely the large discrepancies in the electrical conductivity at low temperatures reported by different studies.

There may be another reason which has not been discussed in the literature. Since the activation energies of K_i and $K_{V_{\text{Cr}}}$ are apparently different, as temperature is decreased a change of the defect structure from intrinsic to p-type behavior may also lead to a change of the activation energy.

The effects of dopants on the electrical conduction behavior of Cr_2O_3 have also been studied. Doping with acceptors such as Mg (69), Ni, Cu (70), or Li

(71,72) was found to increase the electron hole conductivity, and the material becomes p-type under all conditions. When the acceptor is homogeneously dissolved, the electron hole concentration is determined by $[h'] = [Mf_{Cr}']$, and the electrical conductivity is independent of P_{O_2} . When a second phase is present, e.g., for Cu^+ as the dopant with an excess of Cu_2O .



$$K_{Cu_2O} = [Cu_{Cr}'']^2 \cdot [h']^4 \cdot P_{O_2}^{-1} \quad (3.17)$$

$$[h'] = 2[Cu_{Cr}'] = K_{Cu_2O}^{1/6} \cdot P_{O_2}^{1/6} \quad (3.18)$$

the electrical conductivity increases with P_{O_2} . Doping with donors such as W (62), Ti (69), Nb, or V (70), on the other hand, displays different effects on the P_{O_2} behavior, the material behaves as n-type after annealing in argon (α low P_{O_2}), but changes to p-type after annealing in air. Based on their studies of the thermoelectric power, Fischer and Lorentz (63) concluded that this behavior is due to the variation of the solubility of the dopant. The n-type conductivity is independent of P_{O_2} below a certain P_{O_2} where $[donor] < solubility\ limit$ but decreases with increasing P_{O_2} when the solubility and therefore the electron concentration decreases causing ultimately the change to p-type. The solubility decrease can be explained by the reaction, i.e., for Ti^{4+} as the dopant.



$$K_{TiO_2} = [Ti_{Cr}]^2 \cdot [e']^2 \cdot P_{O_2}^{-1/2} \quad (3.20)$$

$$[e'] = [Ti_{Cr}] = K_{TiO_2}^{1/4} \cdot P_{O_2}^{-1/8} \quad (3.21)$$

However, recently Kroger (60) has pointed out that similar effects may also occur as a result of a change in stoichiometry even when the solid solution remains unsaturated. It appears that more thorough investigations are needed.

3.6 Summary

Although large discrepancies have been shown in the literature with regard to the point defect structure of Cr_2O_3 , a few major conclusions may still be drawn :

- (1) The point defect structure of Cr_2O_3 appears to be very complicated, and can not be represented by a simple defect model.
- (2) Chromium point defects are the major ionic point defects in Cr_2O_3 while oxygen point defects are the minority.
- (3) There are indications that the predominant defects in the high P_{O_2} region and the low P_{O_2} region are not the same. At high P_{O_2} 's chromium vacancies are probably predominant. At low P_{O_2} 's, near the decomposition pressure of Cr_2O_3 , Cr interstitials may become predominant.
- (4) Cr_2O_3 is an intrinsic electronic conductor at high temperatures ($T > 1200^\circ\text{C}$) and at high P_{O_2} 's. The p-type behavior measured by Seebeck coefficients suggests a higher mobility for electron holes than for electrons.
- (5) At low temperatures, the large discrepancies of the electrical conductivity may be caused by the presence of unavoidable impurities, the "frozen in" defects, or simply a change of defect structure.
- (6) Both impurity effects and grain boundary diffusion may play important roles in the high temperature oxidation of chromium.

Chapter 4

EXPERIMENTAL PROCEDURE

This chapter describes the general experimental procedure of this research work. Sample preparation and characterization are first discussed. Descriptions of the experimental apparatus and procedures of the electrical conductivity and Seebeck coefficient measurements are then presented.

4.1 Sample Preparation

TiO₂-doped Cr₂O₃, MgO-doped Cr₂O₃ and high purity Cr₂O₃ pellets were prepared by conventional powder methods. TiO₂ and MgO powder were purchased from Alfa Products while high purity Cr₂O₃ powder was supplied by Johnson Matthey Inc.. Table 1 lists the purity of these raw materials.

Table 1: The listed purity of the raw material used in this study

Cr ₂ O ₃	Purity 99.999%	Major Impurity Ag, Al, Ca, Cu, Fe, Mg and Si < 1 ppm
TiO ₂	99.98 %	=====
MgO	99.999%	=====

In preparation of the TiO₂ and MgO doped Cr₂O₃ pellets, the Cr₂O₃ powder was first mixed with the dopant powder in a certain ratio (0.1 to 0.5 mole %). The mixed powder was then put into a plastic bottle, and mixed on a mechanical shaker for 5 minutes. For the pure Cr₂O₃ pellets this step was not necessary. After mixing the powder was ground in a diamonite mortar and pestle for two

hours in order to achieve better homogeneity. The ground powder was then uniaxially pressed at $3.45 \times 10^8 \text{ N/m}^2$ (50,000 psi) into pellets of 5.1 mm. in diameter and 5.7 mm. in height without using any binder. The green density of these compacts was about 55% of the theoretical density.

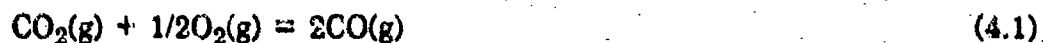
4.1.1 Sintering

Sintering of the compacts was carried out at 1600°C in a horizontal Al_2O_3 tube furnace which was molybdenum-wire wound and hydrogen protected. The final density of the sintered samples is strongly dependent upon the oxygen atmosphere (Fig. 4.1). Dense samples were obtained from low P_{O_2} sintering while porous samples were obtained at high P_{O_2} 's. After sintering, all the specimens were subsequently homogenized in air at 1300°C for three days.

4.1.2 Atmosphere Control

The oxygen potential was controlled by using O_2/Ar and CO/CO_2 gas mixtures. O_2/Ar were used for high P_{O_2} 's, and CO/CO_2 were utilized for low P_{O_2} 's. The principle and procedure of using the CO/CO_2 gas mixture for controlling the P_{O_2} have been discussed extensively in the literature (74,75).

Basically, this is achieved by considering the reaction:



From the equilibrium constant

$$K_1 = \text{P}_{\text{CO}}^2 / (\text{P}_{\text{CO}_2} \text{P}_{\text{O}_2}^{1/2}) \quad (4.2)$$

one obtains a relationship between the oxygen partial pressure (P_{O_2}) and the ratio of P_{CO_2} and P_{CO} . In Figure 4.2, this relationship is illustrated by plotting the oxygen pressure as a function of temperature and $\text{P}_{\text{CO}_2}/\text{P}_{\text{CO}}$ ratios at a total

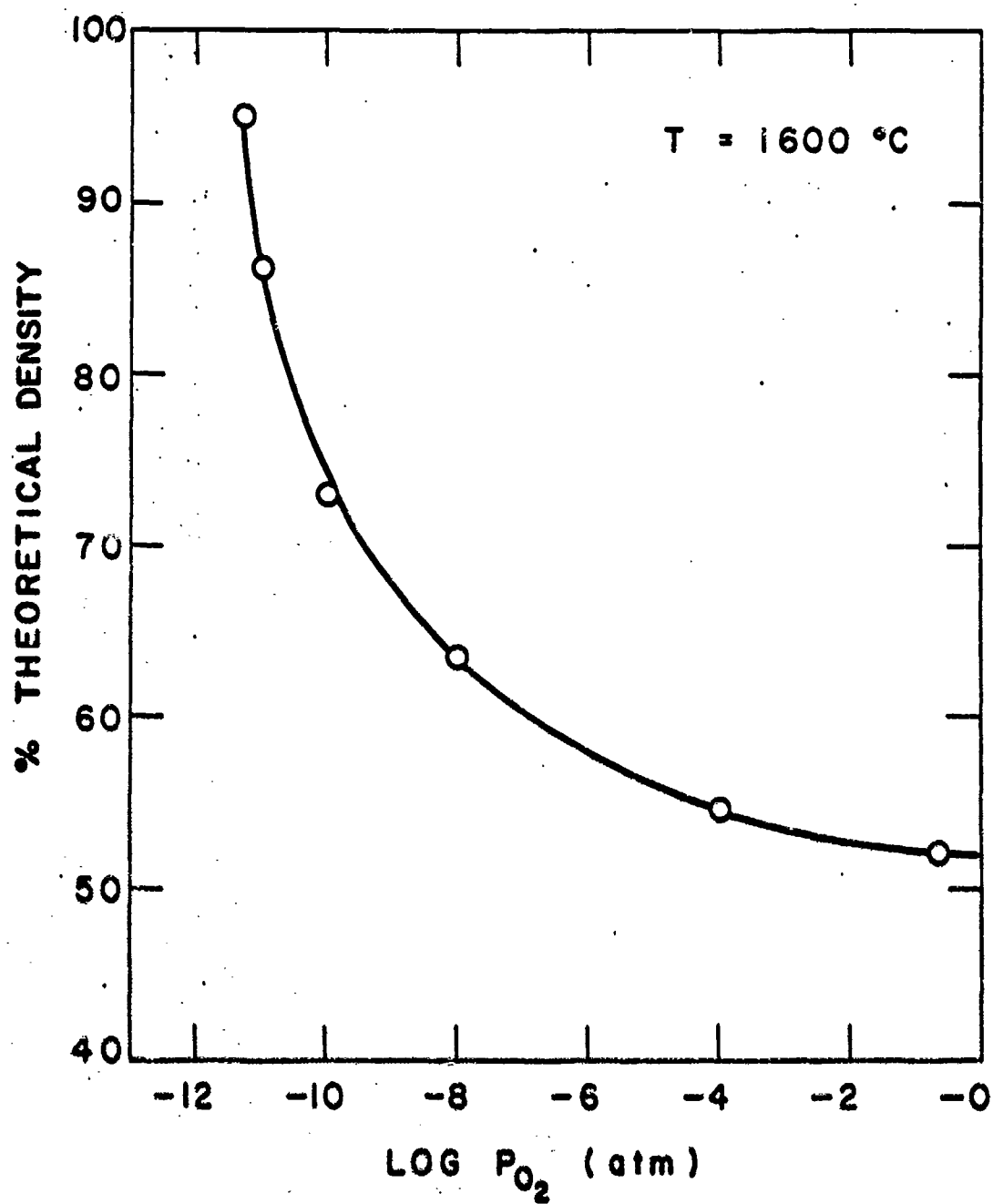


Figure 4.1: The final density of sintered samples of Cr_2O_3 as a function of the oxygen partial pressure

pressure of 1 atm.. Practically the P_{CO_2}/P_{CO} ratios were controlled by fixing the relative amount of the CO, CO₂ gases through flow meters. In order to avoid thermal diffusion effects due to the different weights of these two gases, Darken and Gurry (75) have pointed out that a total flow rate of 0.9 cm/sec has to be maintained.

There are two restrictions in the utilization of the CO/CO₂ mixture method. The first restriction comes from the possible occurrence of carbon precipitation which is depicted as the shaded area in Figure 4.2. As a result, there is a limit to the lowest P_{O_2} that may be attained by this gas mixture. The second restriction related to the flowmeters. It is virtually impossible to control very slow flow rates (< 0.005 cc/sec) by currently available flowmeters. In turn, it is very difficult to control a gas ratio below 1/500. This restriction further limits the range of the oxygen partial pressures available by this method.

Since the purity of commercial gases is generally much less than needed in the laboratory, all the gases used had to be cleaned before flowing into the reaction tube. The cleaning systems for the different gases are illustrated in Fig.4.3.

4.2 Sample Characterization

The sample characterization techniques utilized are X-ray Diffraction, Scanning Electron Microscope (SEM) and Chemical Analysis by Plasma Emission Spectrometer and Atomic Absorption Spectrophotometer.

The solubility of the dopants (TiO₂ and MgO) in Cr₂O₃ were examined by an automated X-ray diffractometer (Philips APD 3600/01) with CuK α radiation at a step increment of 0.02°2 θ and counting time of 1 sec.. The phase identification

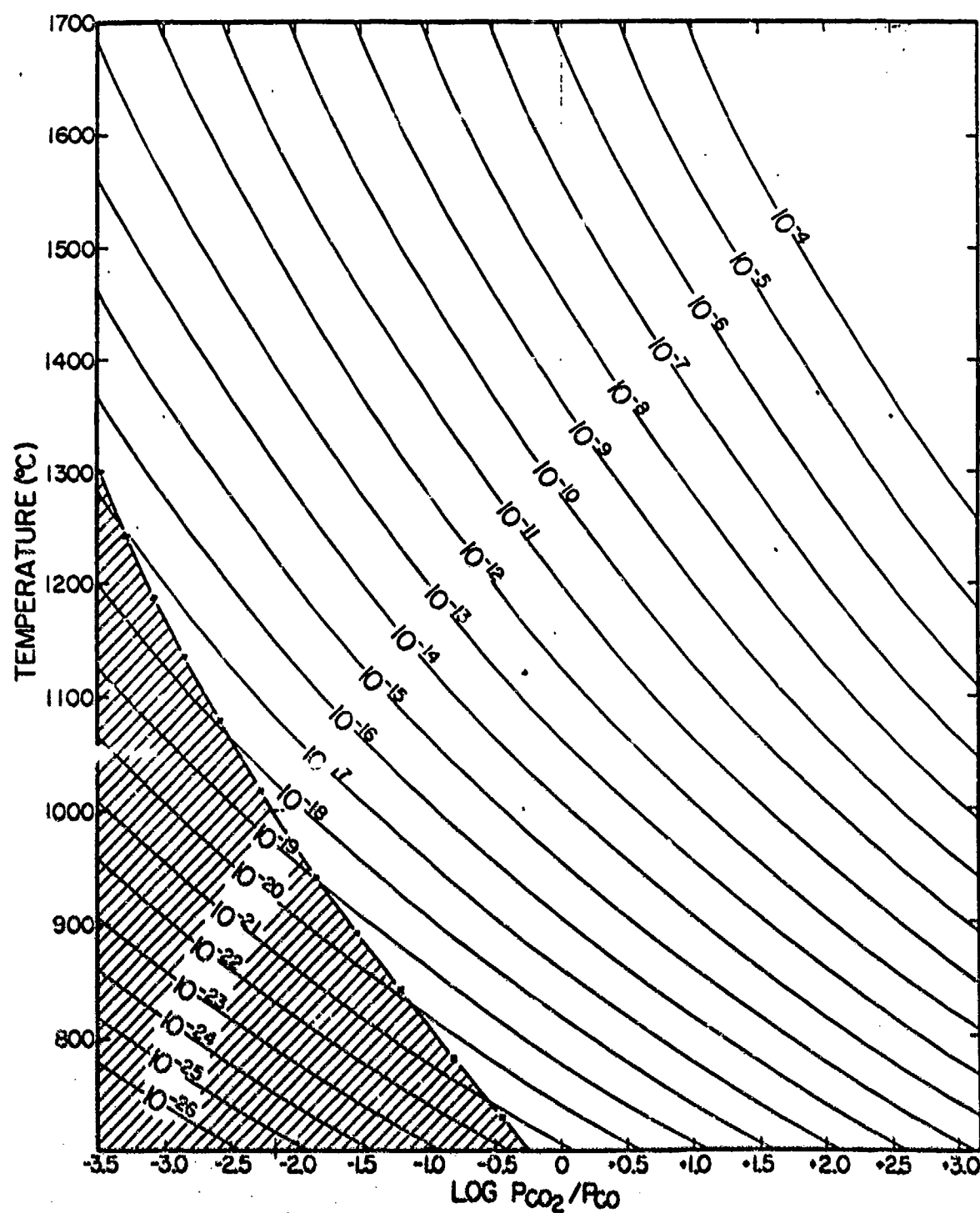


Figure 4.2: Oxygen pressures (atm) as a function of temperature and CO_2/CO ratios at a total pressure of 1 atm. (Ref. 75)

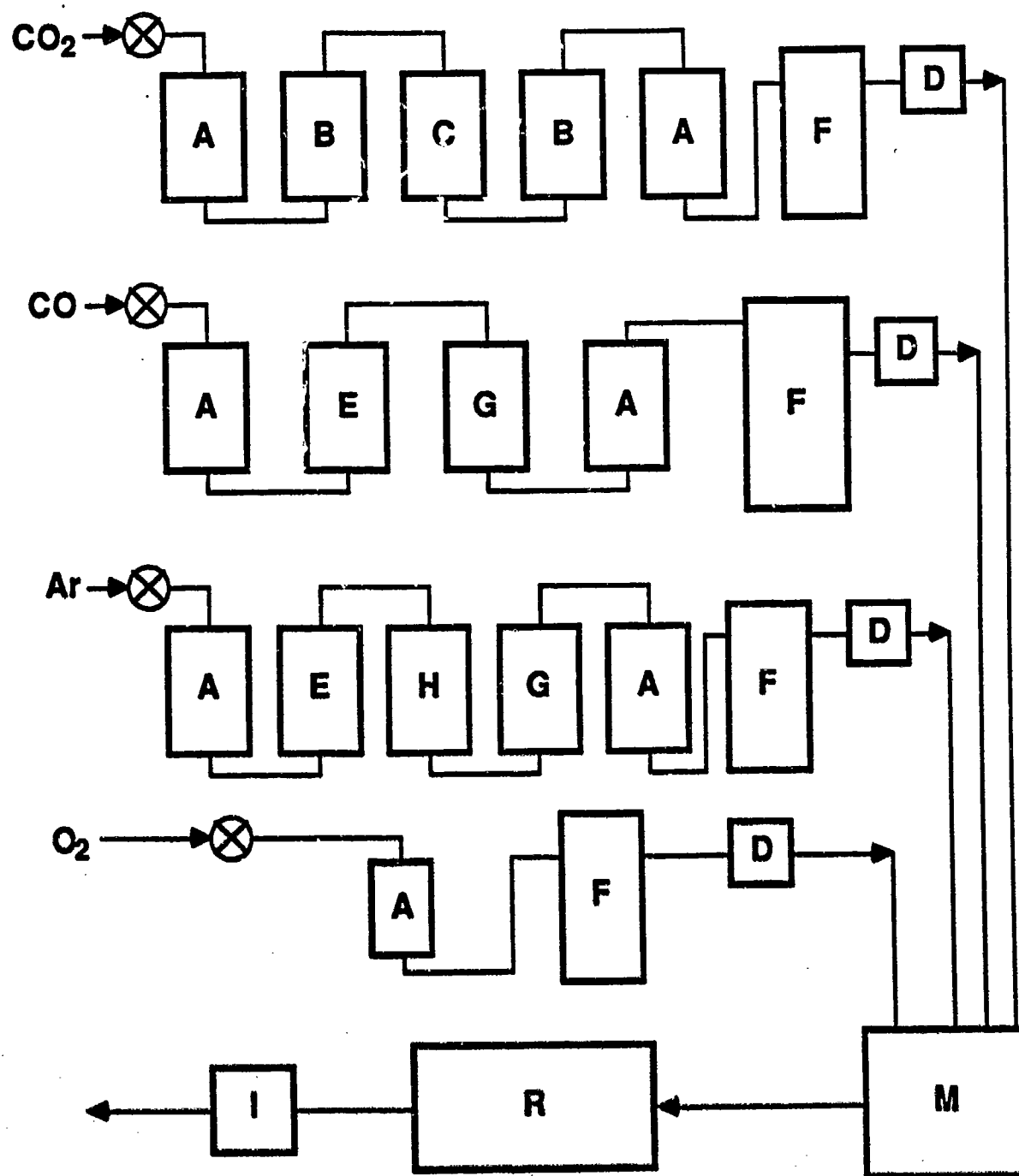


Figure 4.3: Entire gas atmosphere preparation arrangement.
 A. Drierite; B. Activated Al₂O₃; C. Cu/Cu₂O catalyst; D. Three-way stopcock;
 E. Active carbon; F. Flowmeter; G. Ascarite; H. Magnesium trap; I. Bubbler;
 M. Mixing chamber; R. Reaction tube.

was done in a routine manner using the JCPDS (Joint Committee on Powder Diffraction Standards) card. The calculations of the lattice parameters were performed by the APPLEMAN program in a VAX computer.

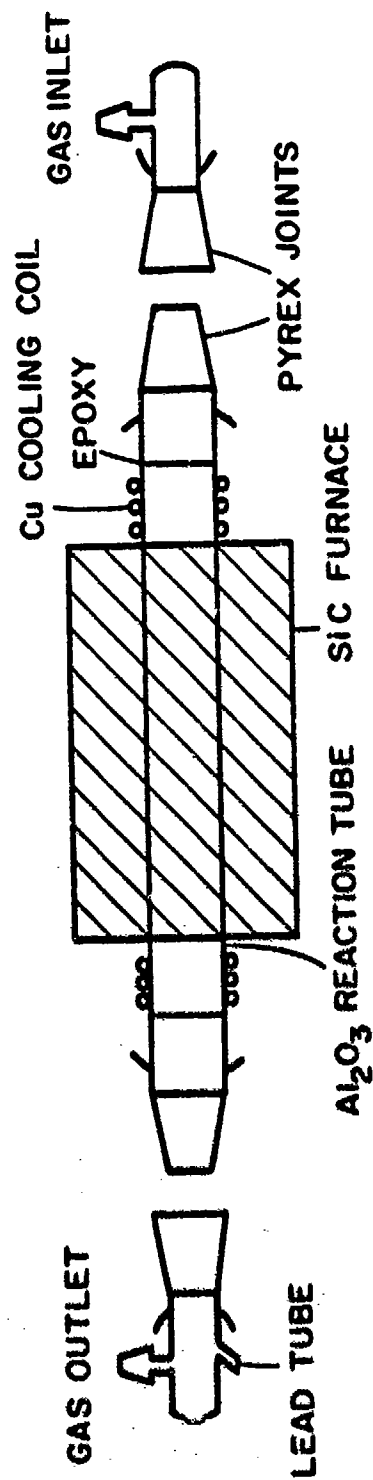
The microstructures of the sintered specimens were examined using an International Scientific M-7 Scanning Electron Microscope operated at 40KV. The SEM was also used for the identification of the second phase.

The dopant contents were examined by spectrometers. While TiO_2 contents were examined by SMI Spectraspan III Plasma Emission Spectrometer using National Bureau of Standard's No. 77a as standard, the MgO contents were checked by Perkin-Elmer model 703 Atomic Absorption Spectrophotometer using NBS No. T-1 as standard. The solutions were prepared by the following procedure: (1) samples were first ground into powder of < 100 mesh in size; (2) 20 mg of the ground powder was mixed with 180 mg of SiO_2 (3) this was then mixed with 1 gm of Lithium Metaborate (used as a fluxer); (4) The mixture was fused in a carbon crucible at 1000°C for 10 minutes; and, (5) then poured into 40% HNO_3 and magnetically stirred for 30 minutes.

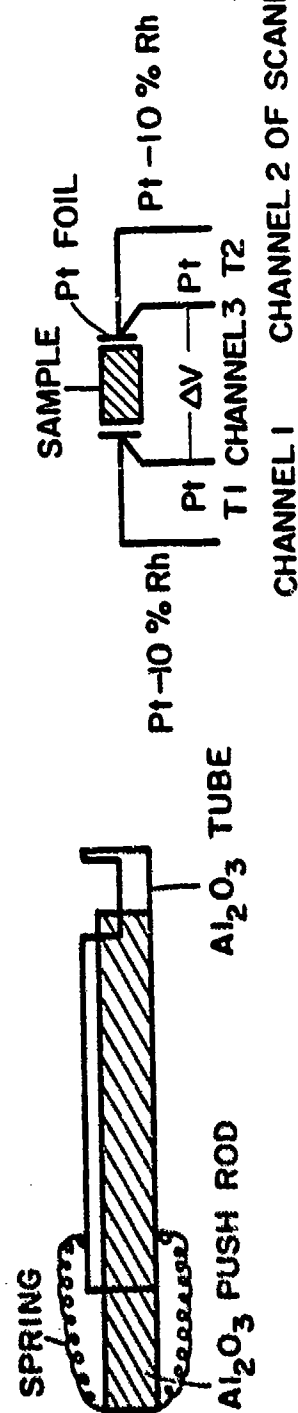
4.3 Electrical Conductivity and Seebeck Coefficient Measurements

The apparatus of the electrical conductivity and Seebeck Coefficient measurements is shown in Figure 4.4. It consist of an all alumina sample holder and two pieces of platinum foil electrodes to which Pt-Pt10%Rh thermocouples were attached. The sample was mechanically held between the electrodes with an Al_2O_3 push rod.

In the electrical conductivity measurement AC resistances were measured with a GenRad 1658 RLC Digibridge at 100 and and 1K Hz. by the four wire



(a)



(c)

(b)

Figure 4.4: Experimental arrangement for the electrical conductivity and Seebeck coefficient measurements. (a) reaction tube and furnace (b) sample holder (c) connections of the electrodes

method. The Pt-10%Rh leads of the electrodes served as current probes and the Pt leads as voltage probes. An IBM personal computer capable of communicating with the Digibridge through an I-EEE 488 bus was used for data collection. During experiments the sample's resistance was monitored as a function of time. The kinetic data were used to determine the equilibrium time needed for the sample to react with the atmosphere employed. A computer program written for this purpose is presented in Appendix 1. Occasionally, DC resistances were also measured for comparison, no apparent difference has been observed.

Seebeck coefficient experiments were performed on the same sample after the electrical conductivity measurements. Temperature gradients were achieved by shifting the sample's position slightly away from the hot zone while the furnace temperature was controlled to maintain the sample at the same average temperature. The Pt-Pt10%Rh thermocouples were used to measure the temperature while the Pt leads were used for the Seebeck voltage by taking the lower temperature end as positive. A block diagram of the equipment utilized in Seebeck coefficient measurement is shown in Figure 4.5.. The Nanovoltmeter (Keithley model 181) was used to measure both temperatures and Seebeck voltages, and the Scanner (Keithley model 705) served as a switching device between the nanovoltmeter and different voltage inputs, i.e., the two temperatures and the Seebeck voltage. The I-EEE 488 bus was still used for communication among these instruments and the IBM Personal Computer. The computer program for this experiment is presented in Appendix 2. The Seebeck coefficient Q was determined from the slope of the linear dependence of $\Delta V = f(\Delta T)$. As illustrated in Figure 4.6, eight temperature gradients were measured in the experiments for the calculation of Q .

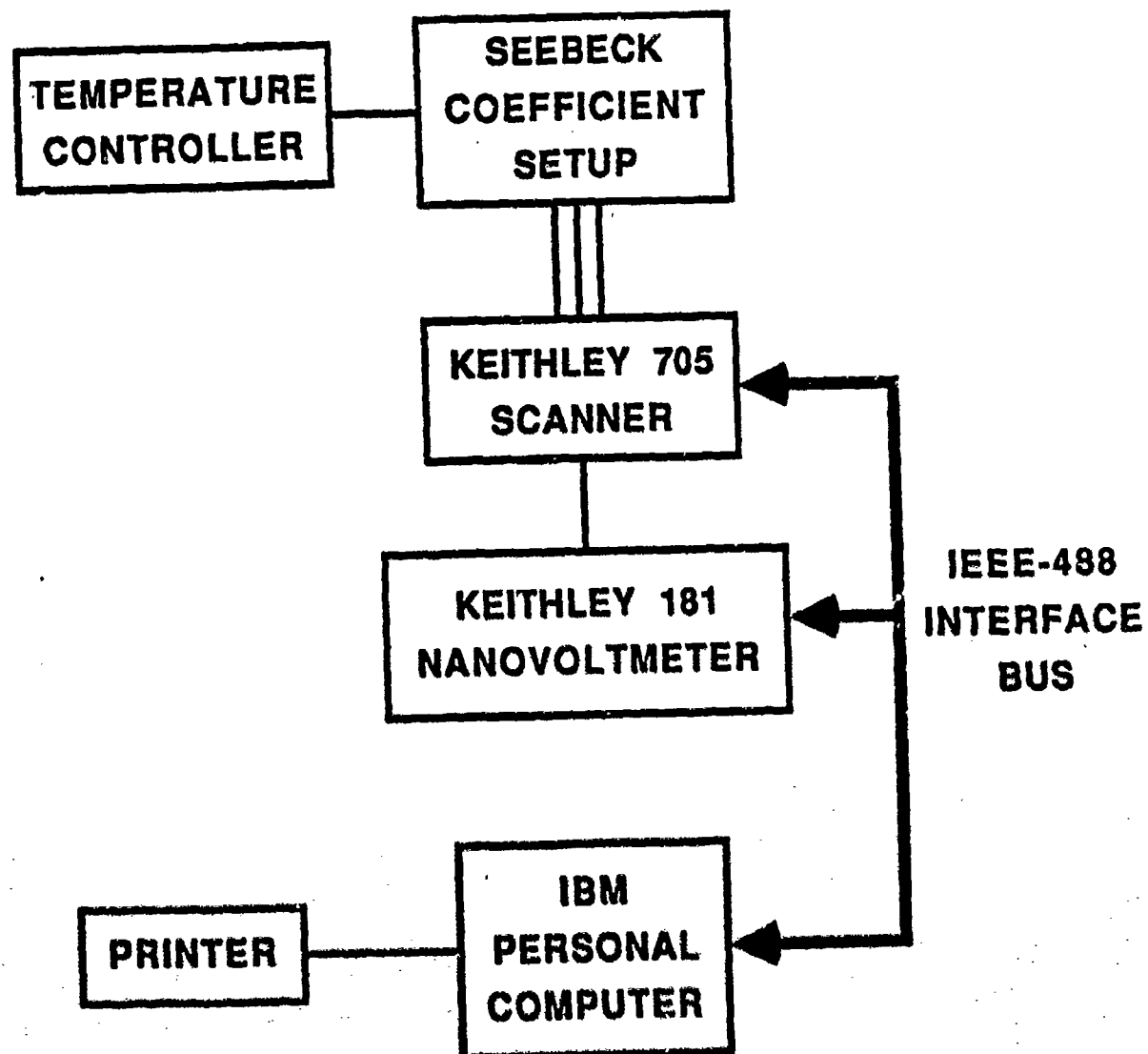


Figure 4.5: Block diagram of the apparatus of the Seebeck coefficient measurement.

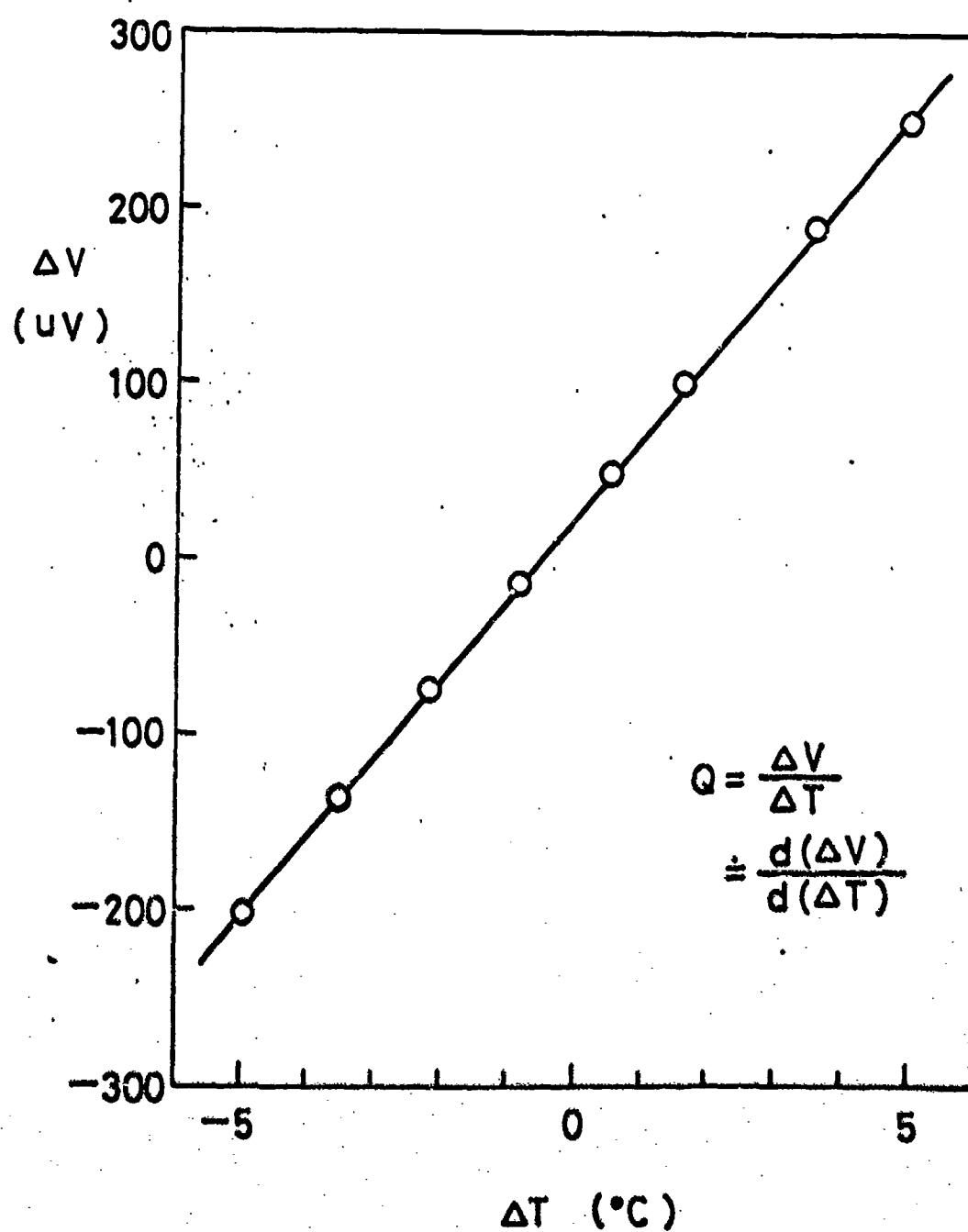


Figure 4.6: Determination of Seebeck coefficient from experimental data. Seebeck coefficient is calculated from the slope of $\Delta V = f(\Delta T)$.

Both electrical conductivities and Seebeck coefficients were measured as functions of temperature and P_{O_2} , where the P_{O_2} 's were still controlled by O_2/Ar and CO/CO_2 gas mixtures.

Chapter 5

ELECTRICAL CONDUCTIVITY AND SEEBECK COEFFICIENT OF TiO_2 -DOPED Cr_2O_3

In this study the electrical conductivities and Seebeck coefficients of TiO_2 -doped Cr_2O_3 were measured as a function of P_{O_2} , temperature and dopant content. As a general feature, the results indicate that doping with higher valent cations (Ti) into Cr_2O_3 will increase the electron conductivity. A very special behavior characterized by a conductivity minimum in the conductivity vs P_{O_2} diagram was observed for all specimens. Based on these results, the major point defects of Cr_2O_3 in the high P_{O_2} region were determined. In this chapter, the results, analyses and discussions are presented in detail.

5.1 Results

5.1.1 Experimental Equilibrium Time

It is of much interest to determine the time needed for a Cr_2O_3 specimen to equilibrate with the environmental atmosphere during experiments. Based on some preliminary studies, the author found that it is very difficult for a dense sample to reach equilibrium. An equilibrium time of days, even weeks, may be needed. In order to obtain appropriate information within a reasonable experimental time span, it was decided to use both porous and dense specimens. Porous samples, which could equilibrate to changing oxygen atmospheres more rapidly, were used to determine P_{O_2} dependence behavior while dense samples were used to determine the true electrical conductivity for comparison, which in turn were also utilized to calculate the mobility of electronic carriers. Figure 3.1

shows a typical kinetic diagram of the resistance measurement on an 0.5 mole% TiO_2 -doped Cr_2O_3 porous sample. It is seen that at 1100°C an equilibrium time of 8 hours was required. Throughout this study, conductivities were calculated from measured resistance by $\sigma = L/AR$, where L is the sample length and $A = \pi r^2$, r is the radius of the sample. Also σ will be used for the notation of the true conductivity, and σ_{eff} for conductivity measured from porous samples.

5.1.2 Electrical Conductivity

The experimental results of the electrical conductivity are plotted in Figures 5.2 to 5.5 as a function of oxygen partial pressure and TiO_2 content, ranging from 0.1 to 0.5 mole%, at temperatures from 1000° to 1300°C . Several interesting characteristics of these curves are described in the following.

(1) Oxygen partial pressure dependence

1. A conductivity minimum appears at an oxygen partial pressure $P_{\text{O}_2}^0$.
2. At $P_{\text{O}_2} > P_{\text{O}_2}^0$, the conductivity varies as $P_{\text{O}_2}^{1/x}$, where x is about 4, which indicates a typical p-type semiconductor behavior.
3. At $P_{\text{O}_2} < P_{\text{O}_2}^0$, the conductivity varies as $P_{\text{O}_2}^{1/x}$, where x is about -4, which indicates a N-type semiconductor behavior.
4. At even lower P_{O_2} , the slope of the conductivity curve becomes smaller and tends to reach zero after a certain P_{O_2} . Apparently, when P_{O_2} is decreased below this inflection point, the electrical conductivity is governed by the dopant content. This inflection point is denoted as $P_{\text{O}_2}^d$.

(2) Composition dependence

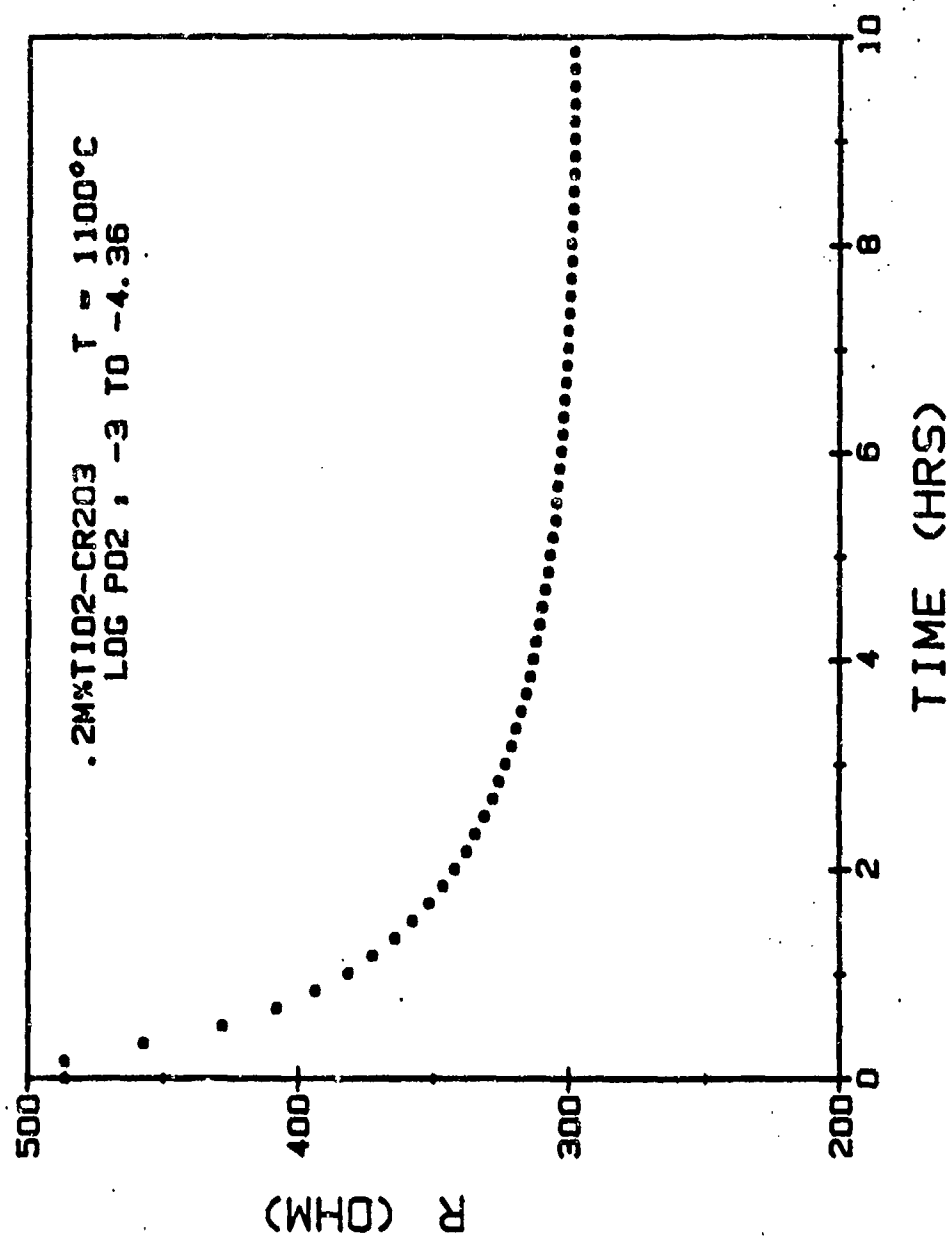


Figure 5.1: Kinetic diagram of measured resistance of a porous Cr₂O₃ sample.

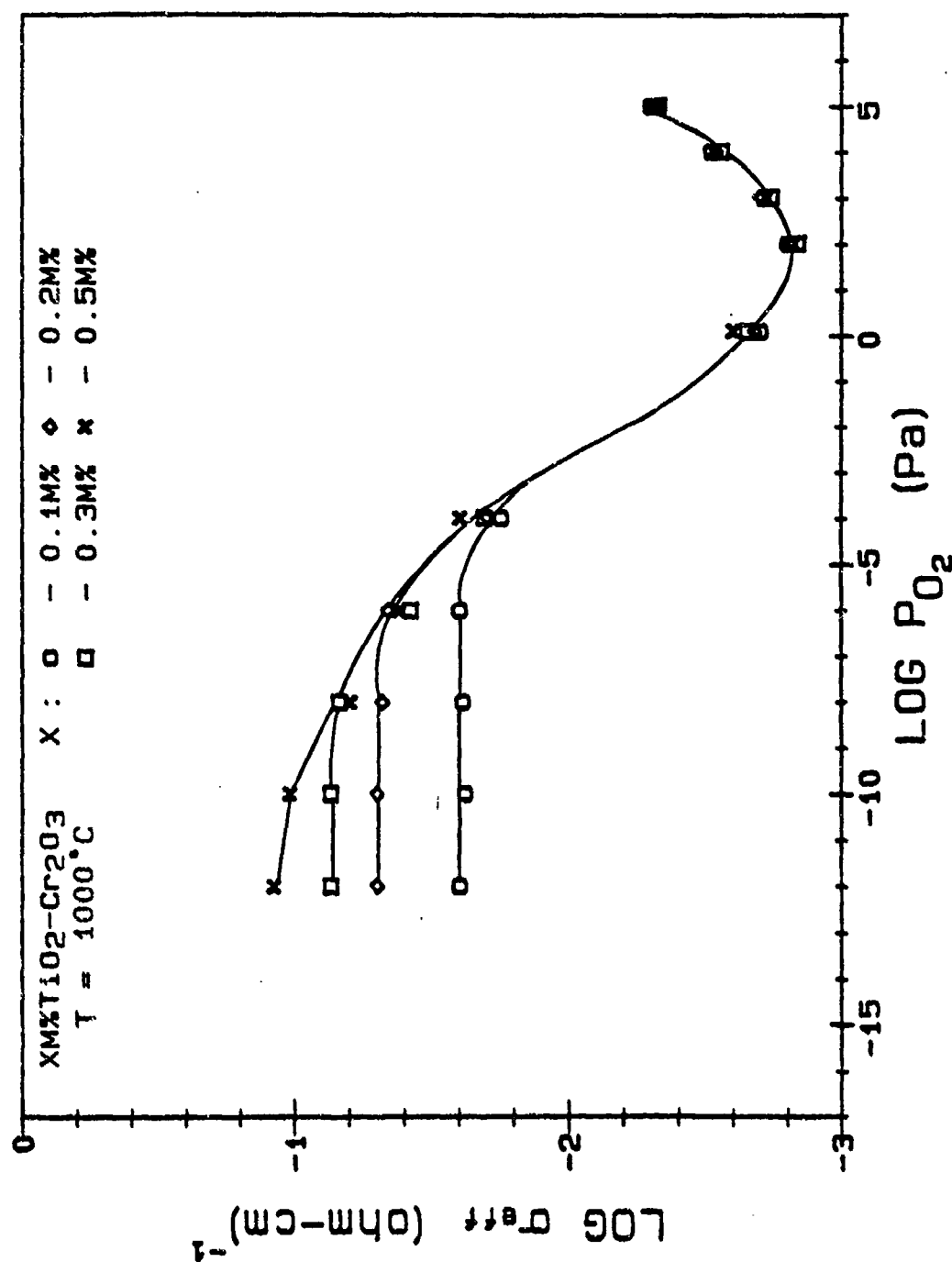


Figure 5.2: Electrical conductivity of TiO_2 -doped Cr_2O_3 at 1000°C .

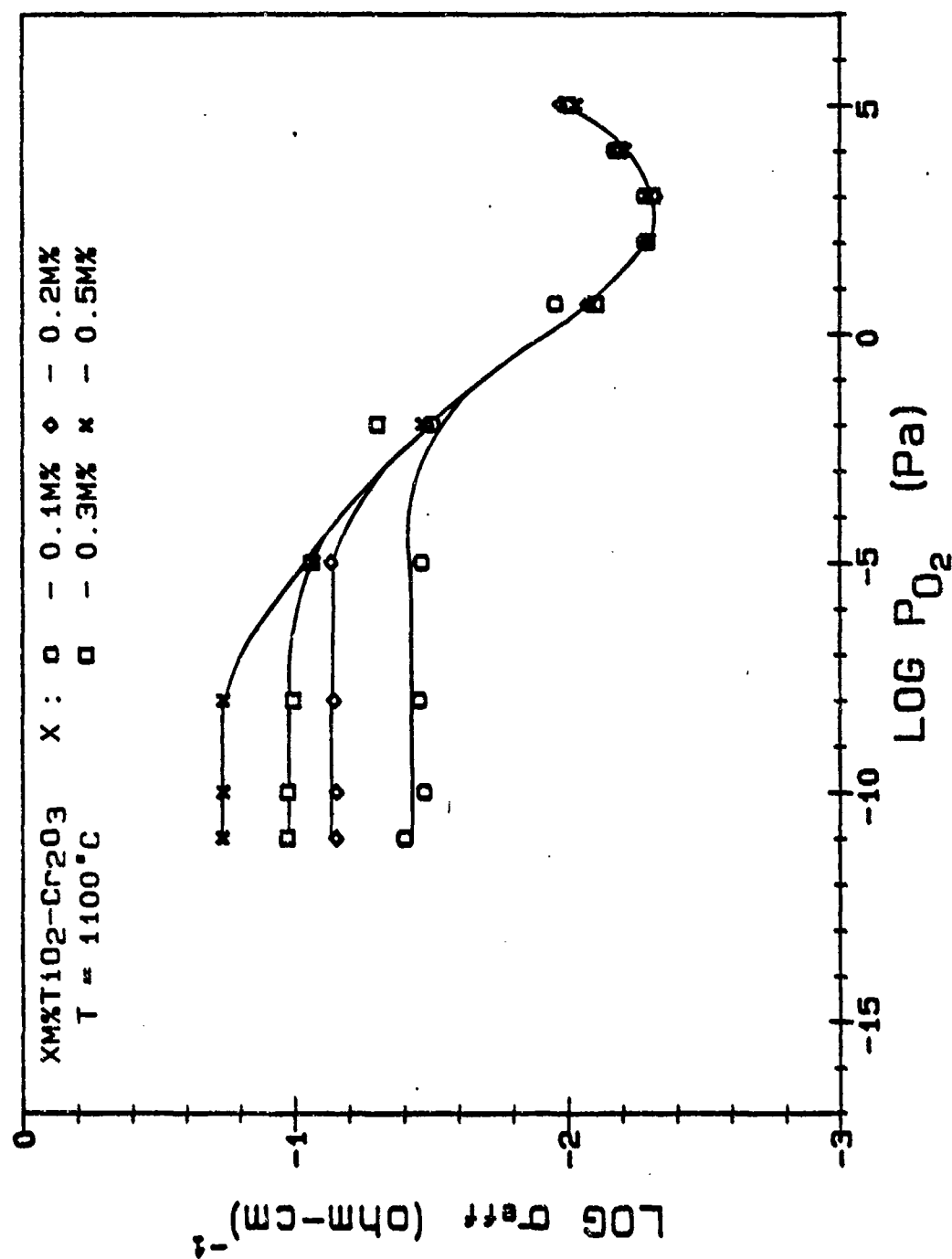


Figure 5.3: Electrical conductivity of TiO_2 -doped Cr_2O_3 at 1100°C .

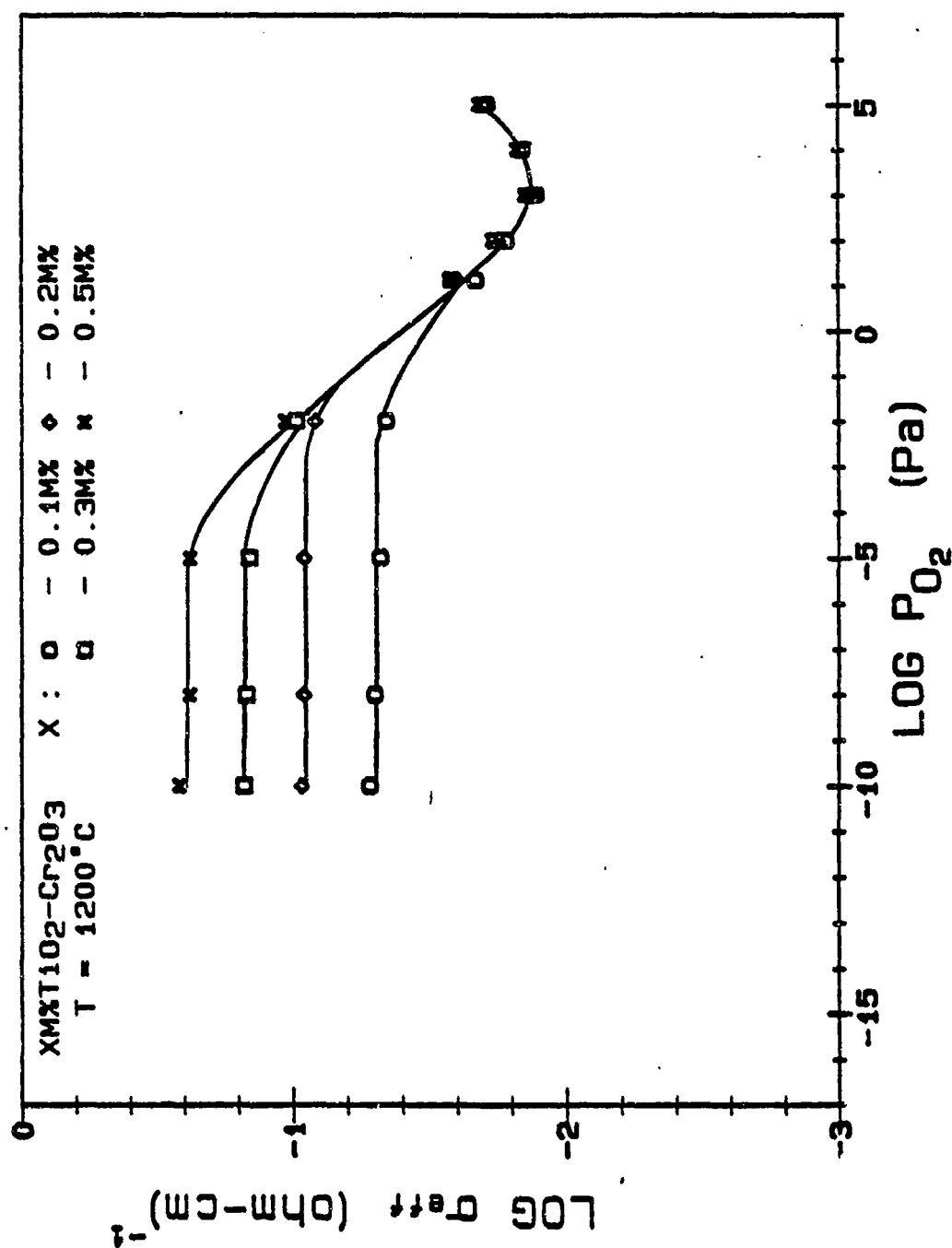


Figure 5.4: Electrical conductivity of TiO₂-doped Cr₂O₃ at 1200°C.

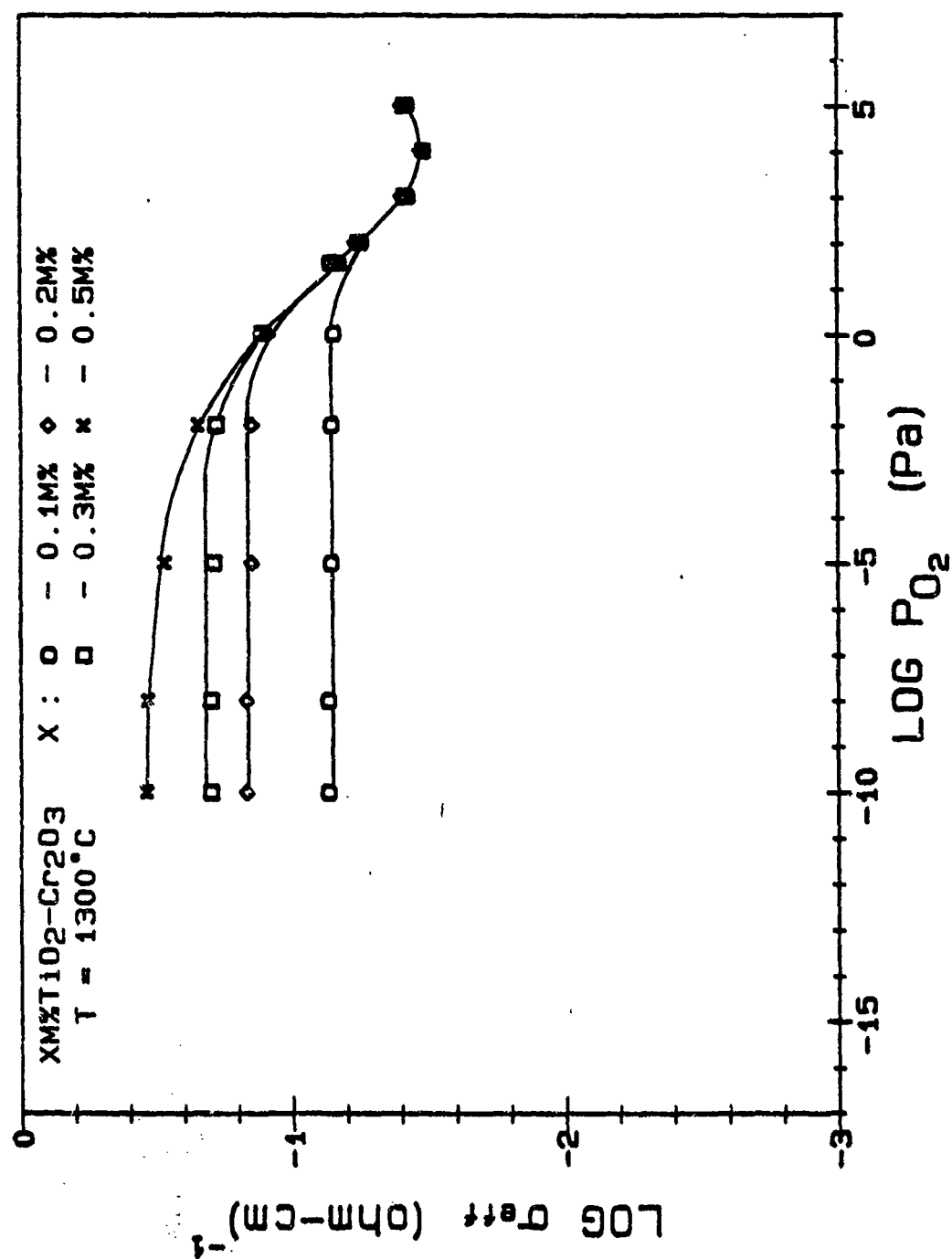


Figure 5.5: Electrical conductivity of TiO_2 -doped Cr_2O_3 at 1300°C .

1. In the high P_{O_2} region, the electrical conductivity does not vary with the doped TiO_2 content.
 2. In the low P_{O_2} region, the electrical conductivity appears to be proportional to the dopant content.
- (3) Temperature dependence

The temperature dependence of the electrical conductivity is illustrated in Figure 5.6. It appears that both the conductivity minimum ($P_{O_2}^g$) and the inflection point ($P_{O_2}^d$) shift to higher P_{O_2} at higher temperatures.

5.1.3 Seebeck Coefficient

The corresponding Seebeck coefficients are shown in Figures 5.7 and 5.8. The results are in excellent agreement with the electrical conductivity. At high P_{O_2} 's, the Seebeck coefficient Q is positive while it is negative at low P_{O_2} 's. The occurrence of the reversal in the sign of Q near $P_{O_2}^g$ indicates a change of the transport mechanism from P-type to N-type conductivity in that vicinity. Also, constant negative values of Q 's for $P_{O_2} < P_{O_2}^d$ implies a constant electron concentration in that region. Furthermore, the P_{O_2} at which $Q = 0$ shifts with temperature somewhat like that for the conductivity minimum. (Figure 5.11)

5.2 Analyses and Discussions

5.2.1 Point Defect Structure of Cr_2O_3

Although the point defect structure of Cr_2O_3 has been shown to be very complicated, it is generally concluded that the following defects may be the major defects present in the crystal : V_{Cr}''' , Cr_i''' , h' and e' . The defect equations between the defects can then be written as

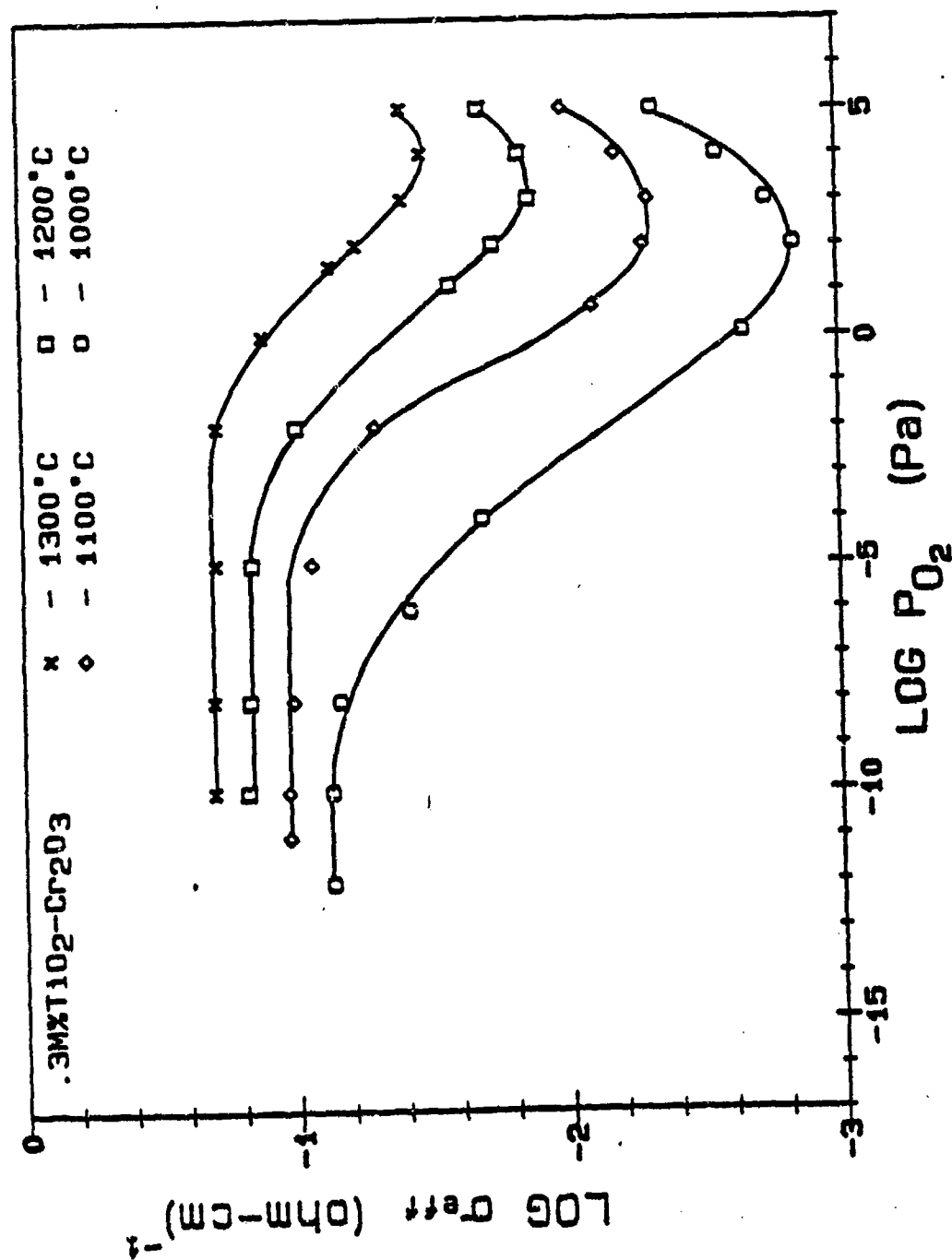


Figure 5.6: Electrical conductivity of TiO₂-doped Cr₂O₃ as a function of temperature.

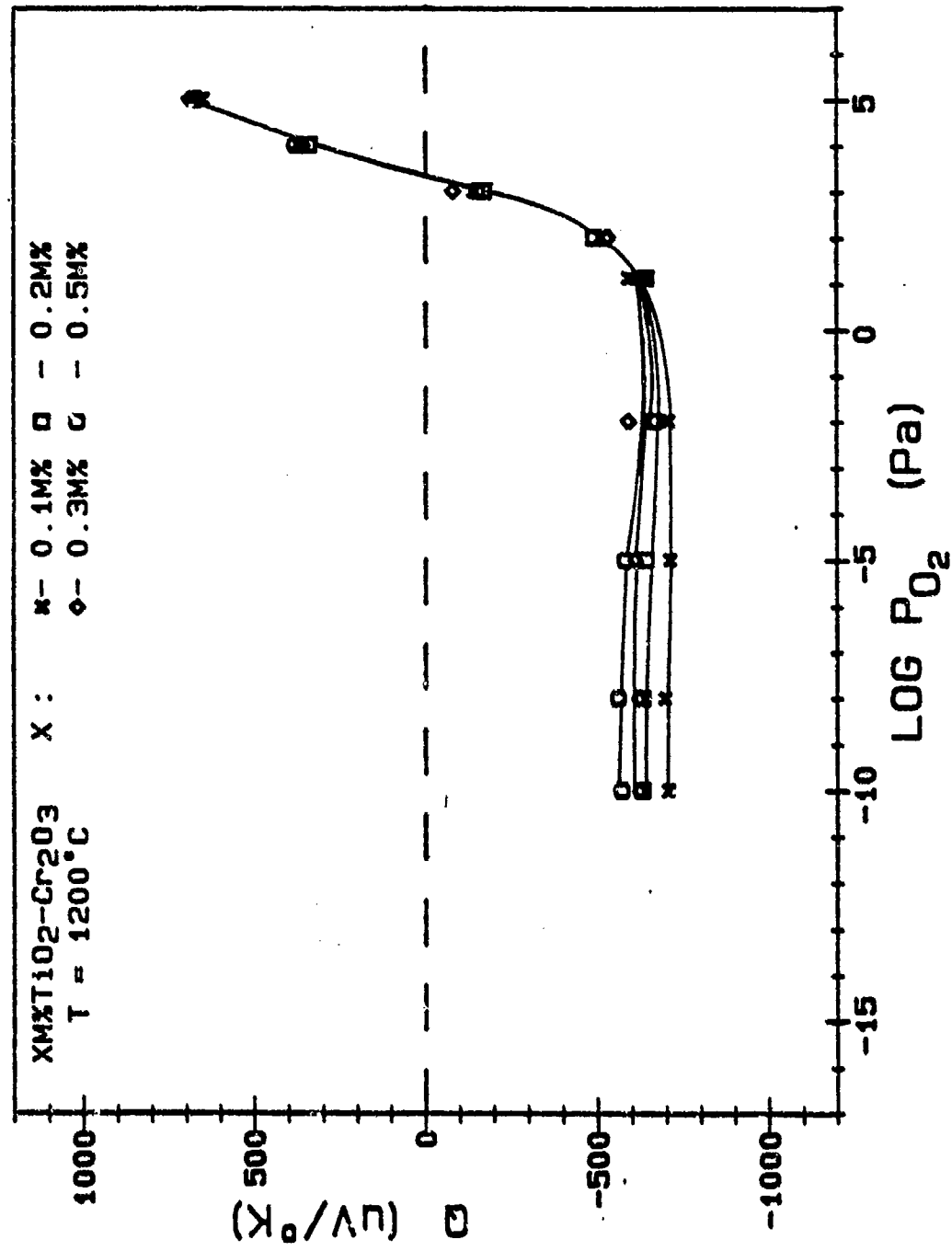


Figure 5.7: Seebeck coefficient of TiO_2 -doped Cr_2O_3 at 1200°C .

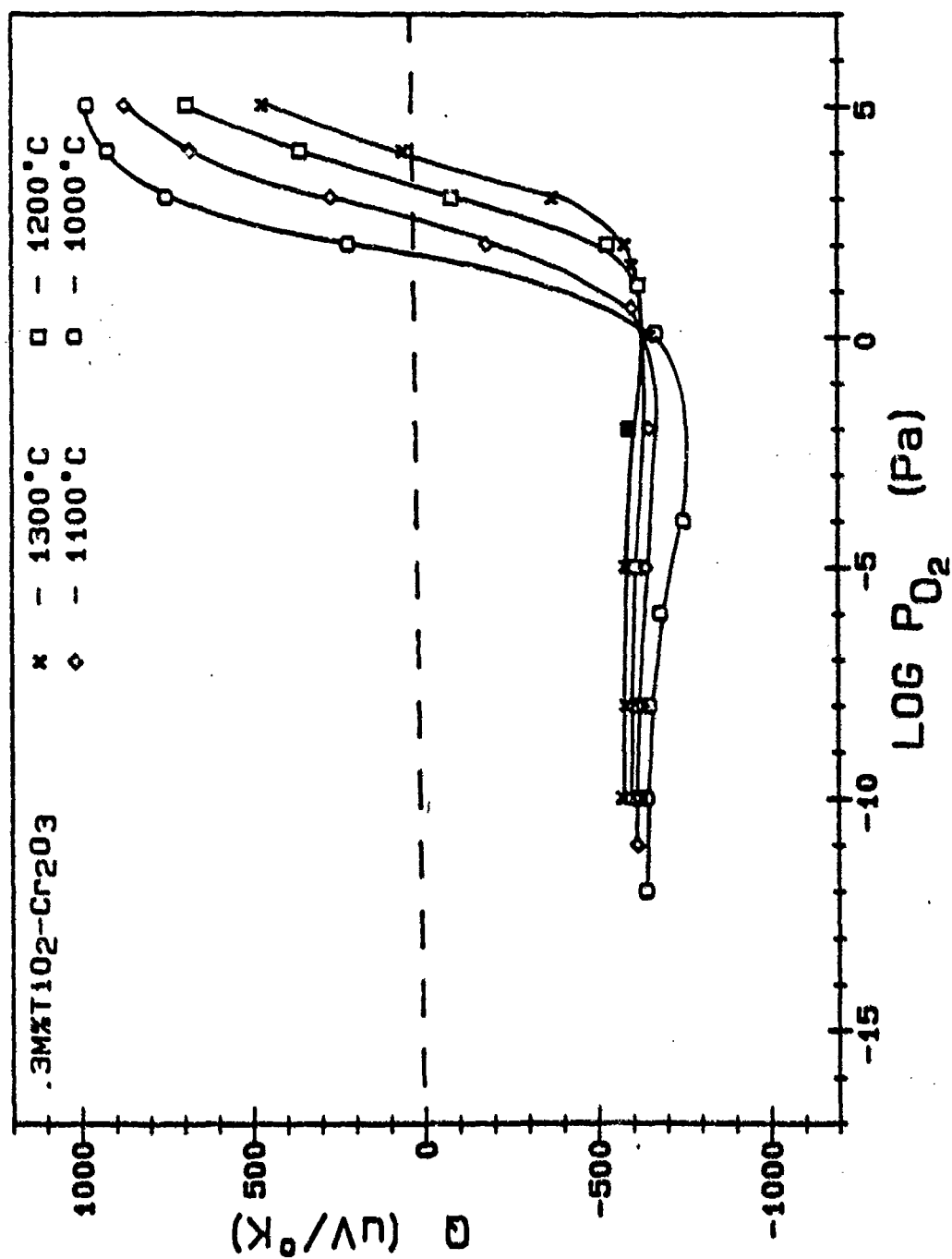


Figure 5.8: Seebeck coefficient of TiO₂-doped Cr₂O₃ as a function of temperature.



Equation 5.1 represents the formation of the defects of a P-type, metal deficit semiconductor; equation 5.2 represents the formation of the defects of a N-type metal excess semiconductor; equation 5.3 represents the formation of the intrinsic electronic defects; and, equation 5.4 represents the formation of Frenkel defects.

Applying the mass action law to the above reactions leads to the following equations :

$$K_{\text{V}_{\text{Cr}}^{\prime\prime\prime}} = [\text{V}_{\text{Cr}}^{\prime\prime\prime}]^2 \cdot [\text{h}^{\cdot}]^6 \cdot \text{P}_{\text{O}_2}^{-3/2} \quad (5.5)$$

$$K_{\text{Cr}_i^{\prime\prime}} = [\text{Cr}_i^{\prime\prime}]^2 \cdot [\text{e}^{\cdot}]^6 \cdot \text{P}_{\text{O}_2}^{3/2} \quad (5.6)$$

$$K_i = [\text{e}^{\cdot}] \cdot [\text{h}^{\cdot}] \quad (5.7)$$

$$K_F = [\text{V}_{\text{Cr}}^{\prime\prime\prime}] \cdot [\text{Cr}_i^{\prime\prime}] \quad (5.8)$$

In addition to equations 5.5 to 5.8, the electroneutrality equation gives

$$[\text{h}^{\cdot}] + 3[\text{Cr}_i^{\prime\prime}] = [\text{e}^{\cdot}] + 3[\text{V}_{\text{Cr}}^{\prime\prime\prime}] \quad (5.9)$$

In all these equations, the square brackets indicate the concentration of the defect involved (in $\text{\#}/\text{cm}^3$). In order to obtain the defect structure of Cr_2O_3 , all these K's need to be obtained.

5.2.2 Defect Structure of TiO_2 -Doped Cr_2O_3

When a higher valent cation (Ti) is incorporated in Cr_2O_3 , the substitution of Ti^{4+} ion into the Cr^{3+} site will generate a positive charge. In order to maintain

the electroneutrality condition, compensation by the creation of negative charged defects are required. Both V_{Cr}''' and e' are possible candidates, and the processes may be represented by the following equations.

In the case of V_{Cr}''' :



$$K_{TiCr1} = [Ti_{Cr}]^3 \cdot [V_{Cr}'''] \quad (5.11)$$

When the dopant concentration $[Ti_{Cr}]$ is much higher than the intrinsic defect concentration, the Cr vacancy concentration is determined by

$$[V_{Cr}'''] = 1/3[Ti_{Cr}] = 3^{-3/4} \cdot K_{TiCr1}^{1/4} \quad (5.12)$$

and is independent of the oxygen partial pressure.

In the case of e' :



$$K_{TiCr2} = [Ti_{Cr}]^2 \cdot [e']^2 \cdot P_{O_2}^{1/2} \quad (5.14)$$

when $[Ti_{Cr}]$ is much greater than the intrinsic defect concentrations, then $[e']$ is controlled by $[Ti_{Cr}]$ through

$$[e'] = [Ti_{Cr}] = K_{TiCr2}^{1/4} \cdot P_{O_2}^{-1/8} \quad (5.15)$$

The appearance of the $P_{O_2}^{-1/8}$ dependence indicates that the solubility of TiO_2 in Cr_2O_3 may vary with the oxygen partial pressure. The solubility increases as P_{O_2} decreases. When the dopant content is higher than the solubility, a second phase TiO_2 appears (Equation 5.13). When both cases are considered, a new electroneutrality condition is applied, that is,

$$[Ti_{Cr}] + [h'] = 3[V_{Cr}'''] + [e'] \quad (5.16)$$

Theoretically, combining these equations with Equations 5.5 and 5.6, one may solve for the four unknown defect concentrations in terms of the equilibrium constants and the P_{O_2} . With a prior knowledge of these equilibrium constants

the relationship between the concentrations of the different defects and P_{O_2} can be obtained. However, when these K 's are not available, this approach becomes too complicated to follow. Thus it is reasonable to use an approximation method. In this study the method developed by Kröger and Vink (6) is adopted. In this method, these equations are solved in a piecewise linear fashion by sequentially choosing conditions for which only one term on each side of the electroneutrality equation need be considered. In other words, only the two defects with the highest concentration in the chosen condition are considered. For example, under heavily oxidizing conditions, the electroneutrality equation may be simplified to

$$[h'] = 3[V_{Cr}^{''}] \quad (5.17)$$

Combining this with Equation 5.5, one obtains

$$[h'] = 3[V_{Cr}^{''}] = 3^{1/4} \cdot K_{V_{Cr}^{''}}^{1/8} \cdot P_{O_2}^{3/16} \quad (5.18)$$

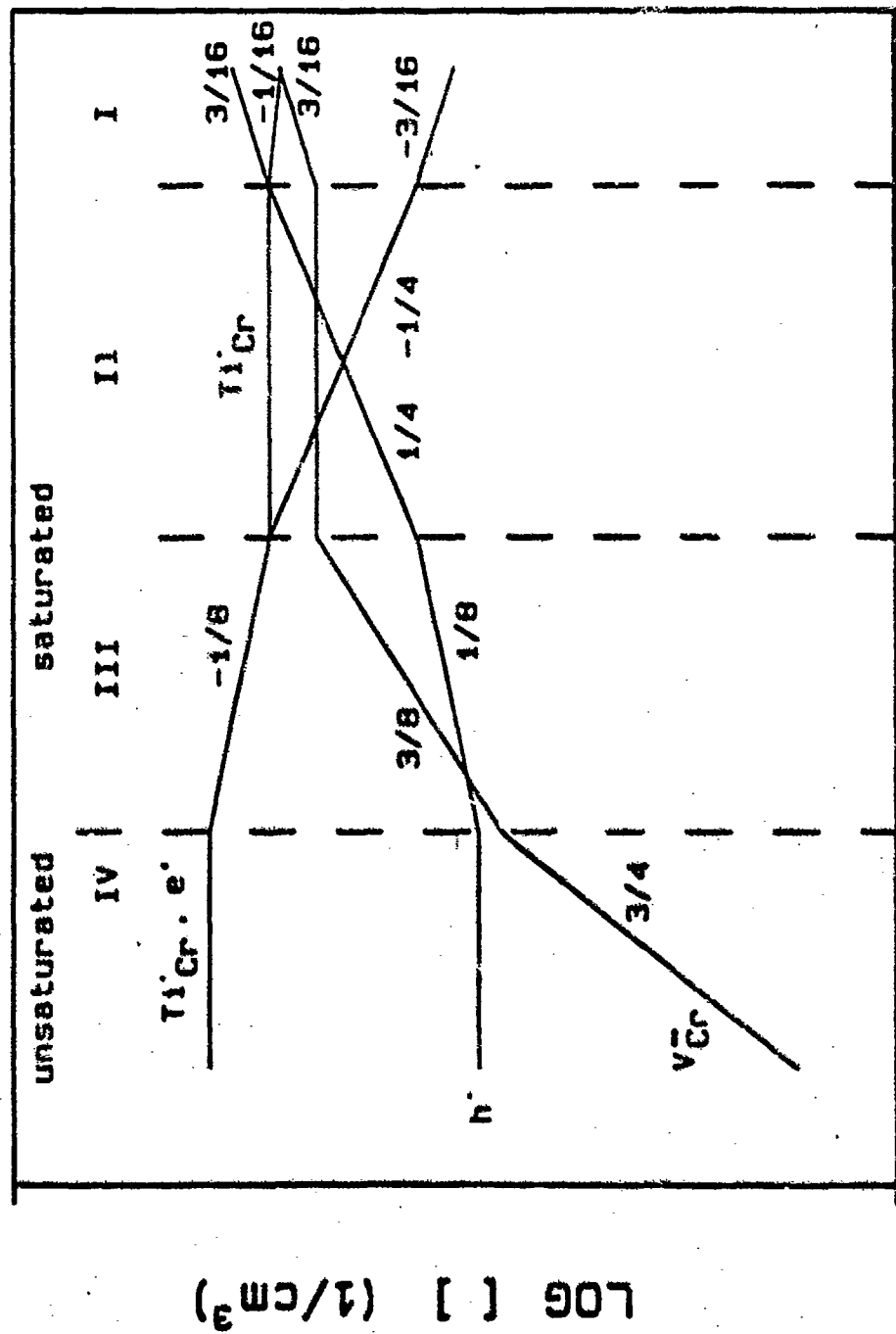
and from Equations 5.6 and 5.13,

$$[e'] = 3^{1/4} \cdot K_1 \cdot K_{V_{Cr}^{''}}^{1/8} \cdot P_{O_2}^{3/16} \quad (5.19)$$

$$[Ti_{Cr}] = 3^{1/4} \cdot K_{Ti_{Cr}}^{1/4} \cdot K_{V_{Cr}^{''}}^{1/24} \cdot P_{O_2}^{1/16} \quad (5.20)$$

The other defect regions can then be determined with successively decreasing P_{O_2} , which gives $[Ti_{Cr}] = 3[V_{Cr}^{''}]$ and $[Ti_{Cr}] = [e']$. A diagram depicting the P_{O_2} dependence of the defects over the different regions is presented in Figure 5.9. Also Table 2 gives the calculated results of the defect concentrations in different regions. It is noted that region IV represents the unsaturated region, a region where the level of the dopant content is below the solubility limit.

It is of interest at this point to compare the defect structure model with the experimental results. When the variations of $[h']$ and $[e']$ to the P_{O_2} 's in Figure 5.9, and that of the σ in the results were examined, an excellent match was found. This fact suggests that the proposed model may represent the defect



LOG P_{O2}

Figure 5.9: A model of the defect structure of TiO_2 -doped Cr_2O_3 .

Table 2: Calculated defect concentrations as functions of different equilibrium constants

	Unsaturated	Saturated
Region	IV	III
Electroneutrality	$[\text{Ti}_{\text{Cr}}] = [\text{e}^-]$	$[\text{Ti}_{\text{Cr}}] = [\text{e}^-]$
PO_2 range	low	low
$[\text{V}_{\text{Cr}}^{\bullet\bullet}]$	$K_{\text{V}_{\text{Cr}}^{\bullet\bullet}} \cdot \text{PO}_2^{3/4}$	$K_1^{-3} K_{\text{Ti}_{\text{Cr}}2}^{3/4} K_{\text{V}_{\text{Cr}}^{\bullet\bullet}} \cdot \text{PO}_2^{-3/8}$
$[\text{h}^{\bullet}]$	$K_1 (\text{const.})^{-1}$	$K_1 K_{\text{Ti}_{\text{Cr}}2}^{-1/4} \text{PO}_2^{1/8}$
$[\text{e}^-]$	const.	$K_{\text{Ti}_{\text{Cr}}2}^{1/4} \text{PO}_2^{-1/8}$
$[\text{Ti}_{\text{Cr}}]$	const.	$K_{\text{Ti}_{\text{Cr}}2}^{1/4} \text{PO}_2^{-1/8}$

Region	II	I
Electroneutrality	$[\text{Ti}_{\text{Cr}}] = 3[\text{V}_{\text{Cr}}^{\bullet\bullet}]$	$[\text{h}^{\bullet}] = 3[\text{V}_{\text{Cr}}^{\bullet\bullet}]$
PO_2 range	intermediate	high
$[\text{V}_{\text{Cr}}^{\bullet\bullet}]$	$3^{-3/4} K_{\text{Ti}_{\text{Cr}}1}^{1/4}$	$3^{-3/4} K_{\text{V}_{\text{Cr}}^{\bullet\bullet}} \cdot \text{PO}_2^{3/16}$
$[\text{h}^{\bullet}]$	$K_{\text{V}_{\text{Cr}}^{\bullet\bullet}} \cdot \text{PO}_2^{1/4}$	$3^{1/4} K_{\text{V}_{\text{Cr}}^{\bullet\bullet}} \cdot \text{PO}_2^{3/16}$
$[\text{e}^-]$	$K_1 K_{\text{V}_{\text{Cr}}^{\bullet\bullet}} \cdot \text{PO}_2^{-1/4}$	$3^{-1/4} K_1 K_{\text{V}_{\text{Cr}}^{\bullet\bullet}} \cdot \text{PO}_2^{-3/16}$
$[\text{Ti}_{\text{Cr}}]$	$3^{1/4} K_{\text{Ti}_{\text{Cr}}1}^{1/4}$	$3^{1/4} K_{\text{Ti}_{\text{Cr}}1}^{1/4} K_{\text{V}_{\text{Cr}}^{\bullet\bullet}} \cdot \text{PO}_2^{-1/16}$

structure of TiO_2 -doped Cr_2O_3 . Accordingly, with the experimental data and this model one may construct the [defect] vs PO_2 diagram, and obtain information about the corresponding equilibrium constants.

5.2.3 Determination of the Intrinsic Electron Concentration n_i

In the process of constructing the [defect]- PO_2 diagram, the conductivity minimum, σ_{\min} , and the constant conductivity in region IV are two very useful parameters. According to Becker and Frederikse's analysis (76), the electrical conductivity, σ , of a semiconductor containing both electrons and electron holes can be expressed by

$$\sigma/\sigma_i = b^{1/2} \cdot (\alpha + 1)/(b + 1) \cdot \alpha^{1/2} \quad (5.21)$$

where $\sigma_i = n_i e(\mu_n + \mu_p)$ is the intrinsic conductivity, i.e., conductivity under the condition $n = p = n_i$, $b = (\mu_n/\mu_p)$ is the ratio of the electron and electron hole mobilities and $\alpha = (\sigma_p/\sigma_n) = (p/n \cdot b)$ is the ratio of the electron hole and electron conductivities. Since σ_{\min} occurs at $\sigma_n = \sigma_p$, i.e. $\alpha = 1$, one obtains

$$\sigma_{\min}/\sigma_i = 2b^{1/2}/(b + 1) \quad (5.22)$$

A special case of $\sigma_{\min} = \sigma_i$ occurs when $b = 1$, i.e., $\mu_n = \mu_p$

Equation 5.22 can also be written in another form

$$\sigma_{\min} = 2eb^{1/2}\mu_p n_i \quad (5.23)$$

In region IV, the electrical conductivity is controlled by the amount of dopant, i.e., $[\text{Ti}_{\text{Cr}}]$ and is expressed as

$$\sigma_{d,n} = e\mu_n n_d, \text{ where } n_d = [\text{Ti}_{\text{Cr}}] \quad (5.24)$$

Dividing Equation 5.23 by Equation 5.24

$$\frac{\sigma_{\min}}{\sigma_{d,n}} = \frac{2 \cdot e \cdot b^{1/2} \cdot \mu_p \cdot n_i}{e \cdot \mu_n \cdot n_d} = 2 \cdot b^{1/2} \cdot \frac{n_i}{n_d} \quad (5.25)$$

Thus

$$n_i = b^{1/2} \cdot (n_d/2) \cdot (\sigma_{\min}/\sigma_{d,n}) \quad (5.26)$$

When b is known, the intrinsic electron concentration n_i can be evaluated from the amount of dopant, i.e. $[Ti_{Cr}] = n_d$, and the ratio $(\sigma_{\min}/\sigma_{d,n})$. Since $K_i = n_i^2$, the equilibrium constant of the intrinsic ionization can also be calculated.

Assign a new parameter n_i' as

$$n_i' = (n_d/2) \cdot (\sigma_{\min}/\sigma_{d,n}) \quad (5.27)$$

then

$$n_i = b^{1/2} \cdot n_i' \quad (5.28)$$

In the case of $b = 1$, $n_i = n_i'$.

It has been suggested that in Cr_2O_3 the electron holes may have a higher mobility than the electrons (). Thus a situation of $b < 1$ is expected. In this study, an indication of $b \neq 1$, i.e., $\mu_n \neq \mu_p$ can be found from the following argument. By taking the derivative of Equation 5.3 with respect to $1/T$, one obtains

$$\frac{\partial \log \sigma_{\min}}{\partial (1/T)} = \frac{\partial \log b}{2 \partial (1/T)} + \frac{\partial \log \mu_p}{\partial (1/T)} + \frac{\partial \log n_i}{\partial (1/T)} \quad (5.29)$$

Assume $b = 1$ or $b \neq f(T)$, one gets

$$\frac{\partial \log \sigma_{\min}}{\partial (1/T)} = \frac{\partial \log \mu_p}{\partial (1/T)} + \frac{\partial \log n_i'}{\partial (1/T)} \quad (5.30)$$

Plotting $\log \sigma_{\min}$ and $\log n_i'$ vs. $1/T$ in Figure 5.10, a value of 0.57 eV is obtained from Equation 5.30 for the activation energies of both the electrons and electron holes. Apparently, this is not a reasonable value. Also it is far too large in comparison with the reported value of 0.17 eV of the activation energy of electron holes. It is therefore concluded that the mobility ratio b must vary with temperatures. In order to evaluate b , the electron and electron hole mobilities need to be determined individually. The electron mobility may be calculated from

the electrical conductivity in the region IV from Equation 5.24. The electrical conductivities have been measured on dense sample of composition 0.2 mole % at 10^{-15} Pa of P_{O_2} and the electron mobilities were calculated. Results are shown in Figure 5.11. the mobility of electron holes have been obtained from studies of the electrical conductivity on MgO-doped Cr_2O_3 . A complete discussion is presented in Chapter 6. In Table 3, the evaluated μ_n , μ_p and b are listed. It is found that $\mu_p > \mu_n$.

Table 3: Mobilities of electrons and electron holes

T (°C)	1300	1200	1100	1000
μ_n (cm ² /V-sec)	0.040	0.030	0.022	0.015
μ_p (cm ² /V-sec)	0.083	0.076	0.069	0.062
b	0.48	0.39	0.31	0.24

Based on Equations 5.26 and 5.6, n_i and K_i were calculated. The results are listed in Table 4

Table 4: Table of calculated intrinsic electron concentration n_i and the correspondence equilibrium K_i

T (°C)	1300	1200	1100	1000
n_i (#/cm ³)	3.47×10^{18}	1.70×10^{18}	7.41×10^{17}	2.88×10^{17}
K_i	1.20×10^{37}	2.88×10^{36}	5.50×10^{35}	8.32×10^{34}

5.2.4 Construction of the Defect Concentration vs Oxygen Partial Pressure Diagram

Since $b \neq 1$ and $\sigma_i \neq \sigma_{\min}$, it is necessary to determine the oxygen partial pressure $P_{O_2}^i$ at which the electron concentration is equal to n_i before one can

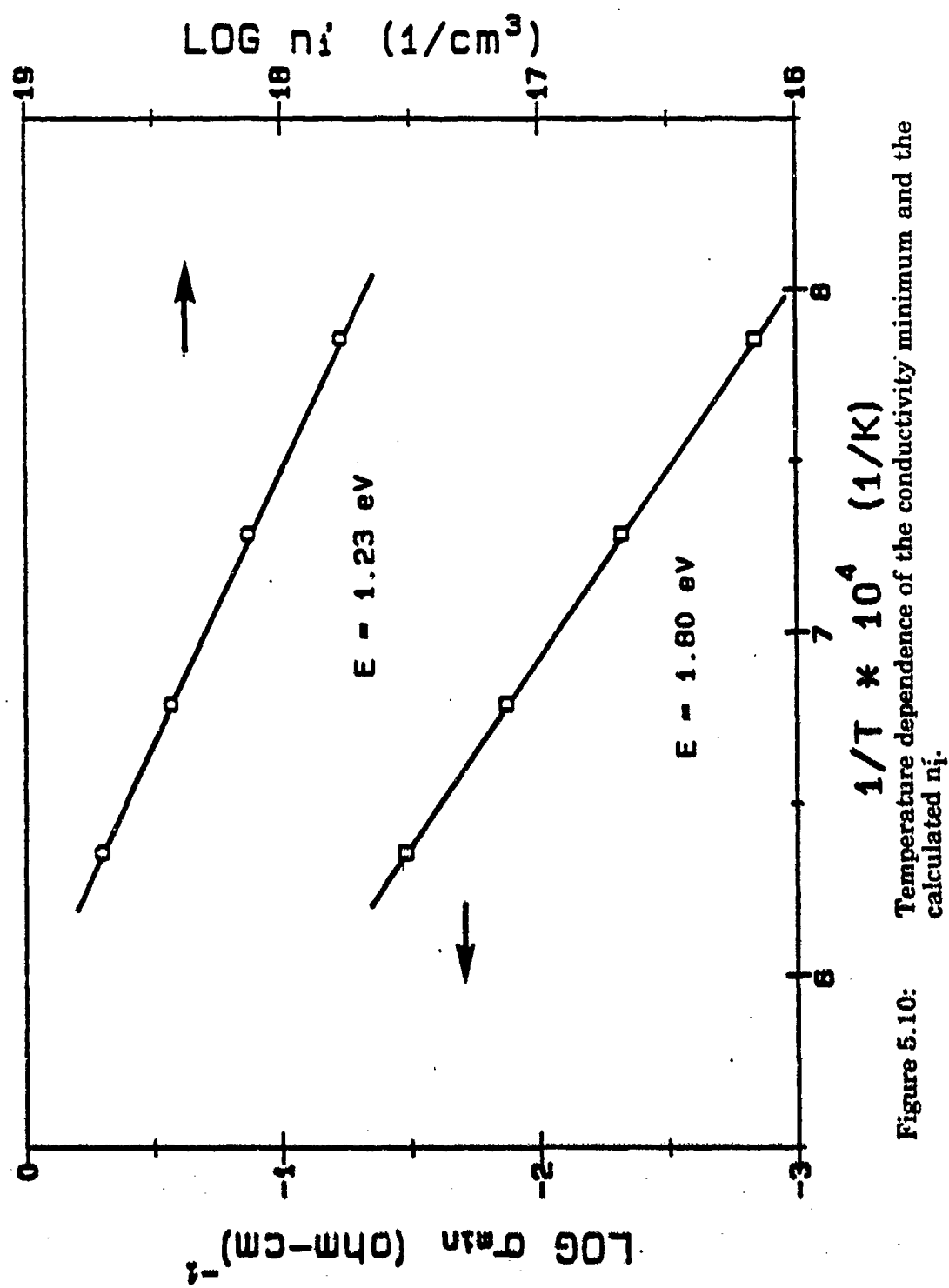


Figure 5.10: Temperature dependence of the conductivity minimum and the calculated n_i .

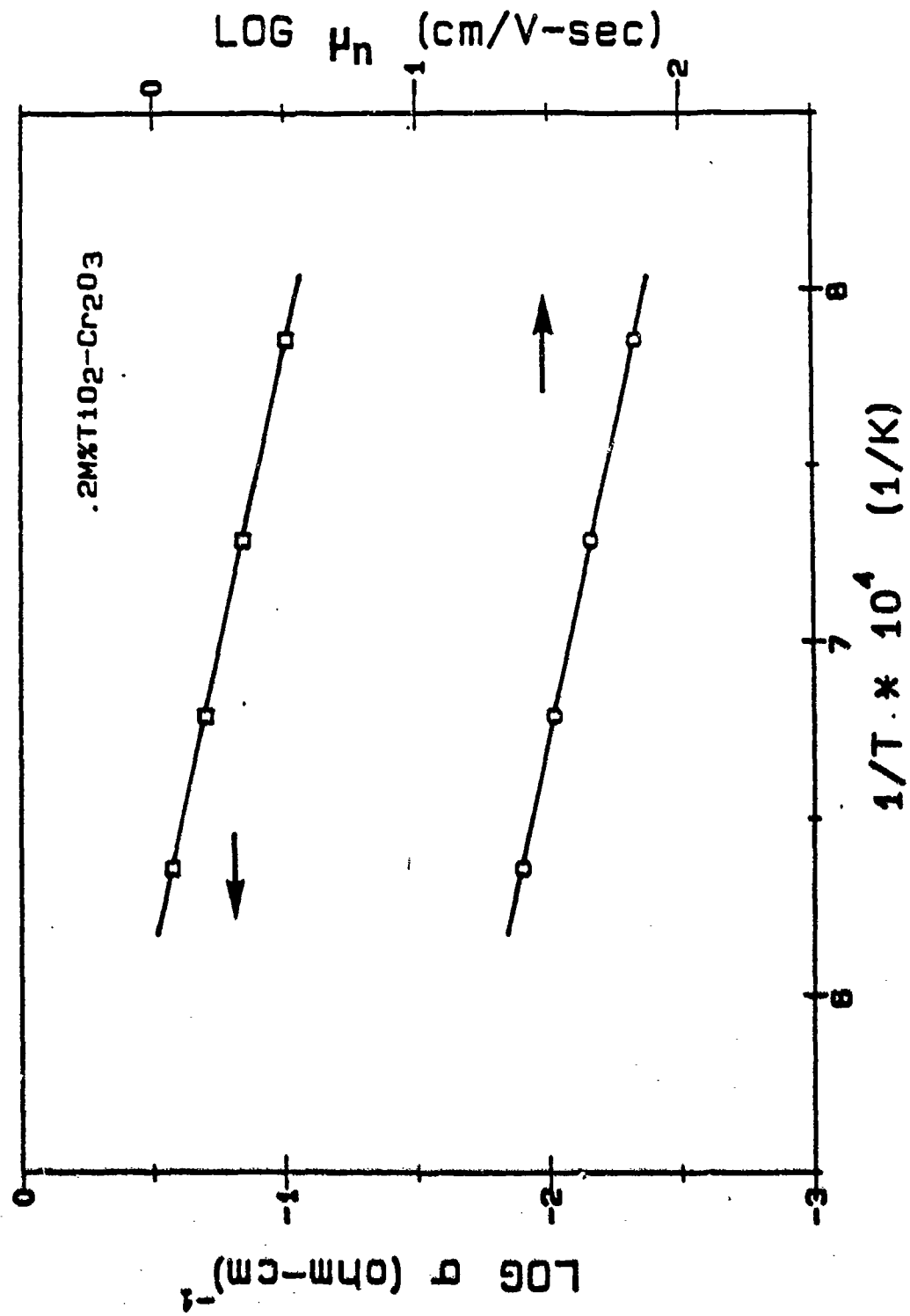


Figure 5.11: Temperature dependence of the electrical conductivity and the calculated mobilities.

construct the Kröger-Vink diagram. Based on Equation 5.22 and the symmetric characteristics of the diagram in the vicinity of n_i , the value of $P_{O_2}^i$ can be obtained from adjustment of $P_{O_2}^d$. With knowledge of the points $(n_i, P_{O_2}^i)$ and $(n_d, P_{O_2}^d)$, and the diagram in Figure 5.14 the construction of the Kröger-Vink diagram is straightforward. The constructed diagrams are presented in Figures 5.12 to 5.15. Based on these diagrams, the equilibrium constant $K_{V_{Cr}''}$ associated with the formation of the chromium vacancies can then be calculated from Equation 5.5. an expression of

$$K_{V_{Cr}''} = 3.63 \times 10^{168} \exp(-5.88 \text{ eV}/kT) \quad (5.31)$$

is obtained. And from K_i and $K_{V_{Cr}''}$, the point defect structure of pure Cr_2O_3 in the high P_{O_2} region is then obtained. The calculated defect concentrations of pure Cr_2O_3 are plotted as functions of P_{O_2} in Figure 5.16. Further discussion will be presented in Chapter 7.

5.3 Summary

The following conclusions are obtained from the studies of the electrical conductivity and Seebeck coefficient of TiO_2 -doped Cr_2O_3 .

- (1) It is found that doping with Ti in Cr_2O_3 increases the electron conductivity. A change of conduction mechanism from P-type to N-type behavior is observed in the high P_{O_2} region.
- (2) The results also indicate that in the low P_{O_2} region the solubility limit of TiO_2 in Cr_2O_3 changes with oxygen partial pressure.
- (3) A model is proposed to explain the electrical properties of this system. Combining experimental results with the model, the equilibrium constants, K_i and $K_{V_{Cr}''}$, were obtained and the defect structure of pure Cr_2O_3 in the high P_{O_2} region was determined.

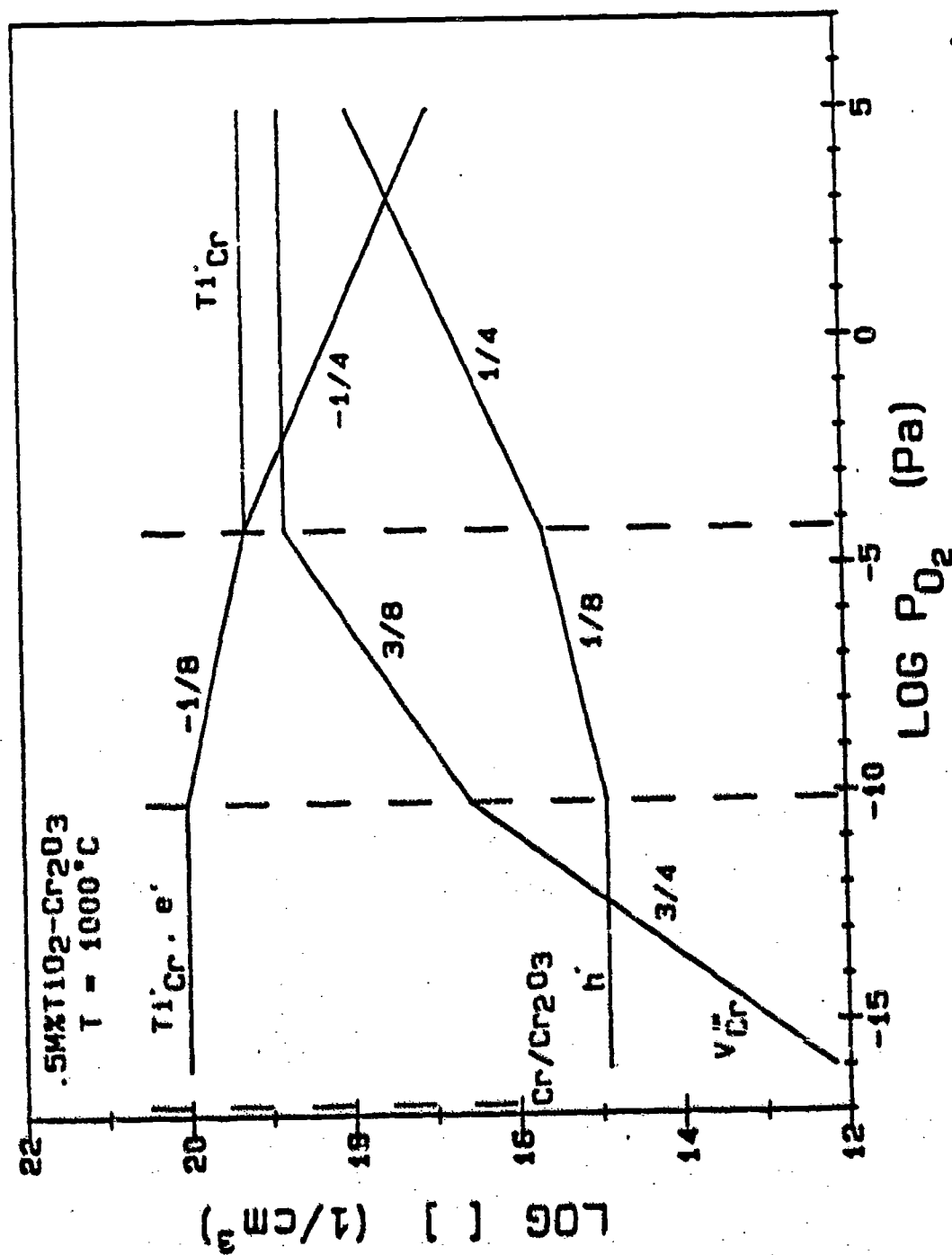


Figure 5.12: Defect concentrations vs. oxygen partial pressure diagram of TiO_2 -doped Cr_2O_3 at 1000°C

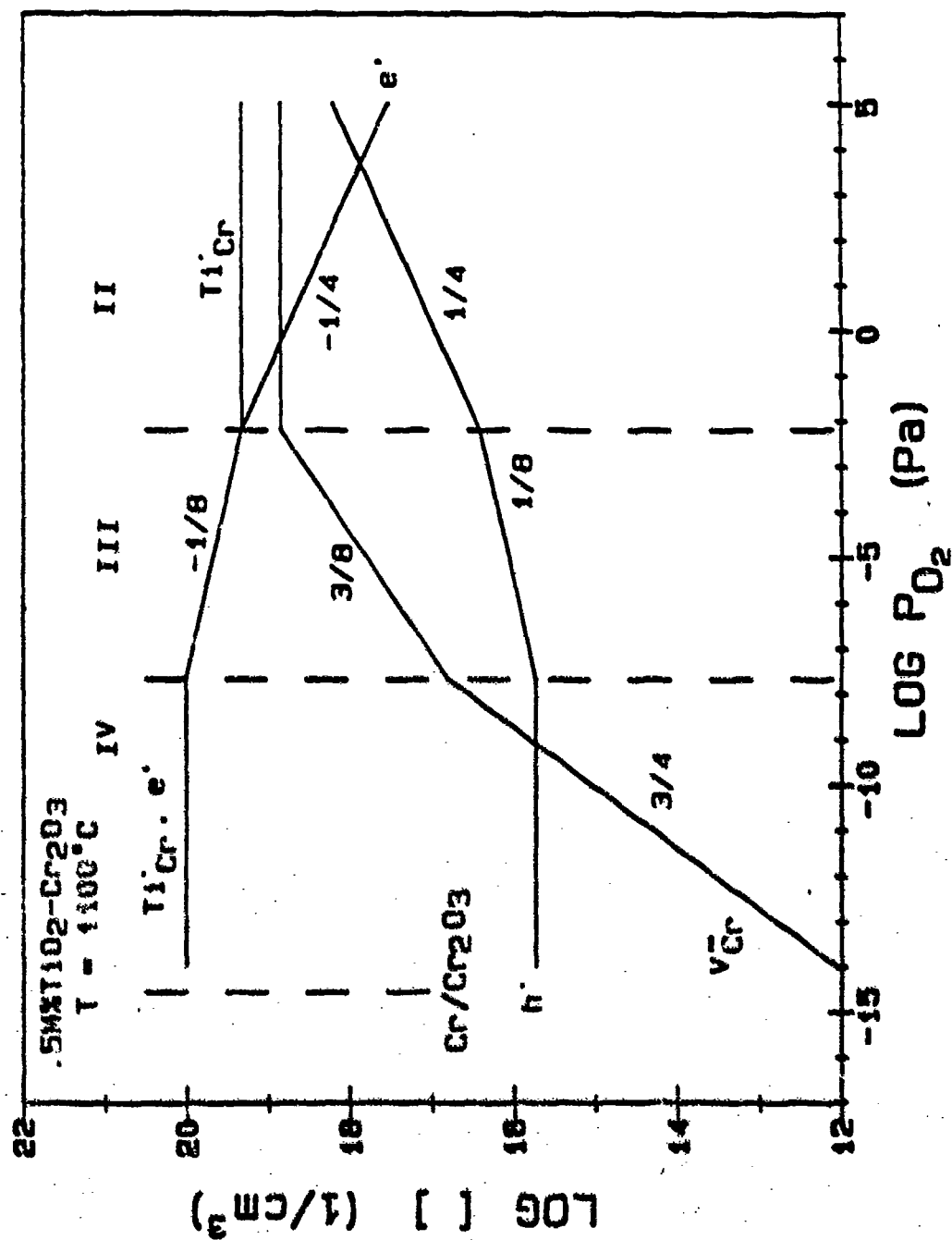


Figure 5.13: Defect concentrations vs. oxygen partial pressure diagram of TiO₂-doped Cr₂O₃ at 1100°C.

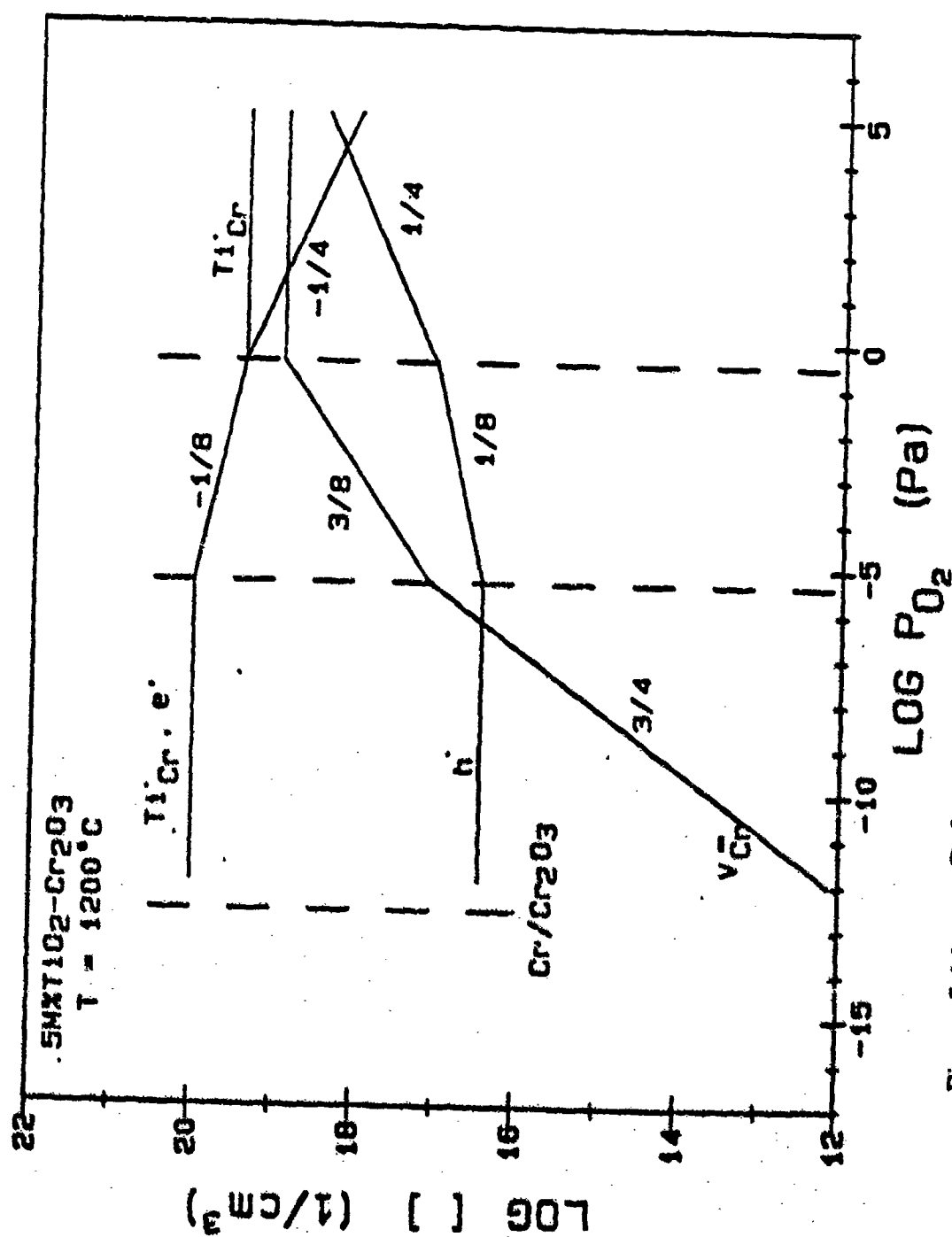


Figure 5.14: Defect concentrations vs. oxygen partial pressure diagram of TiO₂-doped Cr₂O₃ at 1200°C.

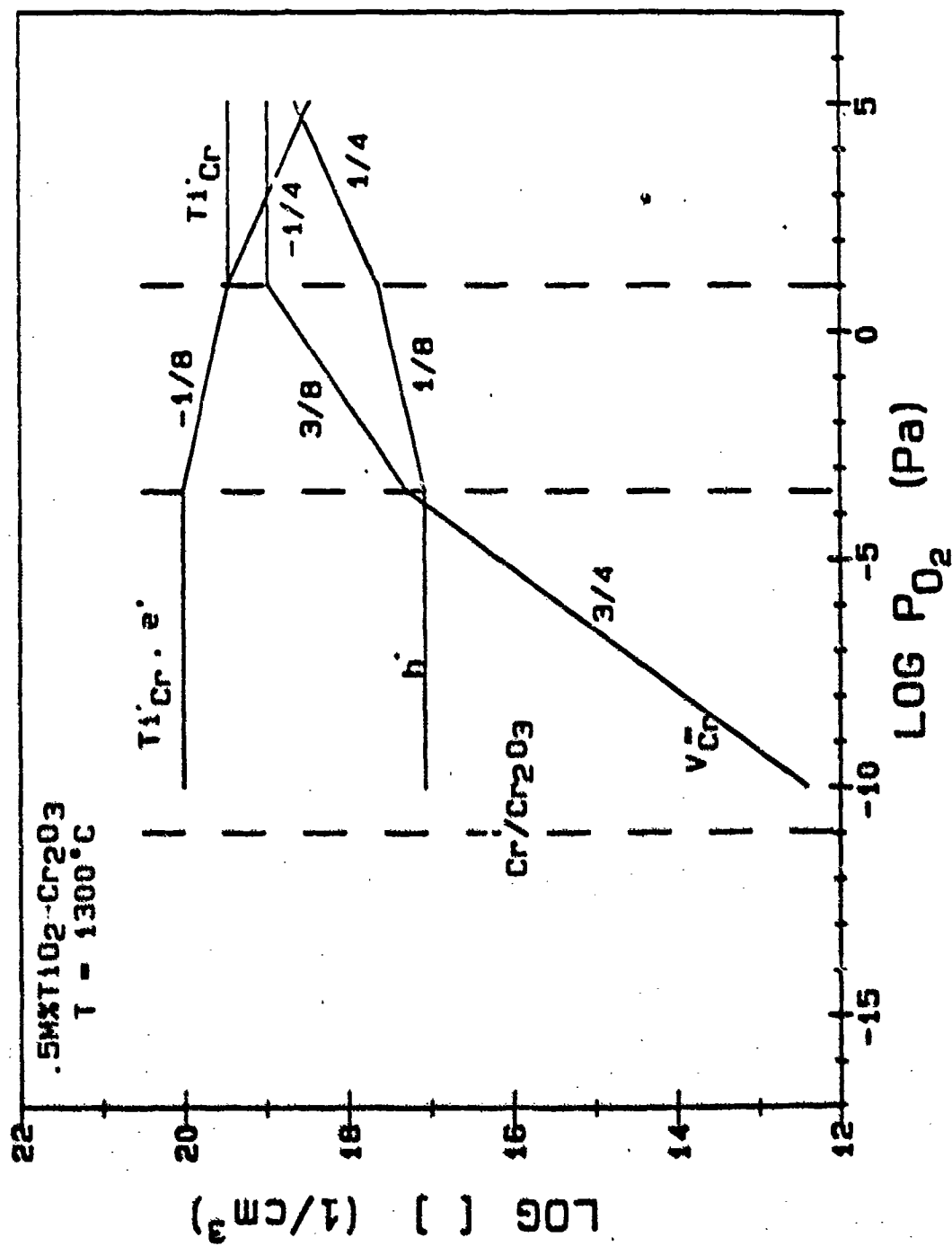


Figure 5.15: Defect concentrations vs. oxygen partial pressure diagram of TiO₂-doped Cr₂O₃ at 1300°C.

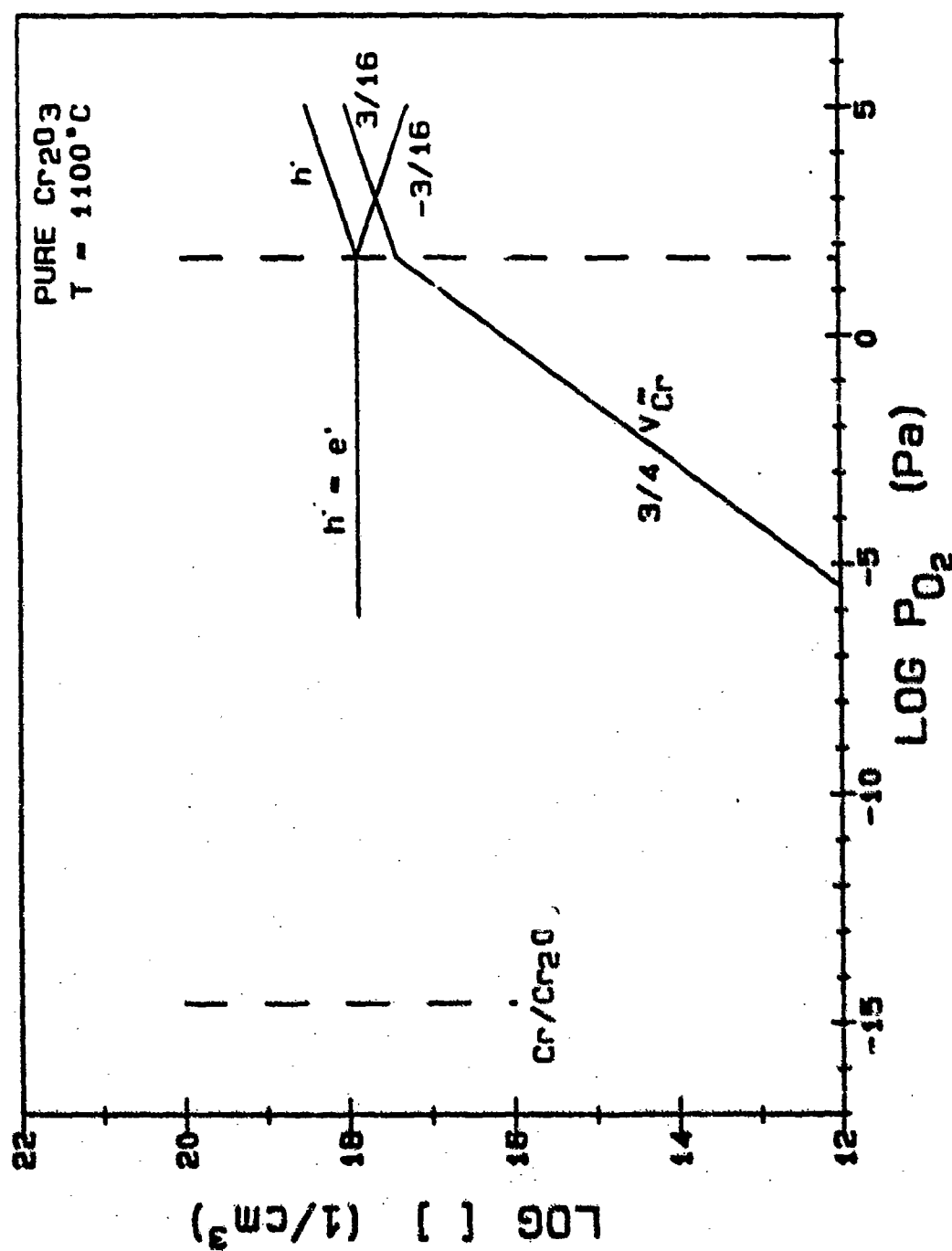


Figure 5.16: Point defect structure of pure Cr_2O_3 in the high oxygen partial pressure at 1100°C .

Chapter 6

ELECTRICAL CONDUCTIVITY AND SEEBECK COEFFICIENT OF MGO-DOPED Cr_2O_3

In the chapter the results of the electrical conductivity and Seebeck coefficient measurements of MgO-doped Cr_2O_3 are presented. It was found that doping Cr_2O_3 with Mg (a lower valent cation) has an effect opposite to Ti (a higher valent cation) doping. In general, the incorporation of MgO into the structure of the Cr_2O_3 will increase the electron hole conductivity. Also since the solubility limit of MgO in Cr_2O_3 changes with oxygen partial pressure, the presence of a second phase MgCr_2O_4 has a significant influence in altering the defect structure of Cr_2O_3 . A model for the defect structure of MgO-doped Cr_2O_3 is proposed to explain these phenomena. Based on this model and the experimental results the majority defects of Cr_2O_3 in the low P_{O_2} region were determined. In the following sections, the results, analyses and discussions are presented in detail.

6.1 Results

6.1.1 Solubility limit of MgO in Cr_2O_3

The solubility limit of MgO in Cr_2O_3 was studied by lattice parameter measurements using the X-ray Powder Diffraction method. Cr_2O_3 samples with up to 2.5 mol% of MgO were sintered at 1300°C for 24 hours at 1 and 10^{-15} atm P_{O_2} , and air quenched to room temperature. The lattice parameters of these samples were calculated from the X-ray power diffraction pattern. The results are plotted as a function of the MgO content and the sintering atmosphere in Figure 6.1. It appears that at dopant levels above 1 mole %, the measured lattice

parameters of samples sintered at different P_{O_2} 's become different. This observation indicates that the solubility limit of MgO in Cr_2O_3 may be dependent upon oxygen partial pressure. However, it has not been possible to obtain definite values for the solubility due to the large deviation of the data.

Also, further information has been obtained from the X-ray diffraction pattern. Figure 6.2 shows the diffraction patterns of 0.5 mole % MgO- Cr_2O_3 sintered at 1 and 10^{-15} atm P_{O_2} . It appears that a second phase of $MgCr_2O_4$ exist for samples prepared at low P_{O_2} while it was not found on the pattern of the high P_{O_2} sintered sample. From these results, it is concluded that the solubility limit of MgO in Cr_2O_3 decreases with decreasing P_{O_2} .

6.1.2 Electrical Conductivity and Seebeck Coefficient

The experimental results of the electrical conductivity and Seebeck coefficient measurements are plotted as functions of oxygen partial pressure and MgO content in Figures 6.3 and 6.4, respectively. The general characteristics of these curves are described in the following.

(1) Oxygen partial pressure dependence

Both the conductivity σ and the Seebeck coefficient Q remain relatively unchanged with little P_{O_2} dependence in the high P_{O_2} region. In the intermediate P_{O_2} region, σ decreases with decreasing P_{O_2} while Q increases slightly. In the low P_{O_2} region, there is an indication that σ may vary with P_{O_2} in a different manner. Also, in the corresponding Seebeck coefficient, a maximum, Q_{max} , appears at a oxygen partial pressure $P_{O_2}^m$. When P_{O_2} is decreased below $P_{O_2}^m$, the value of Seebeck coefficient drops relatively fast with decreasing P_{O_2} . However, negative values of Q have not been observed. This may be because the lowest P_{O_2}

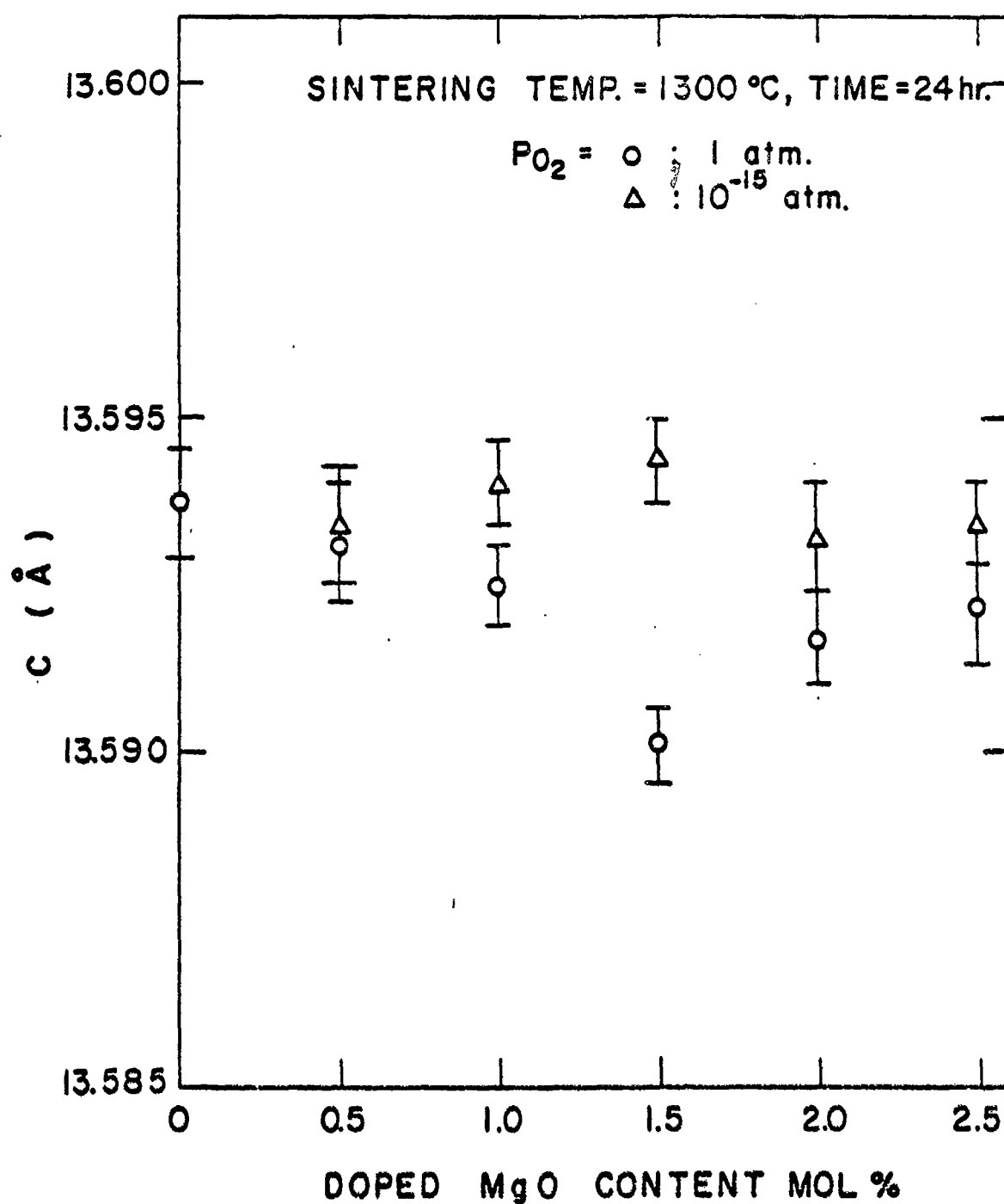
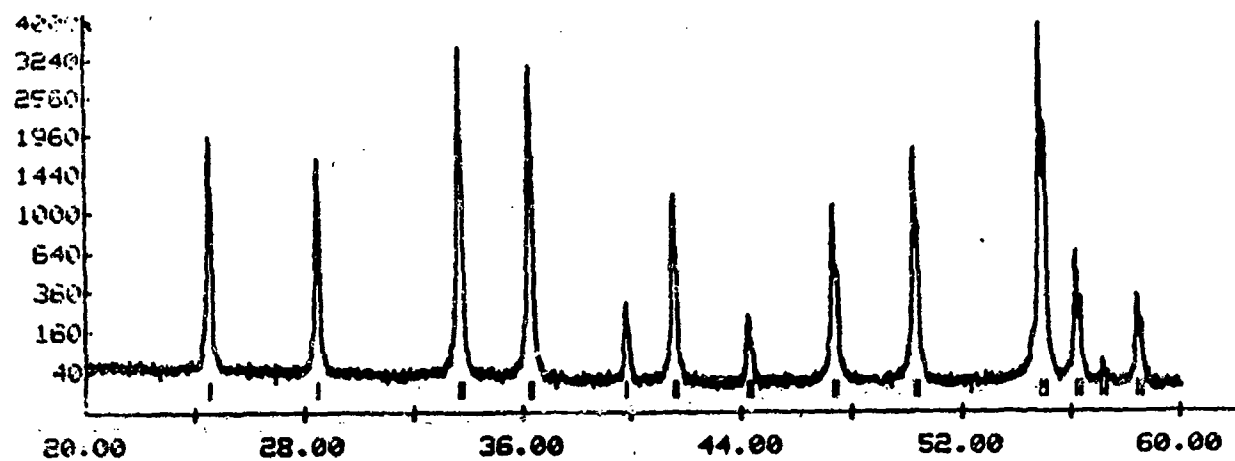
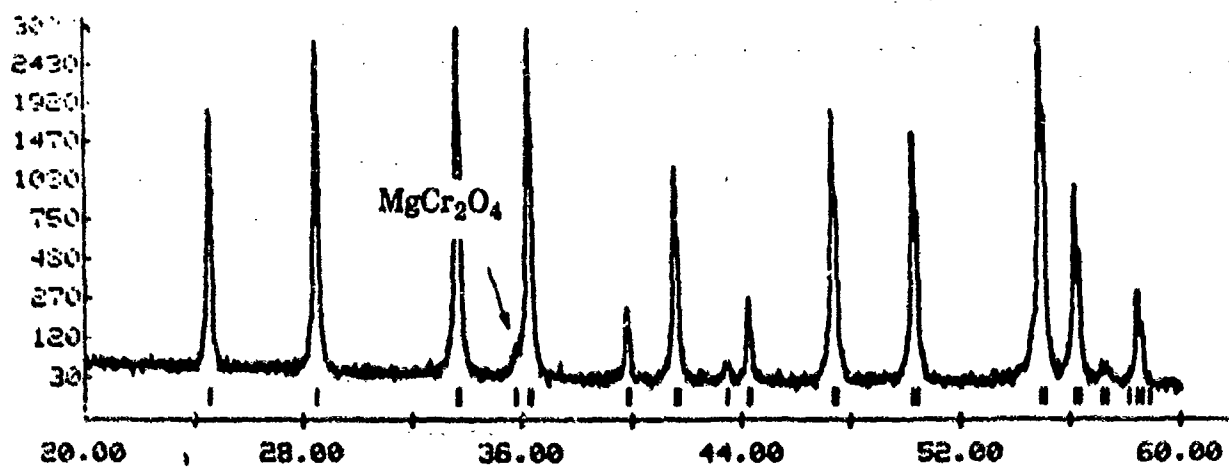


Figure 6.1: Lattice parameters of MgO-doped Cr_2O_3 , plotted as functions of dopant content and sintering atmosphere.



(a)



(b)

Figure 6.2: The X-ray powder diffraction patterns of MgO-doped Cr_2O_3 sintered at (a) 1 atm. (b) 10^{-15} PO_2

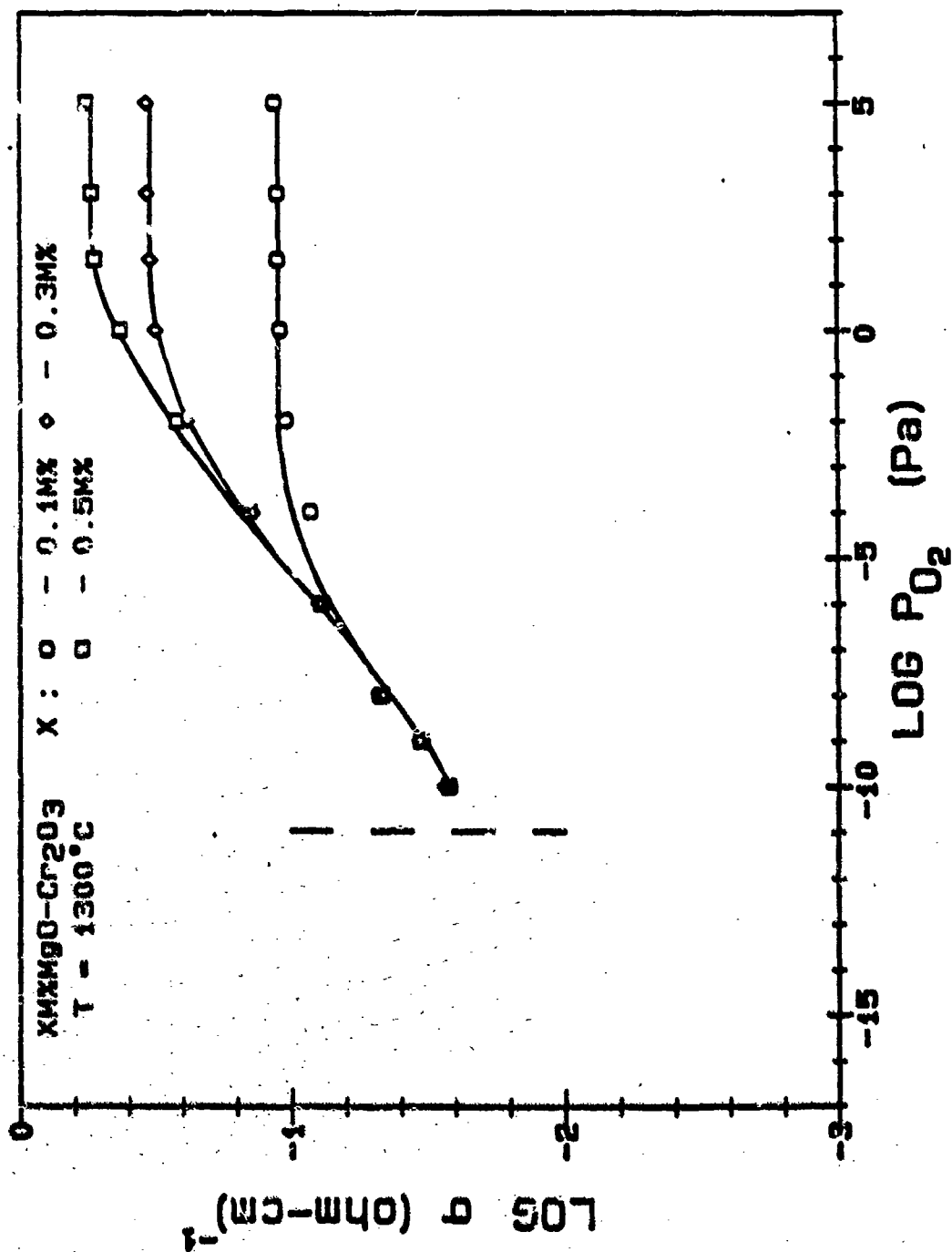


Figure 6.3: Oxygen partial pressure dependence of the electrical conductivity of MgO-doped Cr_2O_3 at 1300°C

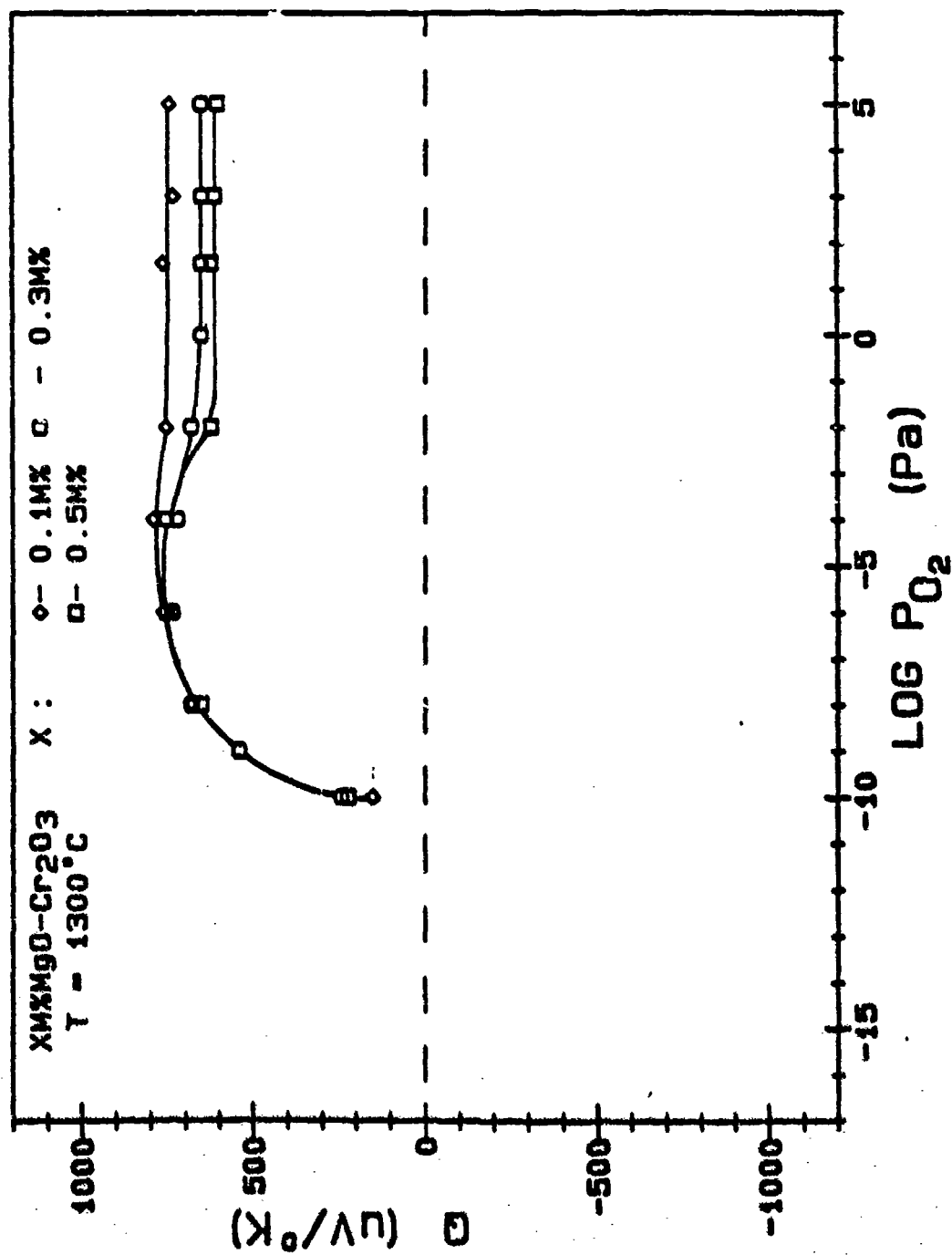


Figure 6.4: Oxygen partial pressure dependence of the Seebeck coefficient of MgO-doped Cr_2O_3 at $1300^\circ C$

that the experimental method can be achieved is still not low enough to see a P-type to N-type transition.

(2) **Composition Dependence**

When the composition dependence is examined, a very nice correspondence to the solubility results is observed. (i) In the high P_{O_2} region, both conductivities and Seebeck coefficients indicate that the dopant levels used are below the solubility limit. (ii) When P_{O_2} is decreased, the composition dependence diminished below a certain oxygen partial pressure $P_{O_2}^d$. This fact indicates that at $P_{O_2} < P_{O_2}^d$ the dopant level is higher than the solubility limit. Since there is no reason for the dopant content to change during the experiment, apparently, the solubility limit must decrease as P_{O_2} is decreased.

(3) **Temperature dependence**

The temperature dependence of the electrical conductivity and Seebeck coefficient are shown in Figures 6.5 and 6.6, respectively. It appears that the activation energy of the electrical conductivity is very small. Also it is found that as temperature is increased, all the characteristic points, i.e., $P_{O_2}^d$ and $P_{O_2}^m$, shift to lower P_{O_2} .

6.2 **Analyses and Discussions**

6.2.1 **Defect Structure of MgO-doped Cr_2O_3**

Since the incorporation of Mg^{2+} ions into Cr_2O_3 will generate negative charges, defects with positive charges are created in order to maintain the electronic neutrality. The possible defect reactions will then involve either h^{\cdot} or $Cr_i^{\cdot\cdot}$ or both. Accordingly, the following defect equations need to be considered. For the case of h^{\cdot} , the relations

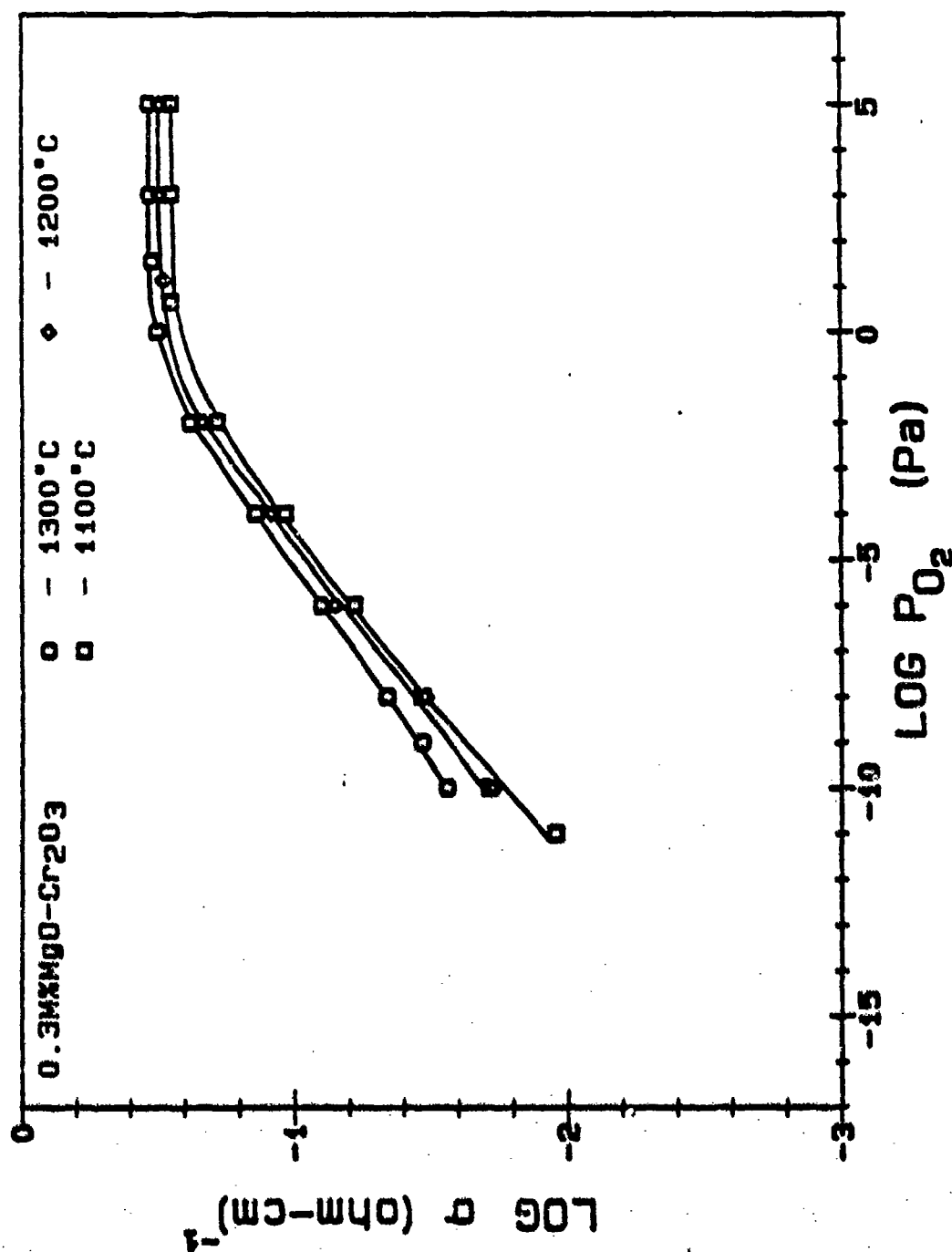


Figure 6.5: Oxygen partial pressure dependence of the electrical conductivity of 0.3mole% MgO-doped Cr₂O₃ at different temperatures

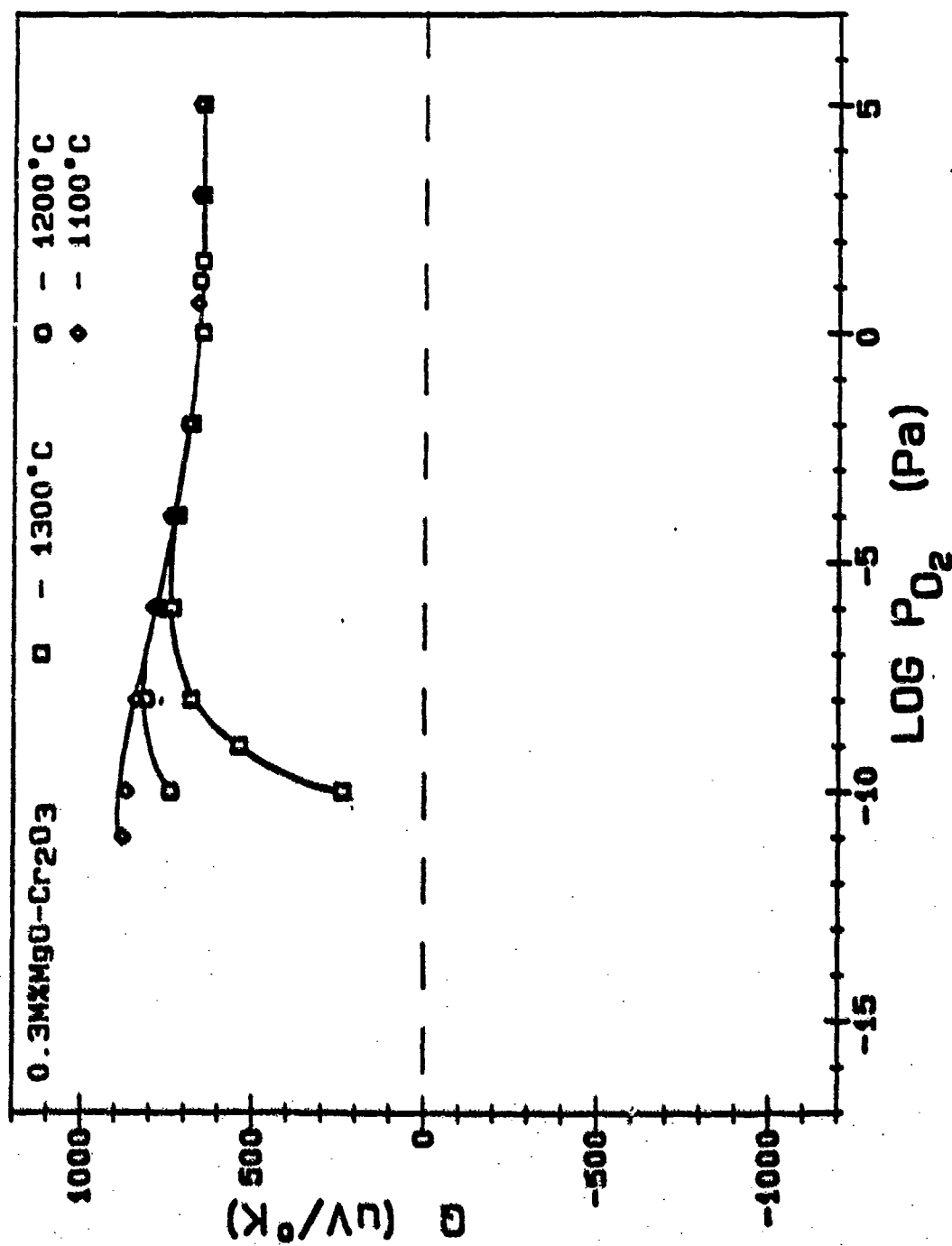
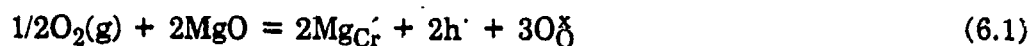


Figure 6.6: Oxygen partial pressure dependence of the Seebeck coefficient of 0.3mole% MgO-doped Cr₂O₃ at different temperatures

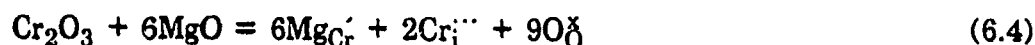


$$K_{\text{MgCr}2} = [\text{Mg}_{\text{Cr}}']^2 \cdot [\text{h}^\cdot]^2 \cdot P_{\text{O}_2}^{-1/2} \quad (6.2)$$

will give the following defect concentrations that are oxygen partial pressure dependent,

$$[\text{h}^\cdot] = [\text{Mg}_{\text{Cr}}'] = K_{\text{MgCr}2}^{1/8} \cdot P_{\text{O}_2}^{-1/8} \quad (6.3)$$

In the case of $\text{Cr}_i^{''}$, the equations



$$K_{\text{MgCr}1} = [\text{Mg}_{\text{Cr}}']^6 \cdot [\text{Cr}_i^{''}]^2 \quad (6.5)$$

show that the following defect concentrations are P_{O_2} independent.

$$[\text{Cr}_i^{''}] = 1/3[\text{Mg}_{\text{Cr}}'] = 3^{-3/4} \cdot K_{\text{MgCr}1}^{1/8} \quad (6.6)$$

When both cases are considered, the electroneutrality condition is

$$[\text{Mg}_{\text{Cr}}'] + [\text{e}^\cdot] = [\text{h}^\cdot] + 3[\text{Cr}_i^{''}] \quad (6.7)$$

The relationships among different defect concentrations and the oxygen partial pressure can be obtained by applying the same technique discussed in Chapter 5 to all the related defect equations. In Figure 6.7, the theoretical prediction of the defect structure of MgO-doped Cr_2O_3 is represented by a Kröger-Vink diagram. According to this diagram, four regions can be distinguished. In region I, the denoted unsaturated region, represents the situation that the dopant level is below the solubility limit. In this case, the concentration of electron holes is determined by the amount of dopant, i.e., $[\text{h}^\cdot] = [\text{Mg}_{\text{Cr}}'] = \text{constant}$. Since the solubility limit of MgO in Cr_2O_3 may decrease with decreasing P_{O_2} , in region II a second phase will be present, and the Mg concentration in Cr_2O_3 will be saturated. As a results, a $P_{\text{O}_2}^{1/8}$ dependence of the defect concentrations based on Equation 6.3 is observed. In region III, where the $\text{Cr}_i^{''}$ is dominant, Equations 6.4 to 6.6 are applied. It is found from the variation of the concentration of the

electronic defects that a situation of $[h'] = [e']$ exists in this region. Thus, a conductivity minimum is expected in this region. Region IV represents the intrinsic behavior of pure Cr_2O_3 where chromium interstitials (Cr_i^{2+}) and electrons (e') are the majority defects.

6.2.2 Calculation of Electron Hole Mobility

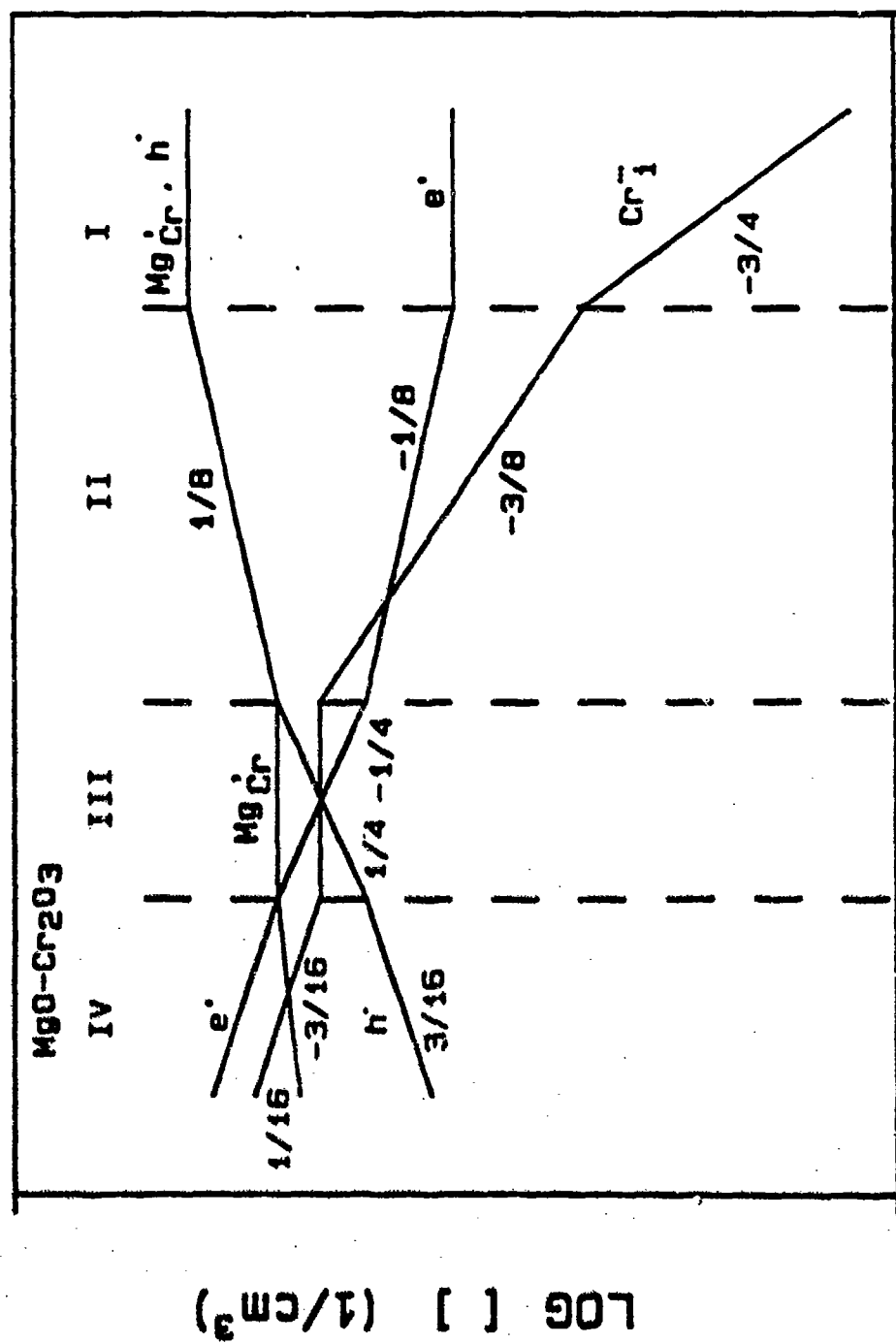
When the defect structure model in Figure 6.7 is compared with the electrical conductivity results in Figures 6.3 and 6.5 rather good agreement is found. Although in the low P_{O_2} region, the expected conductivity minimum has not been determined due to the experimental limitation of controlling a low P_{O_2} , the model does predict the variation of the electrical conductivity with the oxygen partial pressure.

Based on this model, it is then possible to determine the mobility of electron holes by measuring the electrical conductivity in the "unsaturated" region. The electrical conductivity measurement has been performed on dense sample. Since high density samples can only be sintered at low P_{O_2} , and high solubility of MgO in Cr_2O_3 exists at high P_{O_2} , a special procedure for sample preparation was used. Samples were first sintered at 1600°C in CO/CO_2 atmosphere of 10^{-11} atm P_{O_2} for two hours, and then annealed at the same temperature in 1 atm P_{O_2} for 6 days.

The electrical conductivity and the calculated electron hole mobility are plotted as a function of temperature in Figure 6.8. An expression for the mobility by

$$\mu_p = \mu_{op} \cdot \exp(-\Delta E/kT) \quad (6.8)$$

with $\mu_p = 0.29 \text{ cm}^2/\text{V-sec}$ and $\Delta E = 0.17 \text{ eV}$ is obtained.



LOG PO_2

Figure 6.7: A model for the defect structure of MgO-doped Cr_2O_3

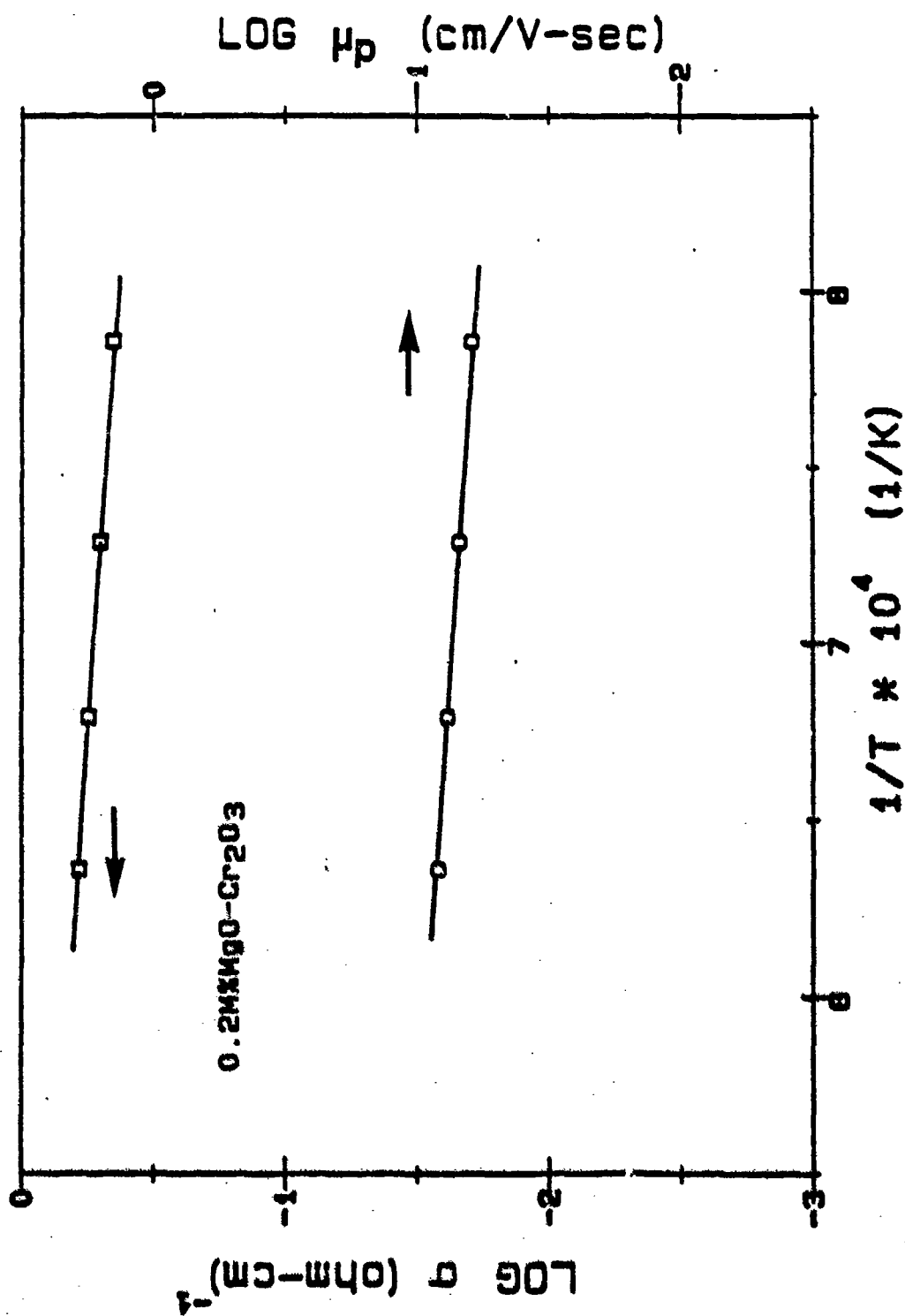


Figure 6.8: Temperature dependence of the electron hole mobility, calculated from the electrical conductivity of 0.2mole%MgO-doped Cr₂O₃ measured at 1 atm PO₂

6.2.3 Construction of the Defect Concentration vs. Oxygen Pressure Diagram

It has been pointed out in Chapter 5 that based on the defect structure model and the experimental results, one may be able to construct a [defect] vs P_{O_2} diagram. In the process of the construction of this diagram, at least two of the positions, the boundaries between the different regions and the position of $n=p=n_i$, are needed.

Since in the high P_{O_2} "unsaturated" region, the concentration of electron holes is determined by the amount of dopant, i.e., $p_d = [h'] = [Mg_{Cr}']$, the boundary point $(p_d, P_{O_2}^d)$ is obtained. However, due to the lack of the σ_{min} in the results, the determination of the other point is not as straightforward. Two approaches have been used. First by estimating the P_{O_2} at the boundary between regions II and III from the experimental results, the line of $[h']$ in region II can be determined since it has a slope of $1/8$ and a starting point $(p_d, P_{O_2}^d)$. Second, the results of Seebeck coefficient measurement have also been utilized. Since there has been a strong indication that the conduction mechanism in Cr_2O_3 is by small polaron conduction, the different parameters N_v , N_c , A_n , A_p , in the equation of Seebeck coefficient can be calculated. Also, since the intrinsic electron concentration n_i has been evaluated, the Seebeck coefficient Q_i at $n=p=n_i$ can then be calculated, and the corresponding oxygen partial pressure $P_{O_2}^i$ can be estimated.

Based on these analyses, the [defect] vs P_{O_2} diagrams at 1100° , 1200° , and $1300^\circ C$ are constructed and plotted in Figures 6.9 to 6.11. It has been shown in Chapter 5 that the equilibrium constant, K_{Cr} , associated with the formation of chromium interstitials can be calculated from

$$K_{Cr_i'''} = [Cr_i''']^2 \cdot [e']^6 \cdot P_{O_2}^{3/16} \quad (6.9)$$

Based on these [defect] - P_{O_2} diagrams, $K_{Cr_i'''} has been calculated for all three temperatures, and can be expressed as$

$$K_{Cr_i'''} = 5.07 \times 10^{191} \cdot \exp(-20.48 \text{ ev/kT}) \quad (6.10)$$

Combined with the equilibrium constant $K_{V_{Cr}''}$ obtained in Chapter 5, the equilibrium constant for the formation of Frenkel defect, K_F , is obtained as

$$K_F = 1.17 \times 10^{42} \cdot \exp(-4.78 \text{ ev/kT}) \quad (6.11)$$

With these constants, $K_{Cr_i'''}$, K_i , K_F , the defect structure of Cr_2O_3 at low P_{O_2} region can then be determined. An example of the construction of [defect] - P_{O_2} diagram for pure Cr_2O_3 at low P_{O_2} region is shown in Figure 6.12. Further discussions will be presented in Chapter 7.

6.3 Summary

The following conclusions have been obtained from the study of the electrical conductivity and Seebeck coefficient of MgO-doped Cr_2O_3 :

- (1) Doping with MgO in Cr_2O_3 increases the electron hole conductivity. P-type behavior has been found for all the temperatures and P_{O_2} 's studied.
- (2) A maximum of the Seebeck coefficient has been found at very low P_{O_2} 's which indicates a possibility of a change in conduction mechanism from P-type to N-type.
- (3) The solubility limit of MgO in Cr_2O_3 has been found to decrease with decreasing P_{O_2} . This property has a strong effect on altering the defect structure of Cr_2O_3 .

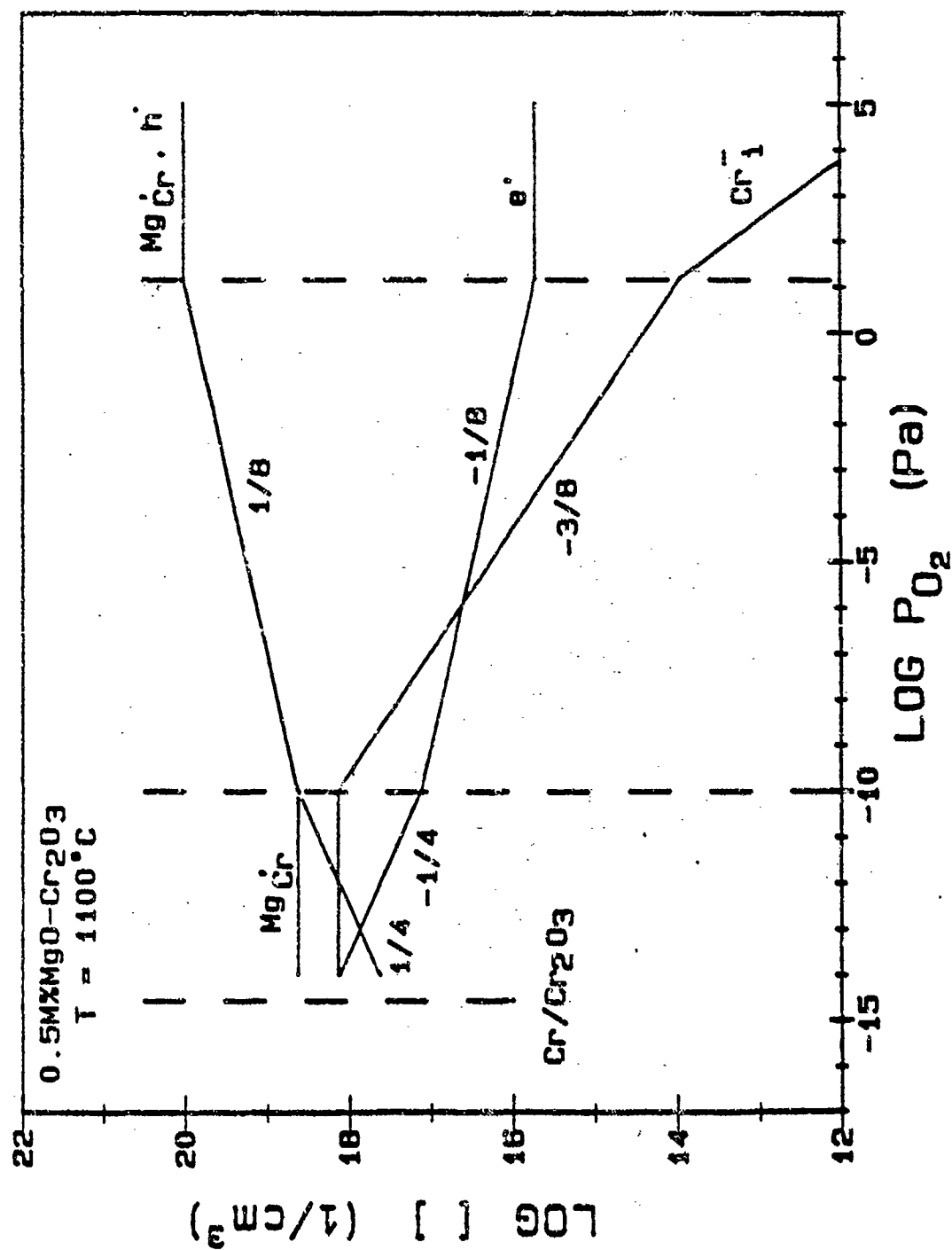


Figure 6.9: Defect concentration vs. oxygen pressure diagram for MgO-doped Cr₂O₃ at 1100°C

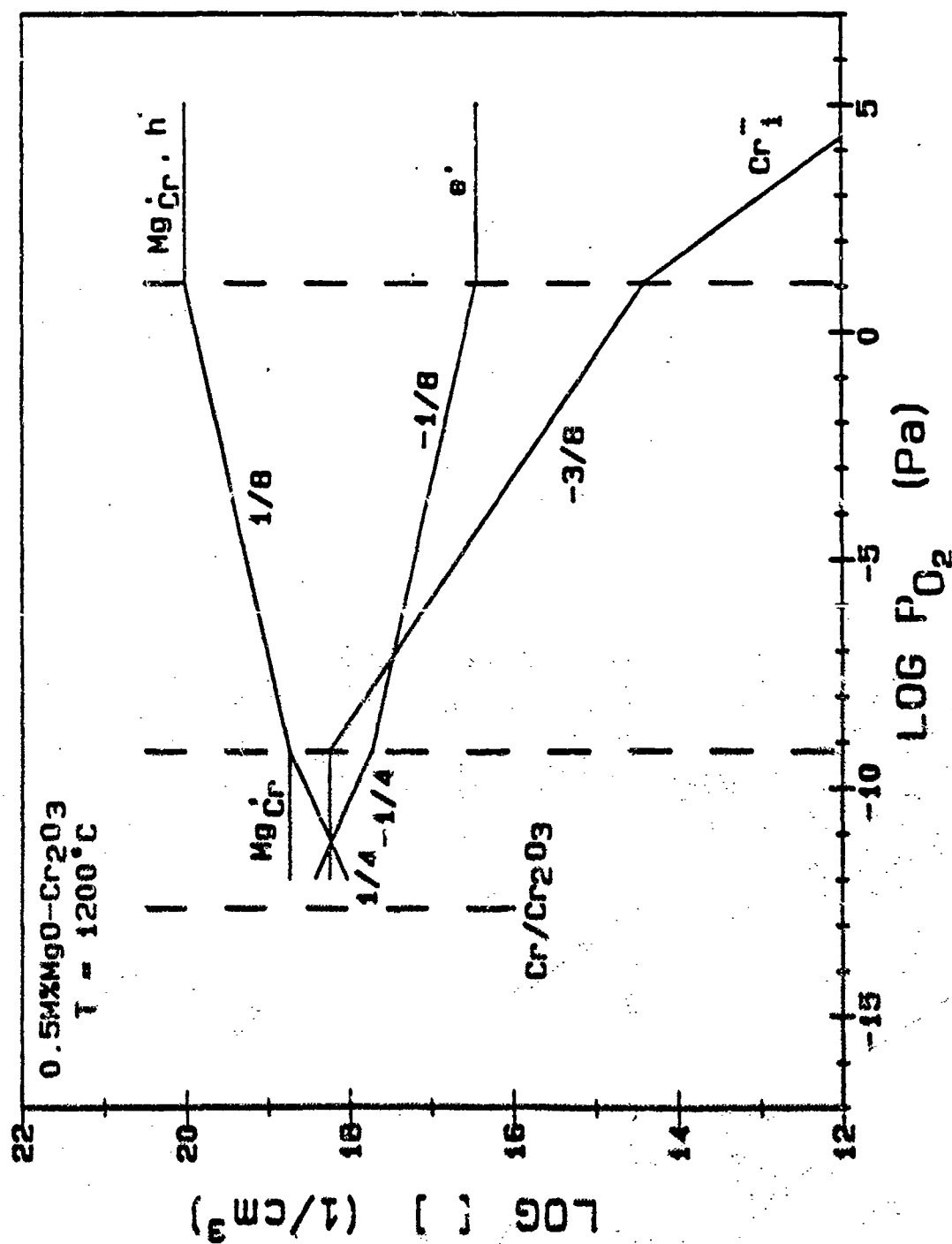


Figure 6.10: Defect concentrations vs. oxygen pressure diagram for MgO-doped Cr₂O₃ at 1200°C

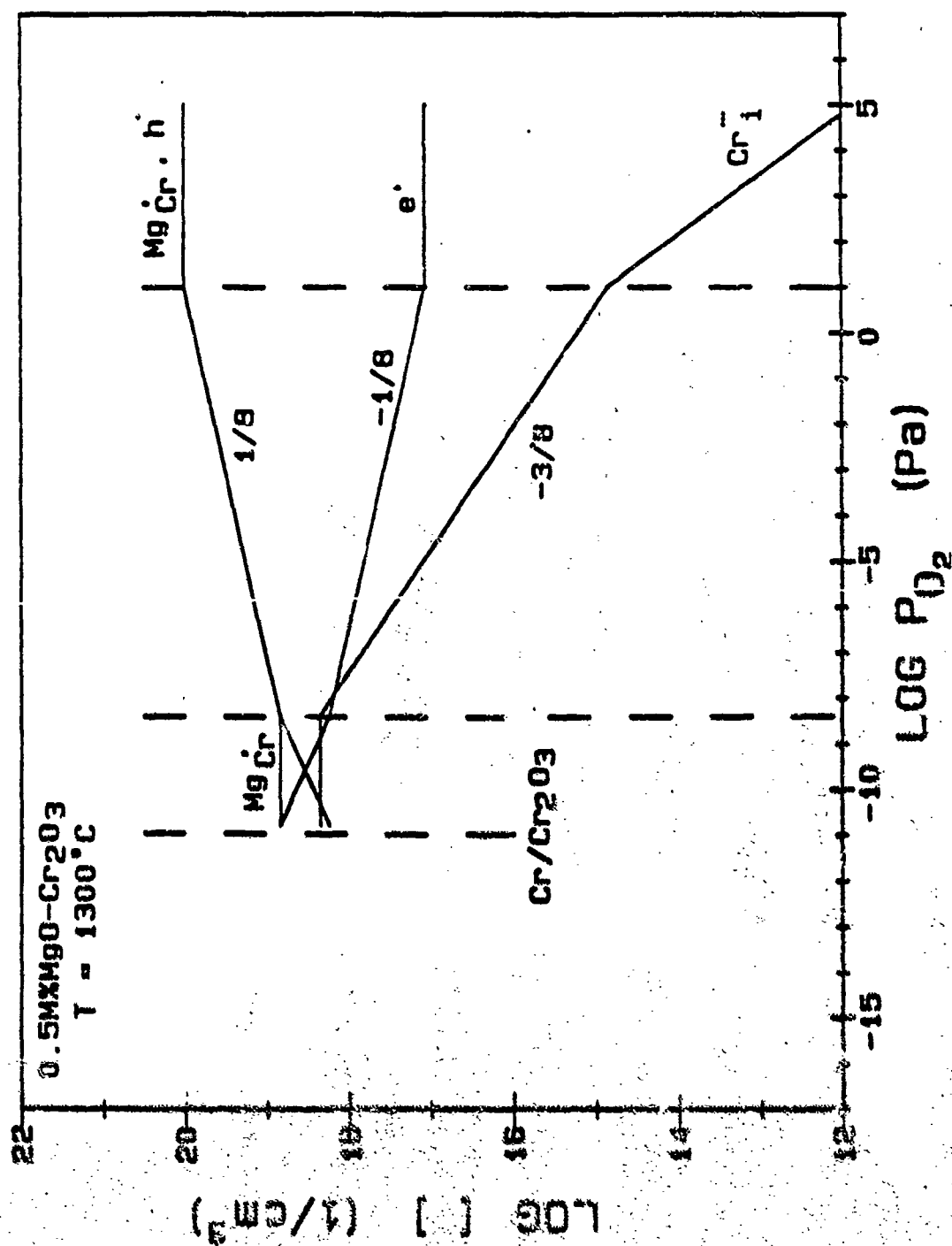


Figure 6.11: Defect concentrations vs oxygen pressure diagram for MgO-doped Cr₂O₃ at 1300°C

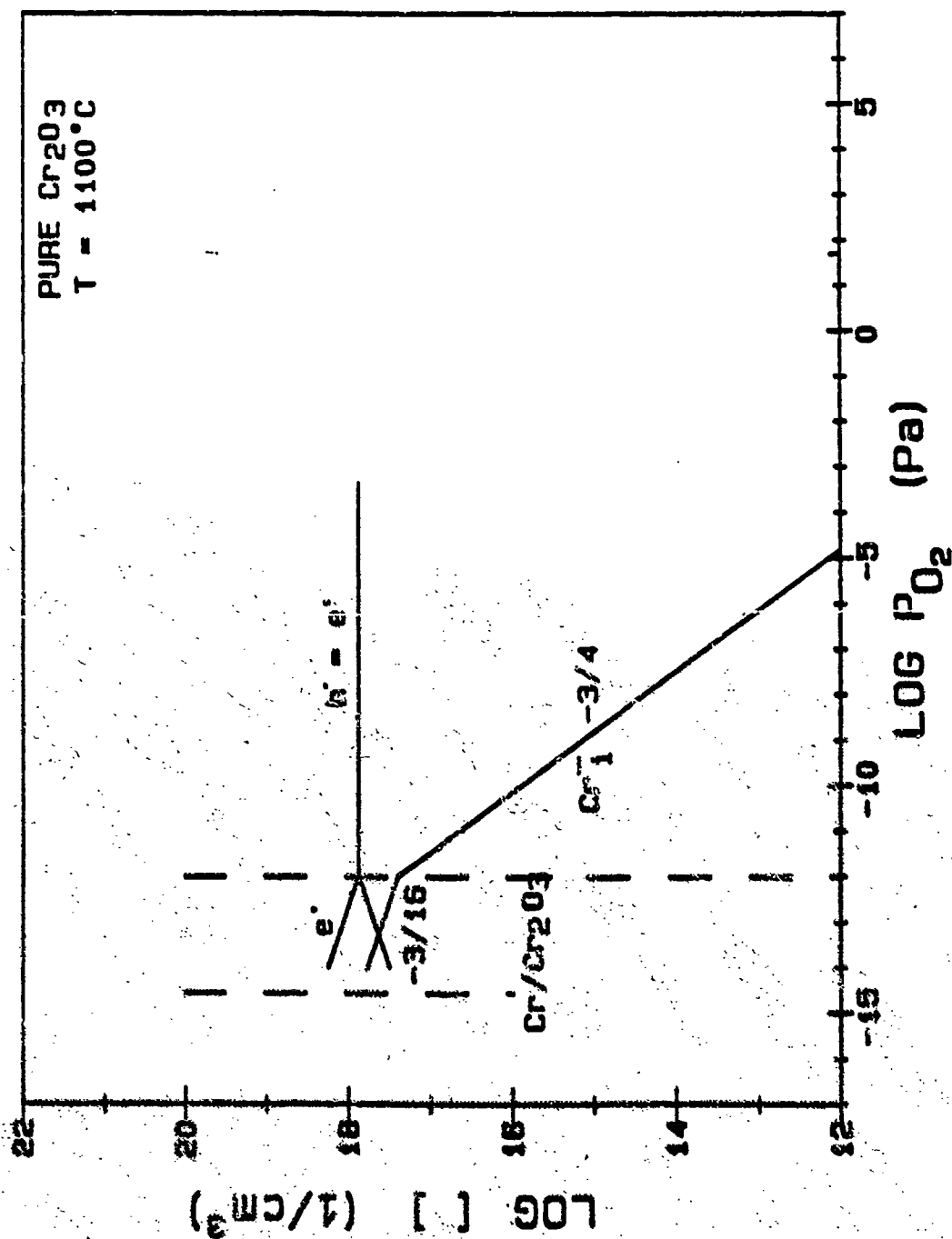


Figure 6.12: Defect concentrations vs oxygen pressure diagram for pure Cr_2O_3 in low oxygen partial pressure at 1100°C

- (4) A model of the defect structure of MgO-doped Cr_2O_3 has been proposed to explain the experimental results.
- (5) Based on the defect structure model and the experimental results, the equilibrium constants K_{Cr} ... K_{F} were calculated and the defect structure of pure Cr_2O_3 in the low P_{O_2} region can in turn be determined.

Chapter 7

POINT DEFECT STRUCTURE OF Cr_2O_3

7.1 Point Defect Structure of Cr_2O_3

Based on the results obtained from the electrical conductivity and Seebeck coefficient measurements of TiO_2 and MgO-doped Cr_2O_3 , the equilibrium constants associated with the formation of different defects in Cr_2O_3 , i.e., $K_{V_{\text{Cr}}''}$, $K_{\text{Cr}_i''}$, K_i and K_F , have been deduced. From these equilibrium constants and their corresponding defect equations (Equations 5.1 to 5.4), it is then possible to determine the point defect structure of Cr_2O_3 . Accordingly, the concentrations of the different defects have been calculated as functions of both temperature and oxygen partial pressure.

In Figure 7.1, the point defect structure of Cr_2O_3 at 1100°C is illustrated by plotting the oxygen partial pressure dependence of the defect concentrations. It appears that three distinct regions exist. In the high P_{O_2} region, near atmospheric oxygen pressure, Cr_2O_3 behaves as a P-type semiconductor with V_{Cr}'' and h^\cdot as the predominant defects. As P_{O_2} decreases, $[V_{\text{Cr}}'']$ and $[h^\cdot]$ start decreasing and $[e^\cdot]$ increases. When P_{O_2} is decreased to a certain point where $[h^\cdot] = [e^\cdot]$, the intrinsic electronic behavior becomes important. In the low P_{O_2} region, near the P_{O_2} for $\text{Cr}/\text{Cr}_2\text{O}_3$ equilibrium, Cr_2O_3 changes to an N-type semiconductor with Cr_i'' and e^\cdot as the dominant defects.

The temperature dependence of the defect structure of Cr_2O_3 is illustrated in Figure 7.2, where only the electronic defect concentrations are displaced. When temperature is increased, all three regions shift towards higher P_{O_2} 's. At temperatures above 1500°C , the intrinsic region becomes dominant even at P_{O_2}

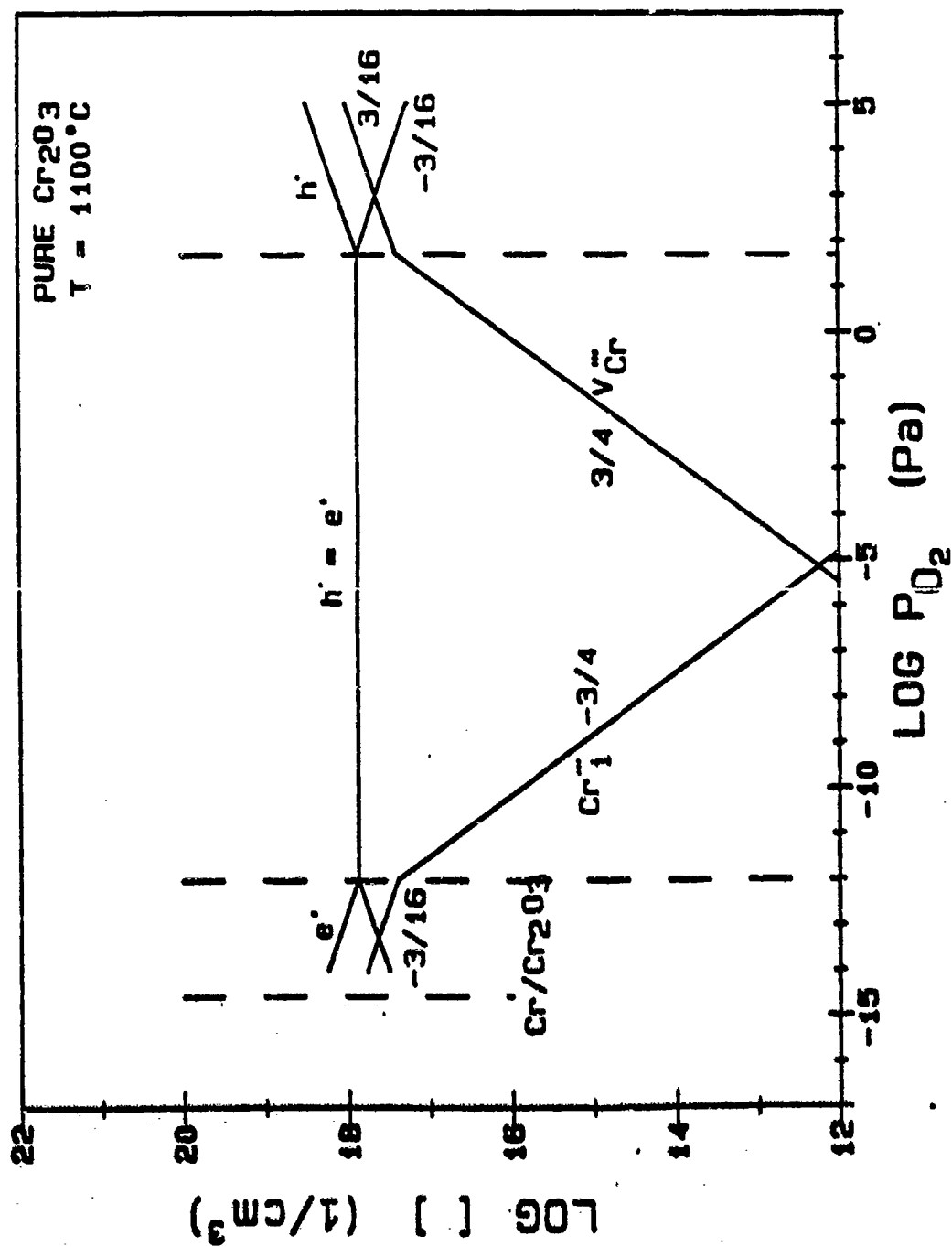


Figure 7.1: Defect concentrations vs. oxygen partial pressure diagram for pure Cr_2O_3 at 1100°C

≈ 1 atm. This kind of shift is somewhat anticipatable since all the defect formation processes are thermal activated, and all the different equilibrium constants apparently have different activation energies.

In order to verify the deduced defect structure, it is necessary to examine the different defect dependent properties of Cr_2O_3 . A fully explanation of these properties with the model is essential for its justification. In the following sections, discussions on the electrical conductivity and Seebeck coefficient, and the diffusion process related properties, i.e., the parabolic growth of pure Cr_2O_3 and the sintering of Cr_2O_3 are presented.

7.2 Electrical Conductivity and Seebeck Coefficient of Cr_2O_3

7.2.1 Electronic Conduction Mechanism

It is of interest to examine the electronic conduction mechanism of Cr_2O_3 by means of its band structure. In principle, the electronic structure of a 3d transition-metal oxide can be ascribed to an empty conduction band assumed to arise from the cation 4s levels, and a full valence band arising from the anion (oxygen) 2p levels. In addition, the 3d energy levels exist with some of them presumably located in the gap between these two bands. The 3d levels are usually considered to be localized states, even though there is a probability that they may form a very narrow band due to some overlap of their wave functions. In the case of Cr_2O_3 , the Cr^{3+} ion has three 3d electrons remaining outside the last closed-shell configuration. Electronic transport may result from the motion of charge carriers in the bands or in the localized levels or in both simultaneously.

Regarding the described band structure, several mechanisms for the generation of the intrinsic electron-hole pair are possible. Electron-hole pairs

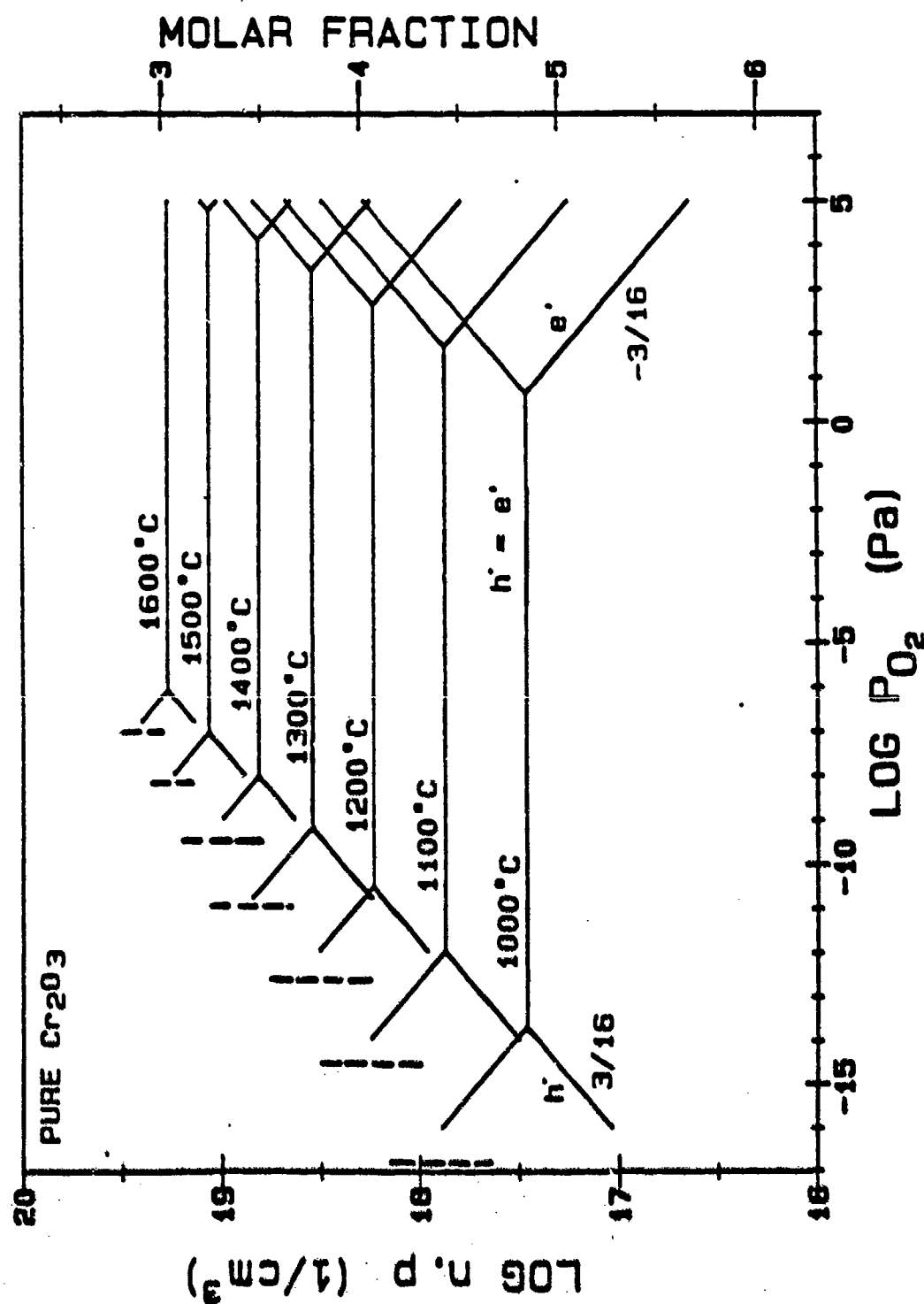


Figure 7.2: Defect concentrations vs. oxygen partial pressure diagram for pure Cr_2O_3 at temperatures between 1000°C to 1600°C

may be formed by excitation of electrons from the oxygen 2p band to the chromium 3d or 4s levels; from the 3d levels to the conduction band; or within the 3d localized levels. However, it has been pointed out by Crawford () that the formation of the electron-hole pair in the 3d levels, by



is the only reasonable process in Cr_2O_3 . Since the 3d levels are localized states, the motion of the electronic charge-carriers involves a thermally-activated diffusion, or hopping process, and is characterized by a rather low and thermally activated mobility. It has been shown in previous chapters that the mobilities of electrons and electron holes are in the range of 10^{-1} - 10^{-2} cm/V-sec, and can be expressed by

$$\mu_p = 0.29 \cdot \exp(-0.17\text{ev/kT}) \quad (7.2)$$

and

$$\mu_n = 2.67 \cdot \exp(-0.57\text{ev/kT}) \quad (7.3)$$

These results further verify the "hopping" mechanism of the charge-carriers in Cr_2O_3 . The apparent difference in the activation energies of μ_p and μ_n may be due to the different strength of the polarization field induced by electrons and electron holes. Since the chromium ion Cr^{3+} has higher charges than the oxygen ion O^{2-} , the coulombic potential well generated from Cr^{3+} is expected to be higher. Thus, the interaction between the electron and Cr^{3+} is apparently larger than that of the electron hole and O^{2-} . In turn, more energy is required for electrons than for electron holes to jump out of their induced polarization field.

7.2.2 Electrical Conductivity and Seebeck Coefficient

Based on the obtained defect structure and the electron and electron hole mobilities, the electrical conductivity of Cr_2O_3 has been calculated as functions of

temperature and P_{O_2} . Also according to the small polaron conduction mechanism, the densities of effective states, N_c and N_v and the transport energies, A_n and A_p are obtained which give $N_c = 8 \times 10^{22}$, $N_v = 1.2 \times 10^{23}$, $A_n = A_p = 0$. With these quantities, the Seebeck coefficients have also been calculated based on Equations 2.65 to 2.67.

In Figures 7.3 and 7.4, the electrical conductivities and Seebeck coefficients calculated from the defect structure are plotted, respectively. The experimental results of these two properties are also plotted on Figures 7.5 and 7.6. A very close match is found between the calculated and measured values.

7.3 Self Diffusion Coefficient of Cr in Cr_2O_3

In this section, the self-diffusion of chromium in Cr_2O_3 and the effect of impurities on the diffusion coefficient of chromium are discussed. It has been shown that the self-diffusion of the cation (Cr) in an oxide (Cr_2O_3) can be expressed by

$$D_{Cr} = \sum D_{def} \cdot [defect] = D_{V_{Cr}'''} \cdot [V_{Cr}'''] + D_{Cr_i'''} \cdot [Cr_i'''] \quad (7.4)$$

Let $R = D_{Cr_i'''} / D_{V_{Cr}'''}$, then

$$D_{Cr} = D_{V_{Cr}'''} \cdot (1 + R) \cdot ([V_{Cr}'''] + [Cr_i''']) \quad (7.5)$$

These equations indicate that with a prior knowledge of $D_{Cr_i'''}$ and $D_{V_{Cr}'''}$, D_{Cr} may be obtained from the defect concentrations.

By adopting the value of $D_{V_{Cr}'''} = 1.15 \times 10^{-12} \text{ cm}^2/\text{sec}$ from studies of Greskovich(31) and assuming $R = 0.1, 1$, and 10 , the self-diffusion coefficient of Cr in Cr_2O_3 at 1100°C have been calculated with the obtained defect concentrations. The results are plotted as a function of oxygen partial pressure in Figure 7.5. A very special behavior is seen on this figure. It appears that the

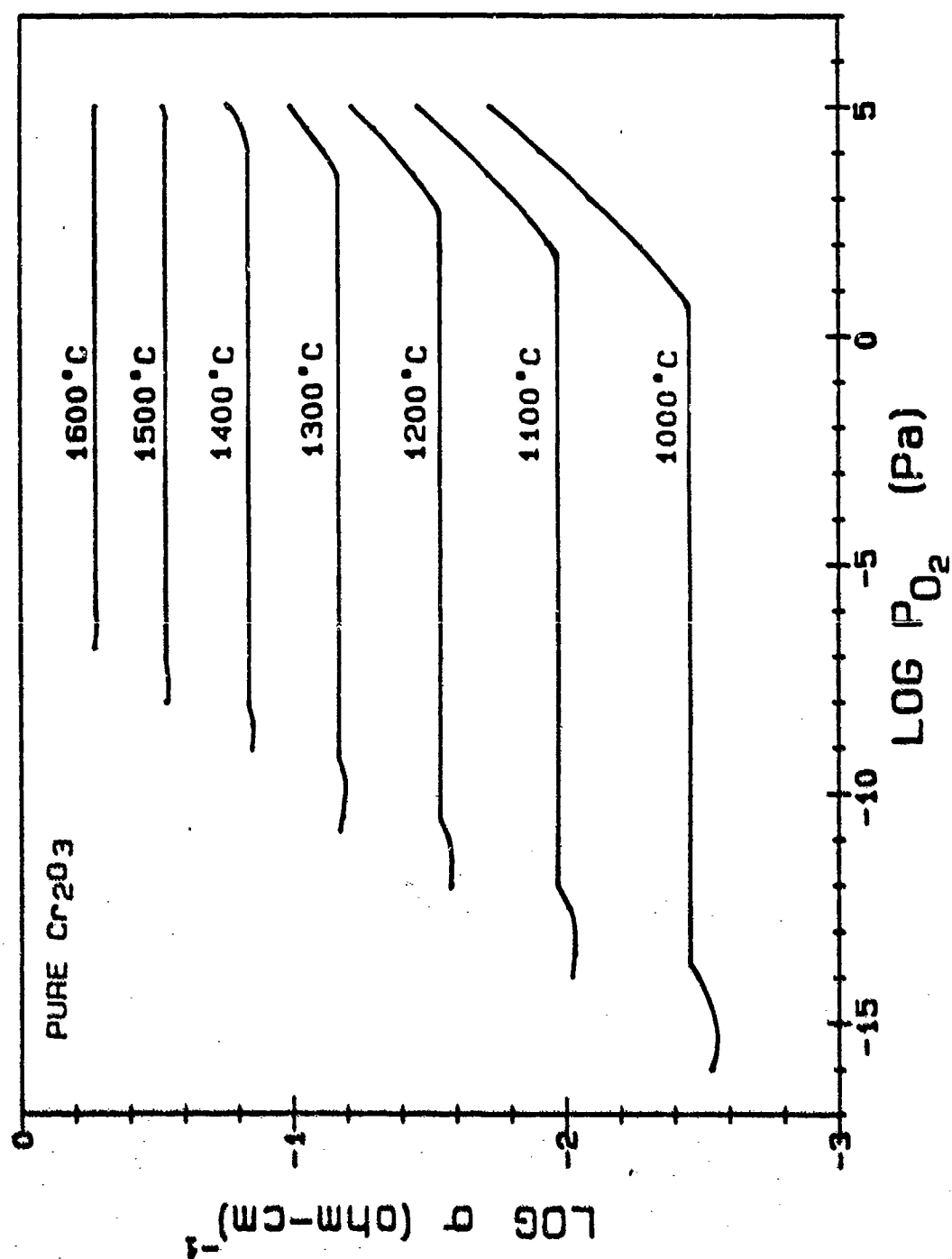


Figure 7.3: Electrical conductivity vs. oxygen partial pressure diagram for pure Cr_2O_3 at temperatures between 1000° to 1600°C

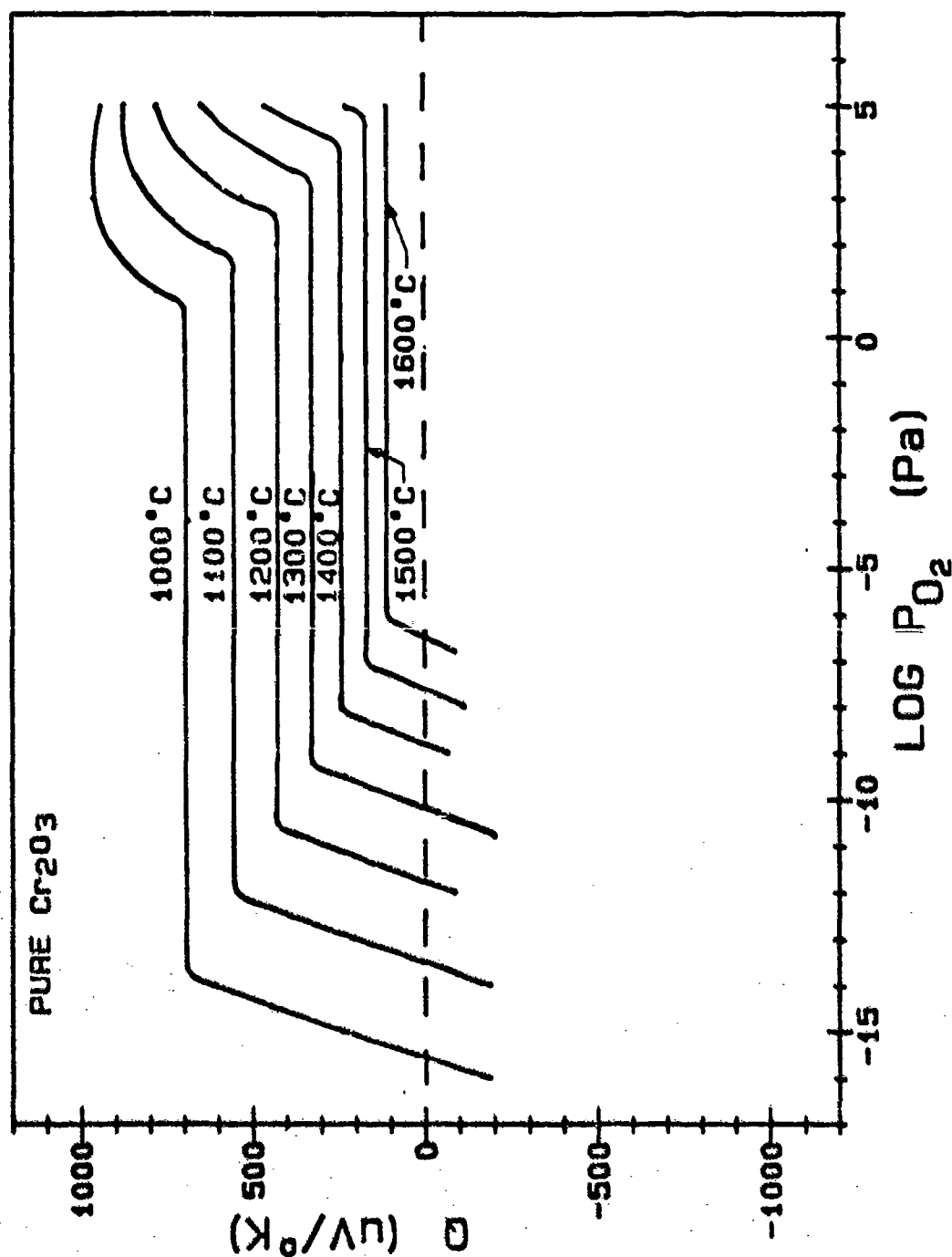


Figure 7.4: Seebeck coefficient vs. oxygen partial pressure diagram for pure Cr_2O_3 at temperatures between 1000°C to 1600°C

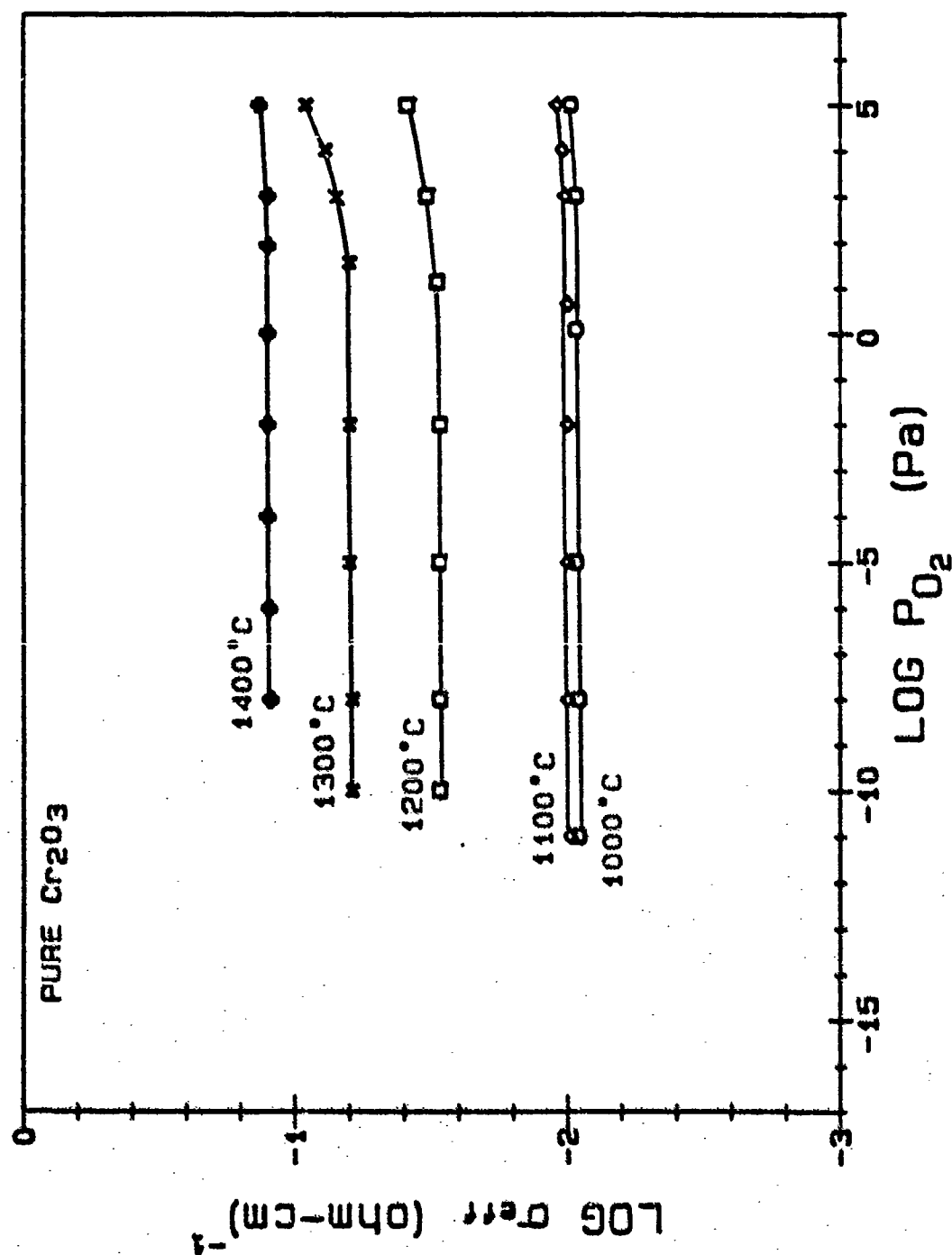


Figure 7.5: Experimental results of the electrical conductivity of pure Cr_2O_3 at temperatures between 1000° to 1400°C

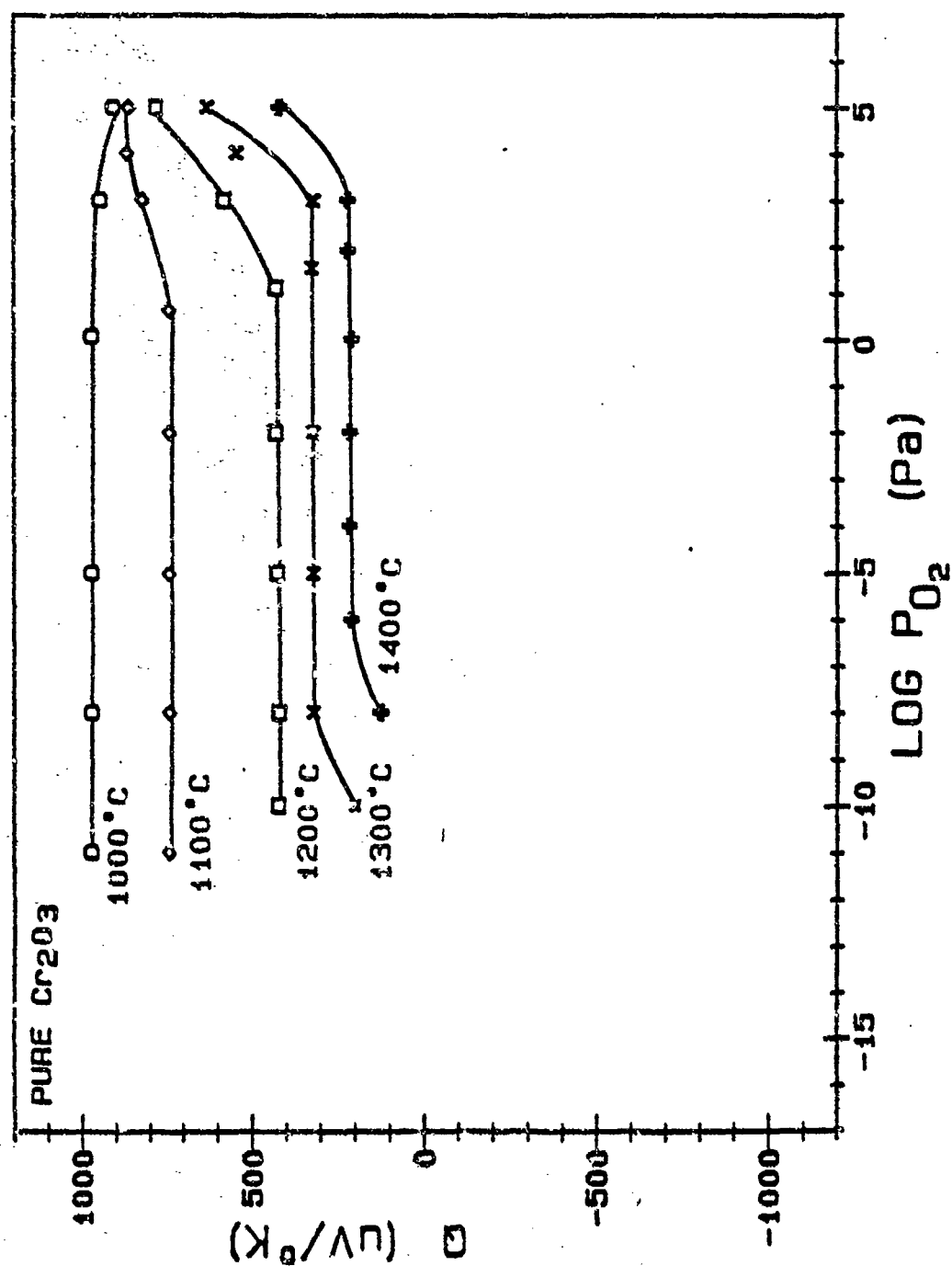


Figure 7.6: Seebeck coefficient vs. oxygen partial pressure diagram for pure Cr_2O_3 at temperatures between 1000°C to 1600°C

self-diffusion coefficient D_{Cr} is surprisingly low at an intermediate P_{O_2} region in comparison with the high and low P_{O_2} regions. If this is indeed the case, apparently, in that region other diffusion paths, such as grain-boundaries and dislocations, may easily contribute to the diffusion process along with the volume diffusion. This indication appears to be in agreement with recent studies of Atkinson and Taylor(39). They have found that diffusion along dislocations actually plays a very important role in the diffusion of Cr in Cr_2O_3 . Additionally, diffusion along grain boundaries has been considered as the reason why the reported diffusion coefficients of Cr in early studies on polycrystalline Cr_2O_3 have much higher values.

Another unavoidable factor may come from the effect of impurities. The effect can be easily seen by examining Figure 7.2. Since at $1100^\circ C$, the intrinsic electronic concentration, n_i , has a value of less than 0.005 mole/mole of Cr_2O_3 , an impurity of this amount will in fact alter the defect structure of the whole intrinsic region. For a further illustration, the diffusion coefficients of Cr in 0.05 and 0.1 mole % of higher and lower valent cation doped Cr_2O_3 have been calculated by the method mentioned above. The results are plotted in Figure 7.8 and 7.9. It is quite clear that the impurities have a significant effect on increasing the self-diffusion coefficient of Cr in Cr_2O_3 .

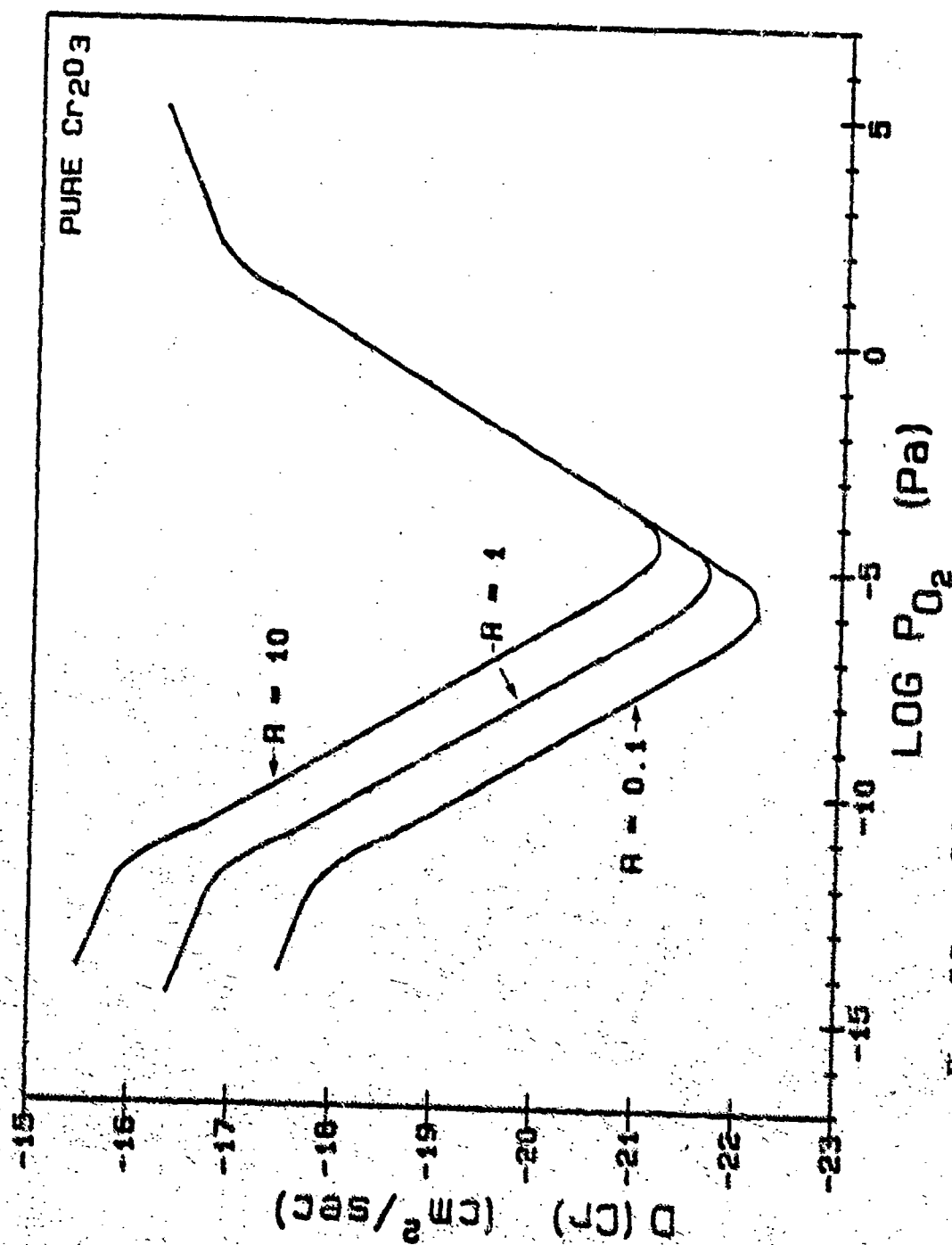


Figure 7.7: Calculated diffusion coefficient vs. oxygen partial pressure diagram for pure Cr_2O_3 at 1100°C

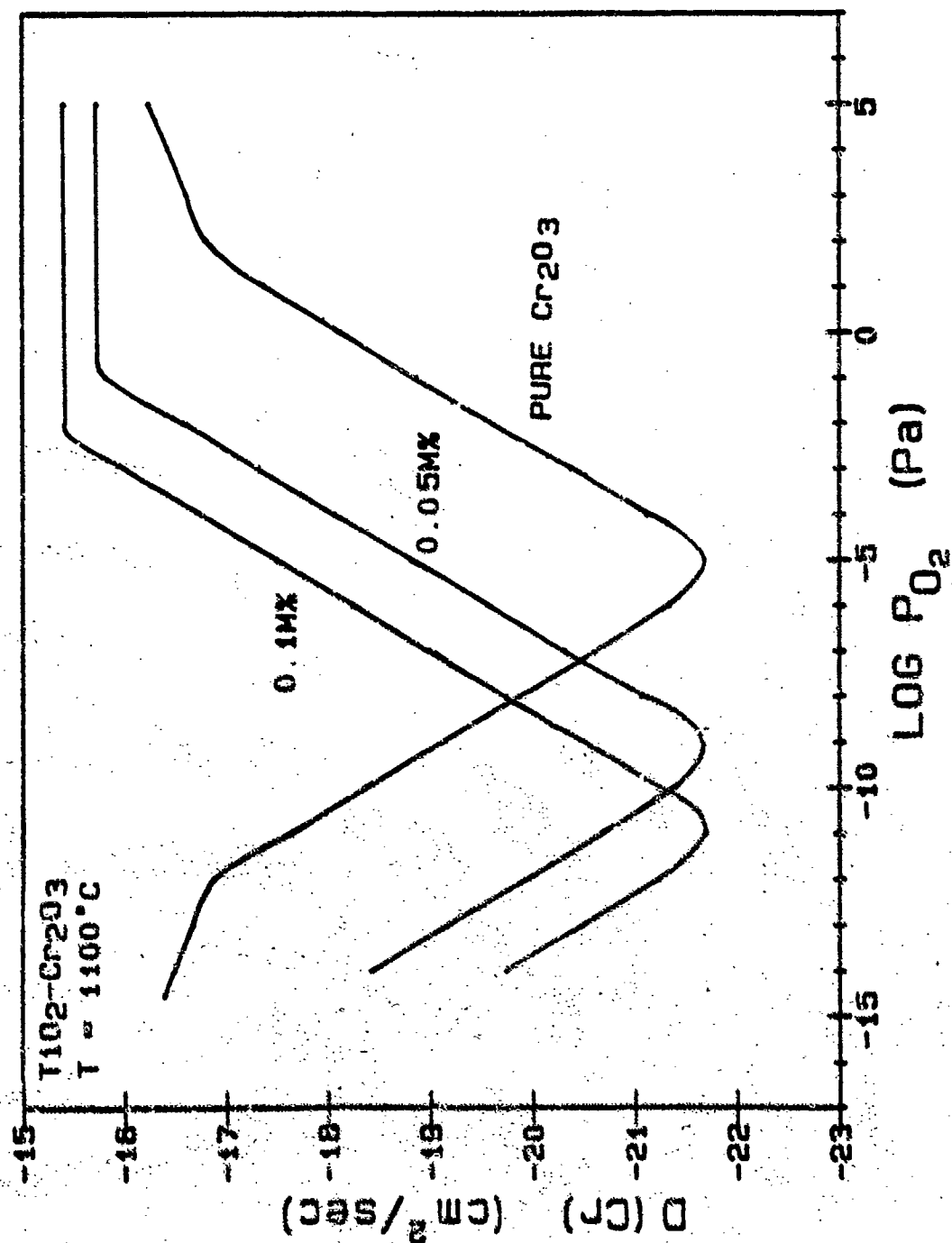


Figure 7.8: Effect of higher valent cations on the diffusion coefficient of Cr in Cr_2O_3 at 1100°C

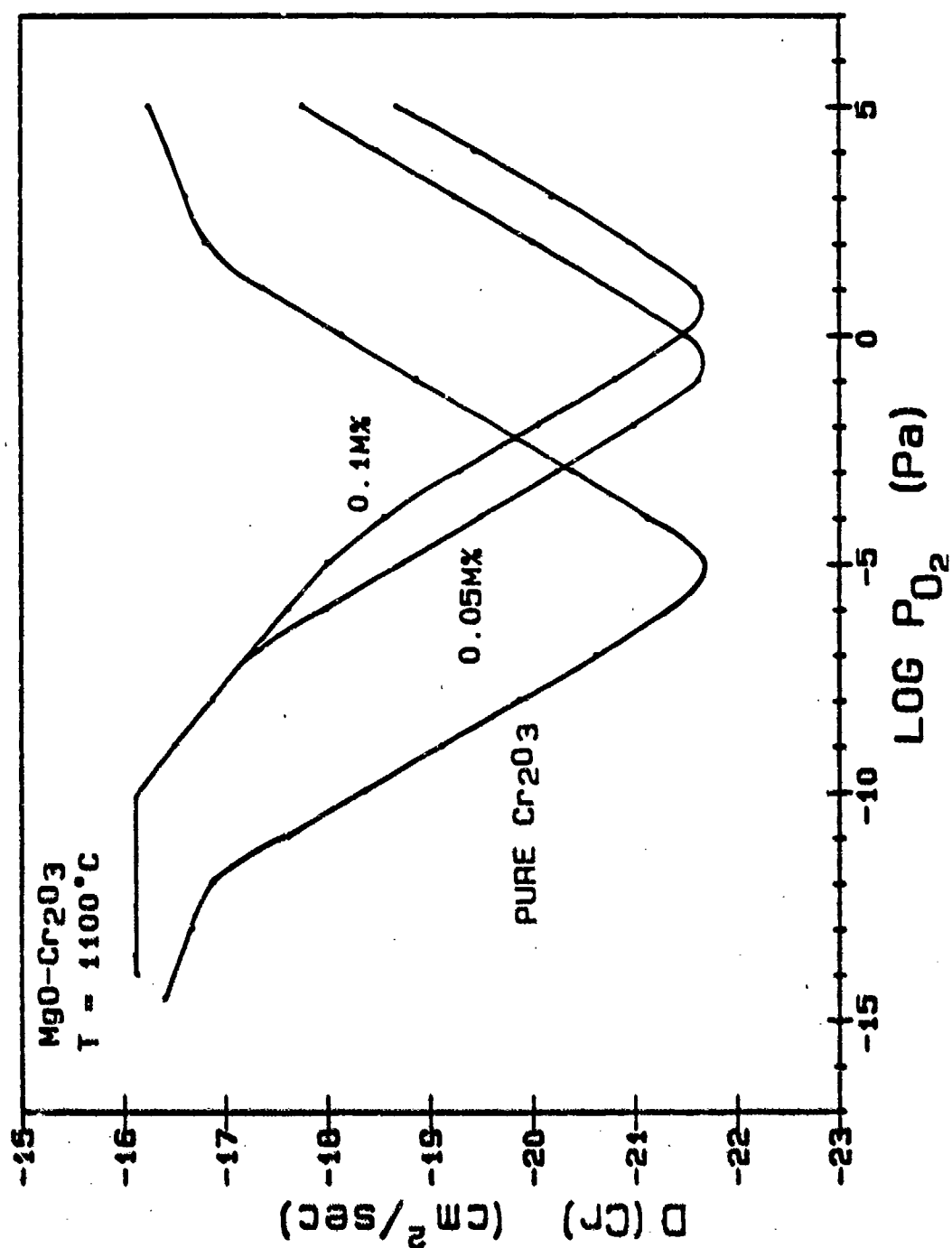


Figure 7.9: Effect of lower valent cations on the diffusion coefficient of Cr in Cr₂O₃ at 1100°C.

7.4 High Temperature Oxidation of Cr

The parabolic rate constants, K_p , of the growth of Cr_2O_3 at 1100°C has been calculated according to the equation

$$K_p = 2 \int_{P_{\text{O}_2}^{(i)}}^{P_{\text{O}_2}^{(o)}} \frac{D_{\text{Cr}}}{P_{\text{O}_2}} \ln P_{\text{O}_2} \quad (7.6)$$

with the obtained self-diffusion coefficients. The results are plotted in Figure 7.10. It is seen that for all cases, i.e, $R = 0.1, 1, 10$, a constant K_p region exists over quite a large P_{O_2} range. This kind of behavior appears to be consistent with Hindom and Whittle's observation(51). However, comparing the magnitudes of these K_p 's with the reported values, it is found that the calculated values are much smaller than the experimental results. Apparently, short circuit diffusion and impurity effects must have again played important roles in the high temperature oxidation of Cr.

The effect of impurities on the rate constant has also been evaluated, and are shown in Figures 7.11 and 7.12. It appears that higher valent cation (Ti) impurities have much significant effects on the variation of the rate constant to the oxygen partial pressure. Since their presence in Cr_2O_3 increases the concentration of Cr vacancies, the rate constant becomes strongly oxygen partial pressure dependent. On the other hand, the rate constant of the lower valent cation (Mg) doped Cr_2O_3 is independent upon the oxygen partial pressure due to the predominance of Cr interstitials.

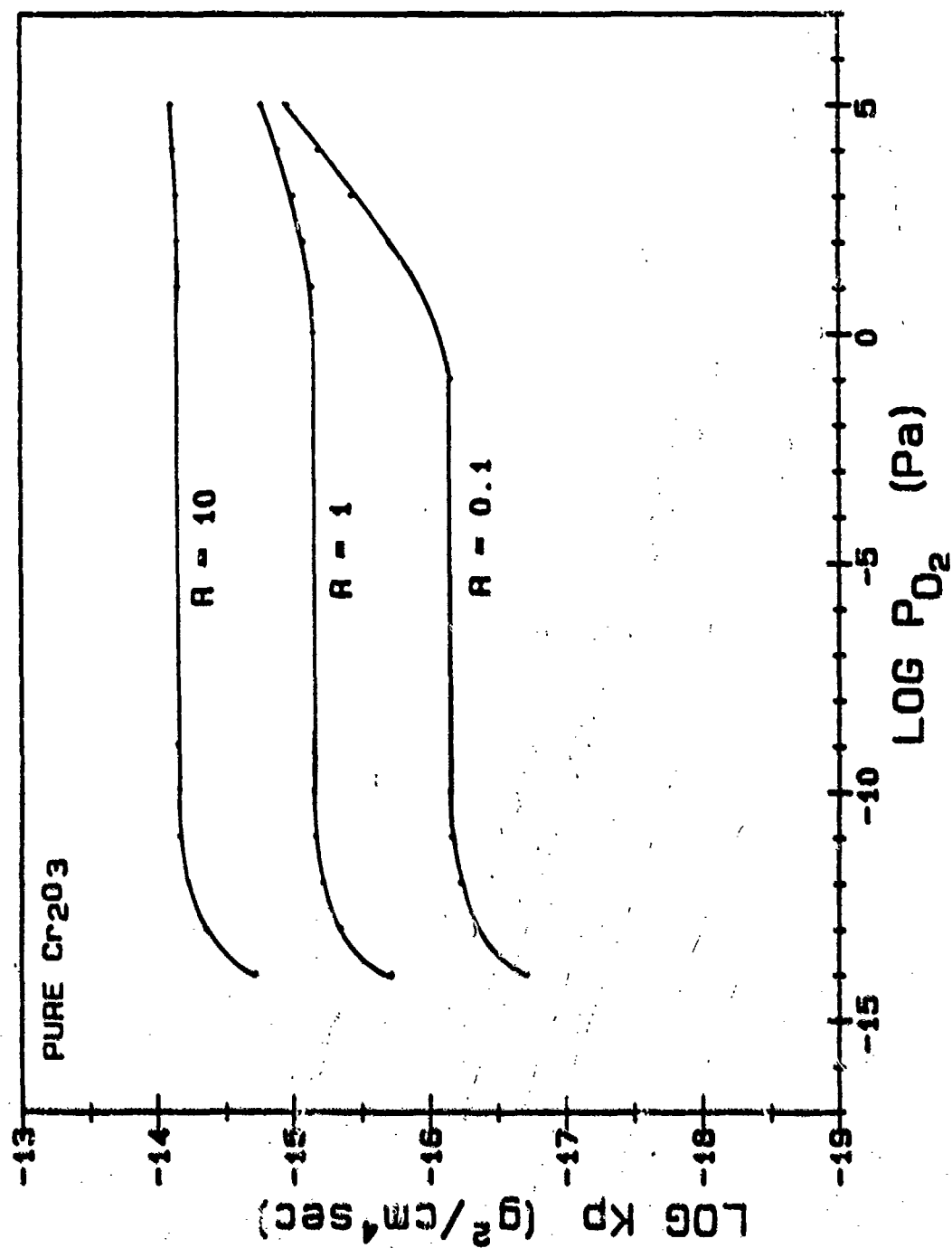


Figure 7.10: Calculated parabolic rate constant vs. oxygen partial pressure diagram for pure Cr_2O_3 at 1100°C

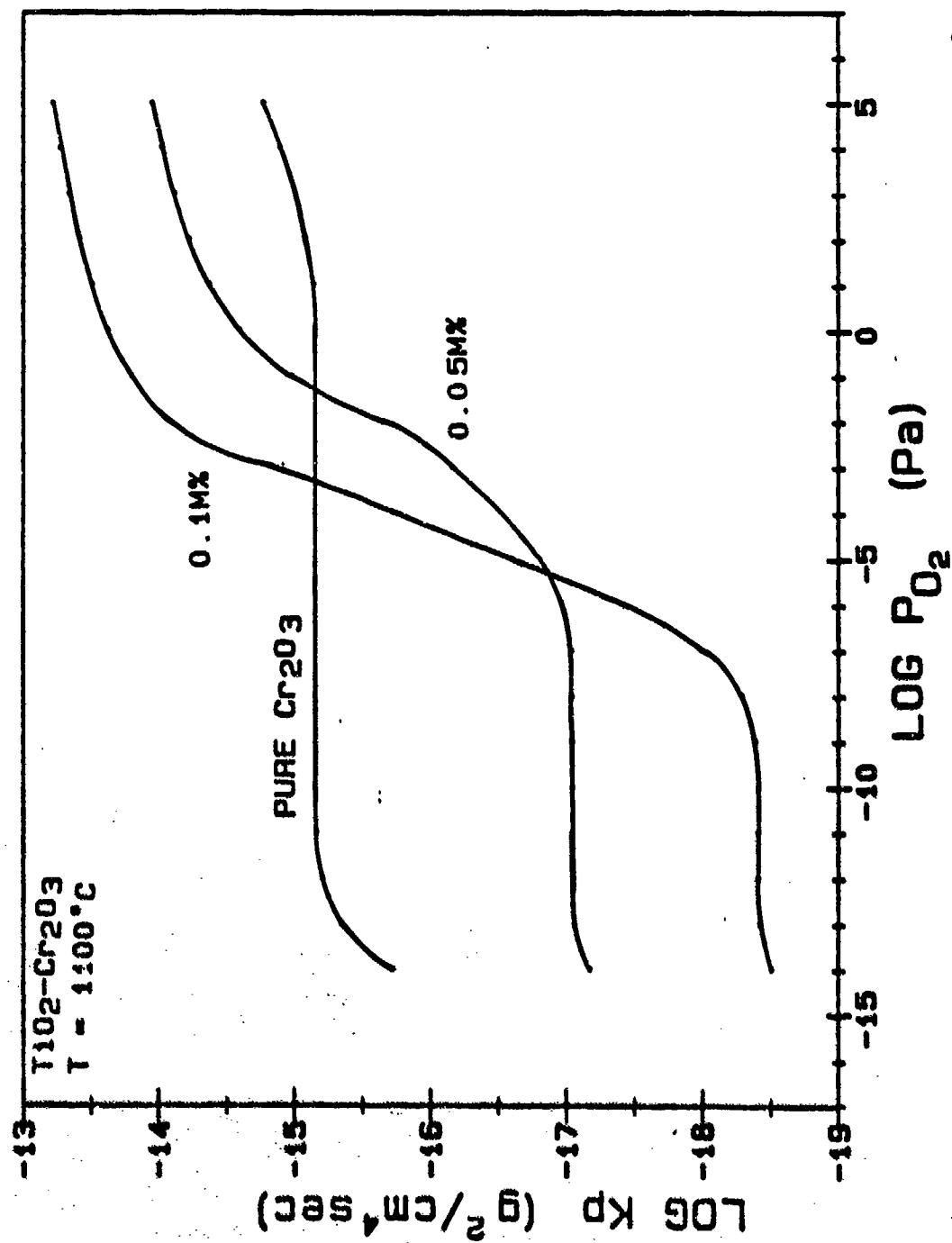


Figure 7.11: Effect of higher valent cations on the parabolic rate constant of the growth of Cr_2O_3 at 1100°C .

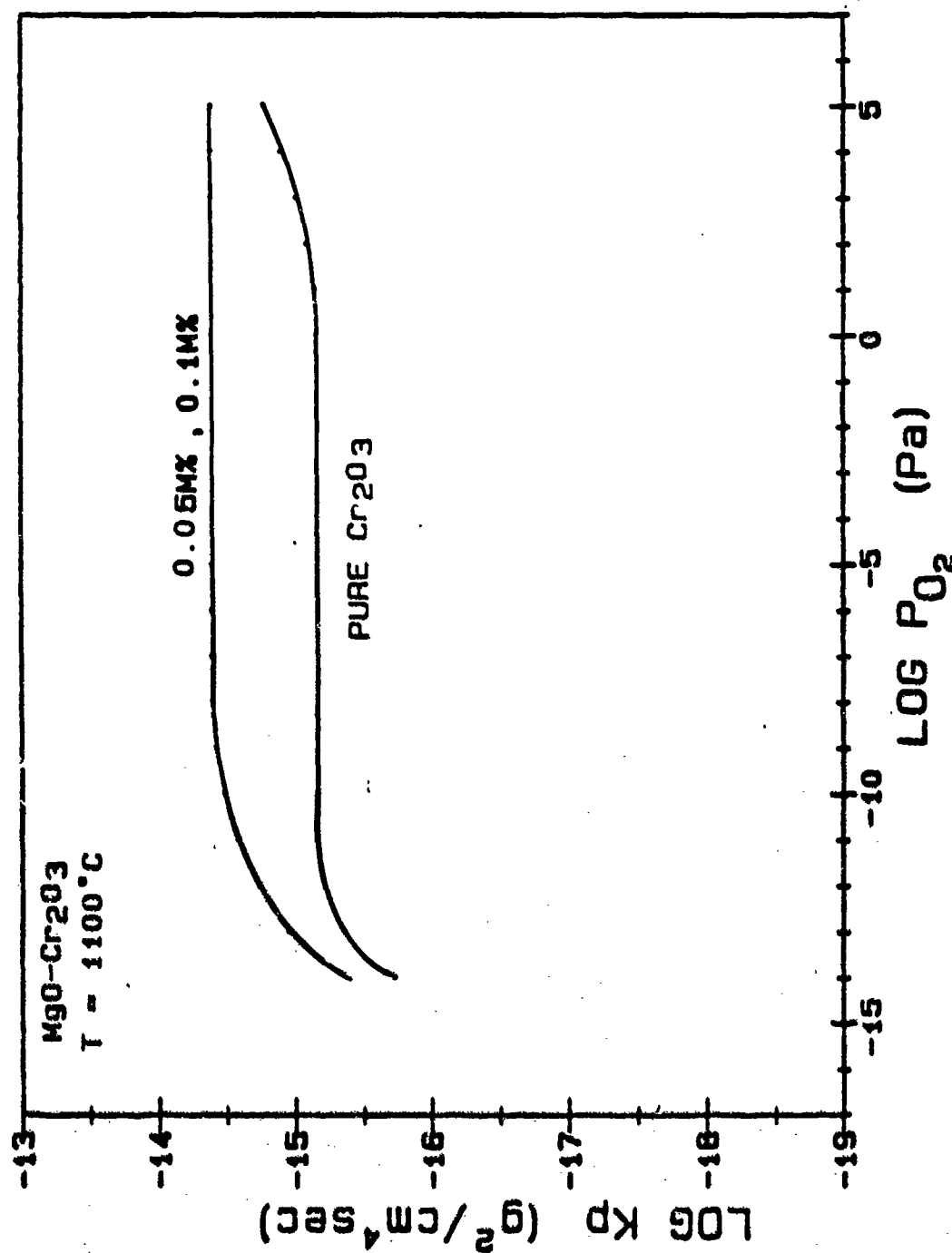


Figure 7.12: Effect of lower valent cations on the parabolic rate constant of the growth of Cr₂O₃ at 1100°C.

7.5 Sintering of Cr_2O_3

It has been shown that the rate of sintering of Cr_2O_3 is determined by the migration of the oxygen atoms through oxygen vacancies. The generation of oxygen vacancies will involve the reaction:



$$K_{\text{V}_\text{O}^\cdot} = [\text{V}_\text{O}^\cdot] \cdot [\text{e}^-]^2 \cdot \text{P}_{\text{O}_2}^{1/2} \quad (7.8)$$

Although there is no information about the equilibrium constant $K_{\text{V}_\text{O}^\cdot}$, a qualitative analysis can still be applied. From Equation 7.8, the concentration of oxygen vacancies is given by

$$[\text{V}_\text{O}^\cdot] = K_{\text{V}_\text{O}^\cdot} [\text{e}^-]^{-2} \cdot \text{P}_{\text{O}_2}^{-1/2} \quad (7.9)$$

Thus in regions where $[\text{e}^-] \propto \text{P}_{\text{O}_2}^{-3/16}$, $[\text{V}_\text{O}^\cdot] \propto \text{P}_{\text{O}_2}^{-1/8}$ and in regions where $[\text{e}^-] = \text{constant}$, $[\text{V}_\text{O}^\cdot] \propto \text{P}_{\text{O}_2}^{-1/2}$. In Figure 7.13, the variation of the oxygen vacancy at 1600°C is plotted as a function of P_{O_2} . According to this figure, in most of the P_{O_2} range the concentration of oxygen vacancies will increase with decreasing oxygen partial pressure as $\text{P}_{\text{O}_2}^{-1/2}$. Thus in terms of the volume diffusion theory of the sintering mechanism, the rate of sintering of Cr_2O_3 will also increase with a decrease in P_{O_2} , which is in good agreement with experimental observation.

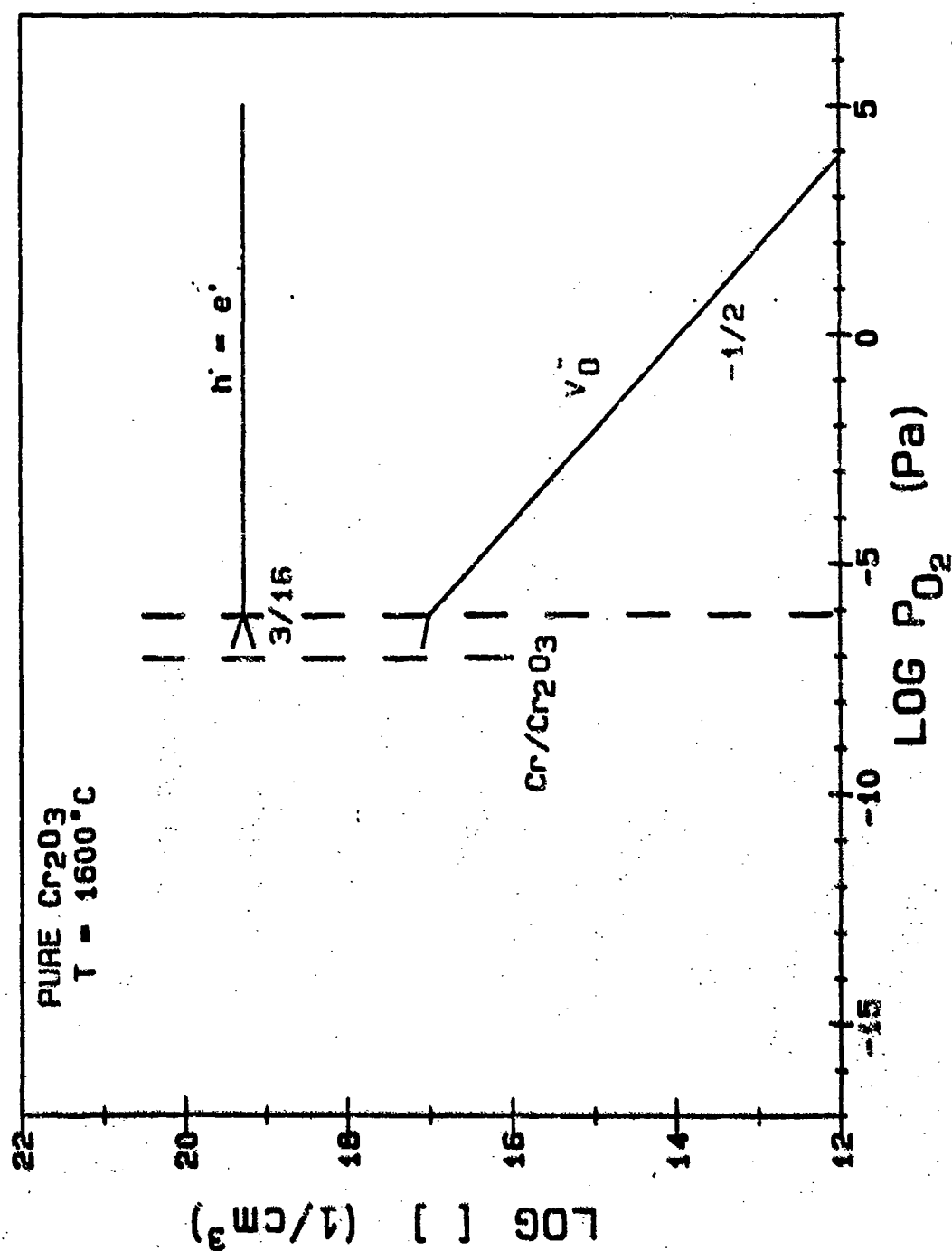


Figure 7.13: Oxygen partial pressure dependence of the concentration of oxygen vacancies in Cr_2O_3 at 1660°C .

Chapter 8

SUMMARY AND SUGGESTIONS FOR FUTURE RESEARCH

This chapter briefly summarizes the present research results and outlines suggestions for related future research. It is hoped that this work has contributed to our understanding of the point defect structure of Cr_2O_3 and its related transport properties.

8.1 Summary of the results

On the basis of this research work, the following conclusions have been obtained:

- (1) It is found that the point defect structure of Cr_2O_3 is complicated. The type of defects present are dependent upon the temperature, the oxygen partial pressure, and the amount of impurities. In general, at high temperature, Cr_2O_3 behaves as a P-type semiconductor at high P_{O_2} 's, an intrinsic semiconductor at intermediate P_{O_2} 's, and an N-type semiconductor at low P_{O_2} 's (near Cr/ Cr_2O_3 equilibrium P_{O_2}).
- (2) When the electronic transport properties are considered, both electrons and electron holes appear to contribute to the process of conduction. It was found that $\mu_p > \mu_n$. Based on the magnitude of the electron and electron hole mobilities and their activation energies, the conduction mechanism in Cr_2O_3 appears to be through small polaron conduction.
- (3) Impurities have very significant effects on altering the defect structure of Cr_2O_3 and changing its transport properties. When Cr_2O_3 is doped with a higher valent cation (Ti), the electron conductivity is increased; on the

other hand, when a lower valent cation is the dopant, the electron hole conductivity is increased.

- (4) It has also been found that the volume diffusion of Cr in Cr_2O_3 is too slow to be totally responsible for some of the diffusion dependent properties, e.g., high temperature oxidation of Cr. Other factors such as impurity effects and the short-circuit diffusion along grain boundaries, dislocations, etc., may have equivalent contributions.
- (5) Sintering of Cr_2O_3 at temperatures higher than 1600°C is apparently controlled by the migration of the minority ionic defects, i.e., oxygen vacancies.

8.2 Suggestions for Future Research

Although the point defect structure of Cr_2O_3 has been studied quite extensively in this work, there are still questions related to the point defects of Cr_2O_3 that need to be answered.

- (1) Since in this study, only one type of dopant has been intentionally added to Cr_2O_3 at one time, the counter effects of the co-existence of two opposite type impurities have not yet been studied. It is of interest to examine this effect by the simultaneous doping with two opposite type of dopants. Theoretically, the appearance of opposite type of dopants will enhance the solubility of both dopants in the host crystal. Therefore, a more dramatic change in the defect structure of Cr_2O_3 will be expected.
- (2) It has been known for a long time that small addition of inert dispersed phases such as ThO_2 , Y_2O_3 etc., will decrease the parabolic rate constant of Cr_2O_3 growth. However the actual mechanism involved has not yet

been fully understood. In order to elucidate these phenomena investigations on the defect chemistry of these systems are required.

- (3) From this study it was found that the solubility of a second phase in a crystal can be revealed through the measurement of the electrical conductivity as a function of oxygen partial pressure, and the content of the second phase. This may be an alternative way of studying systems involving very low solubilities such as SiO_2 in Cr_2O_3 .

BIBLIOGRAPHY

1. F.A. Kröger, The Chemistry of Imperfect Crystals, 2nd edit., North-Holland/American Elsevier, New York, 1974.
2. W. D. Kingery, H. K. Bowen and D. R. Uhlmann, Introduction to Ceramics, 2nd edit., John Wiley & Sons, Inc., 1976.
3. Stanislaw Mrowec, Defects and Diffusion in Solids An Introduction, Elsevier/North-Holland, Inc., 1974.
4. Kofstad, Nonstoichiometry, Diffusion, and Electrical Conductivity in Binary Metal Oxides, Wiley-Interscience, New York, 1972.
5. N. M. Tallan, editor, Electrical Conductivity in Ceramics and Glass, Marcel Dekker, Inc., New York, 1974.
6. F. A. Kröger and H. J. Vink, "Relations Between the Conductions of Imperfections in Crystalline Solids," pp. 307-435, Vol III, Solid State Physics, F. Seitz and D. Turnbull, Eds., Academic Press Inc., New York, 1965.
7. R. Dieckmann, "Point Defects and Transport Properties of Binary and Ternary Oxides," Solid State Ionics, 12, 1-22 (1948).
8. C. Wagner, "Point Defects and their Interaction," Ann. Rev. Mater. Sci., 7, 1-22 (1977)
9. R. A. Smith, Semiconductors, 2nd edition, Cambridge University Press, 1978.
10. A. Joffe, "Properties of Various Semiconductors," J. Phys. Chem. Solids, 8, 6-14 (1959).
11. H. Frölich and G. L. Sewell, "Electric Conduction in Semiconductors," Proc. Phys. Soc., 74, 643-47 (1959).
12. M. J. Klinger, "Low Mobility Transport Phenomena in Semiconductors," pp. 205-215, Proc. Vth Int. Conf. on Phys. of Semiconductors, Inst. of Phys. London, 1962.
13. A. J. Bosman and H. J. van Daal, "Small-Polaron versus Band Conduction in some Transition-Metal Oxides," Advances in Physics, 19 [77] 1-117 (1970).
14. C. Wagner, "The Thermoelectric Power of Cells with Ionic Compounds Involving Ionic and Electronic Conduction," In. Progress in Solid State Chemistry, Edited by J. O. McCaldin and G. Somorjai, Vol 7. p.1-37 (1972).

15. K.-D. Schotte, "The Thermoelectric Properties of the Small Polaron," *Z. F. Physik*, 196, 393-414 (1966).
16. J. Yahia, "Dependence of the Electrical Conductivity and Thermo- electric Power of Pure and Aluminum-Doped Rutile on Equilibrium Oxygen Pressure and Temperature," *Phys. Review*, 130 [5] 1711-19 (1963)
17. A. Z. Hed and D. S. Tannhauser, "High-Temperature Electrical Properties of Manganese Monoxide," *J. Chem. Phys.*, 47[6] 2090-2103 (1967).
18. A. Trestman-Matts, S. E. Dorris, and T. D. Mason, "Measurement and Interpretation of Thermopower in Oxides," *J. Amer. Ceram. Soc.*, 66[8] 589-92 (1983)
19. H.-C. Chen, E. Gartstein, and T. O. Mason, "Conduction Mechanism Analysis for $\text{Fe}_{1-\delta}$ and $\text{Co}_{1-\delta}$," *J. Phys. Chem. Solids*, 43 [10] 991-95 (1982).
20. K. Hauffe, "Oxidation of Metals," Plenum Press, New York (1965).
21. P. Kofstad, "High-Temperature Oxidation of Metals," John Wiley & Sons, Inc., New York (1966).
22. D. P. Whittle, F. Gesmundo, and F. Viani, "The Parabolic Growth of Oxide Solid Solutions on Binary Alloys : A Semiempirical Approach," *Oxid. Met.*, 16, 81-99 (1981).
23. F. Gesmundo and F. Viani, "Application of Wagner's Theory to the Parabolic Growth of Oxides Containing Different Kinds of Defects. I. Pure Oxides," *J. Electrochem. Soc.*, 128[2] 460-69 (1981).
24. F. Gesmundo and F. Viani, "Application of Wagner's Theory to the Parabolic Growth of Oxides Containing Different Kinds of Defects. II. Pure Oxides," *J. Electrochem. Soc.*, 128[2] 470-79 (1981).
25. D. Caplan and M. Cohen, "The Volatilization of Chromium Oxide," *J. Electrochem. Soc.*, 108[5] 438-42 (1961).
26. R. T. Grimley, R. P. Burns, and M. G. Inghram, "Thermodynamics of the Vaporization of Cr_2O_3 : Dissociation Energies of CrO , CrO_2 and CrO_3 ," *J. Chem. Phys.*, 34 [2] 664-67 (1961)
27. E. A. Gulbransen and S. A. Jansson, "Thermochemistry of Gas-Metal Reactions," in "Oxidation of Metals and Alloys," ASM 1970 Seminar.
28. H. C. Graham and H. H. Davis, "Oxidation/Vaporization Kinetics of Cr_2O_3 " *J. Am. Ceram. Soc.*, 54 [2] 89-93 (1971).
29. R. E. Newnham and Y. M. DeHann, "Refinement of the α Al_2O_3 , TiO_2 , V_2O_3 and Cr_2O_3 Structures," *Z. F. Krist.*, 117, 235-37 (1962).
30. L. N. Cojocaru, "Electrical Properties of Non-Stoichiometric Cr_2O_3 ," *Z. Phys. Chem., N. F.*, 64, 255-62 (1969).

31. C. Greskovich, "Deviation from Stoichiometry in Cr_2O_3 at High Oxygen Partial Pressures," J. Am. Ceram. Soc., 67 [6] C-111-C112 (1984).
32. P. Kofstad, pp. 203-208 in Nonstoichiometry, Diffusion, and Electrical Conductivity in Binary Metal Oxides. Wiley-Interscience, New York, 1972.
33. R. Lindner and A. Åkerström, Z. Phys. Chem, N. F., 6, p162 (1956).
34. W. C. Hagel and A. V. Seybolt, "Cation Diffusion in Cr_2O_3 ," J. Electrochem. Soc., 108 [12] 1146-52 (1961).
35. L. C. Walters and R. E. Grace, "Self-Diffusion of ^{51}Cr in Single Crystals of Cr_2O_3 ," J. Appl. Phys., 36 [7] 2331-32 (1965).
36. W. C. Hagel, "Anion Diffusion in $\alpha\text{-Cr}_2\text{O}_3$," J. Am. Ceram. Soc., 48[2] 70-75 (1965)
37. P. Kofstad and K. P. Lillerud, : On High Temperature Oxidation of Chromium, II. Properties of Cr_2O_3 and The Oxidation Mechanism of Chromium," J. Electrochem. Soc., 127 [11] 2410-19 (1980).
38. K. Hoshino and N. L. Peterson, "Cation Self-Diffusion in Cr_2O_3 ," J. Am. Ceram. Soc., 66 [11] C-202-C-203 (1983).
39. A. Atkinson and R. I. Taylor, "Diffusion of ^{51}Cr Tracer in Cr_2O_3 and the Growth of Cr_2O_3 films," pp.285-95 in Transport in Nonstoichiometric Compounds, Edited by G. Simkovich and V. S. Stubican, Plenum, New York, 1985.
40. P. D. Ownby and G. E. Jungquist, "Final Sintering of Cr_2O_3 ," J. Am. Ceram. Soc., 55 [9] 433-36 (1972).
41. N. Toker and L. S. Darken, "Preparation of Crucibles and the Defect Structure of Cr_2O_3 ," Geochim. Cosmochim. Acta, 39, 847-52 (1975).
42. J. W. Halloran and H. U. Anderson, "Influence of O_2 Partial Pressure on Initial Sintering of Alpha Cr_2O_3 ," J. Am. Ceram. Soc., 57 [3] 150 (1974).
43. J. M. Neve and R. L. Coble, "Initial Sintering of Cr_2O_3 ," J. Am. Ceram. Soc., 57 [6] 274-75 (1974).
44. W. D. Callister, M. L. Johnson, I. B. Cutler, and R. W. Ure, Jr., "Sintering Chromium Oxide with the Aid of TiO_2 ," J. Am. Ceram. Soc., 62 [3-4] 208-11 (1979).
45. M-Y. Su, H-Y Chang and G. Simkovich, " Diffusion in Cr_2O_3 Via Initial Sintering Experiments," pp.385-95 in Transport in Nonstoichiometric Compounds, Edited by G. Simkovich and V. S. Stubican, Plenum, New York, 1985.
46. K. P. Lillerud and P. Kofstad, "On High Temperature Oxidation of Chromium," I. Oxidation of Annealed, Thermally Etched Chromium at $800^\circ\text{-}1100^\circ\text{C}$," J. Electrochem. Soc., 127 [11] 2397-2409 (1980).

47. K. P. Lillerud and P. Kofstad, "On High Temperature Oxidation of Chromium," II. Oxidation of Annealed, Thermally Etched Chromium at 800°-1100°C," J. Electrochem. Soc., 127 [11] 2410-19 (1980).
48. P. Kofstad and K. P. Lillerud, "Chromium Transport Through Cr₂O₃ Scales. I. On Lattice Diffusion of Chromium," Oxid. Met., 17 [3/4] 177-194 (1982).
49. P. Kofstad and K. P. Lillerud, "Chromium Transport Through Cr₂O₃ Scales. II. Changes in Scale Morphology During High Vacuum Treatment of Oxidized Chromium Specimens," Oxid. Met., 17 [3/4] 195-203 (1982).
50. K. P. Lillerud and P. Kofstad, "Reoxidation of Chromium with Densified Cr₂O₃ Scales," Oxid. Met. 17 [1/2] 127-39 (1982).
51. H. Hindam and D. P. Whittle, "Microstructure, Adhesion and Growth Kinetics of Protective Scales on Metals and Alloys," Oxid. Met., 18 [5/6] 245-84 (1982).
52. D. Caplan, A. Harvey, and M. Cohen, Corros. Sci. 3, p.161 (1963).
53. D. Caplan and G. I. Sproule, "Effect of Oxide Grain Structure on the High-Temperature Oxidation of Cr," Oxid. Met., 9 [5] 459-72 (1975).
54. W. C. Hagel, "Factors Controlling the High-Temperature Oxidation," Trans. ASM., 56, 583-599 (1963).
55. D. J. McPherson and M. G. Fontana, "Preparation and Properties of Titanium Chromium Binary Alloy," Trans.ASM, 43, 1098-1125 (1951).
56. P. Kofstad, "High Temperature Oxidation of Metals," John Wiley and sons, New York, 1966.
57. T. F. Kassner, L. C. Walters and R. E. Grace, Proceedings of "Symposium on Thermodynamics with Emphasis on Nuclear Materials and Atomic Transport in Solids," IAEA, Vienna, 1966.
58. H. Hindom and D. P. Whittle, "Evidence for the Growth Mechanism of Cr₂O₃ at Low Oxygen Potentials," J. Electrochem. Soc., 130 [7] 1519-23 (1983).
59. F. A. Kröger, "Defects and Transport in SiO₂, Al₂O₃, Cr₂O₃," pp. 89-100, Proceeding of NACE Conference on "High Temperature Corrosion," San Diego, California (March 1981).
60. J. A. Crawford and R. W. Vest, "Electrical Conductivity of Single-Crystal Cr₂O₃," J. Appl. Phys., 35 [8] 2413-18 (1964).
61. K. Hauffe and J. Block, "Fehlorderungsmodell eines Eigenstörstellen-Halbleiters am Beispiel des Chromoxyds," J. Z. Phys. Chem. (Lps), 198, 222-47 (1951).

62. W. A. Fischer and G. Lorenz, "Die Sauerstoffdruckabhängigkeit der Elektrischen Eigenschaften des Chrom(III) Oxydes," Z. Physik. Chem. N. F., 18, 308-329 (1958).
63. G. Lorenz and W. A. Fischer, "Der Leitungsmechanismus im Chrom(III) Oxyd bei hohen Temperaturen," Z. Physik. Chem. N. F., 18, 265-280, (1958).
64. F. G. Hicks, D. R. Holmes and D. B. Meadowcroft, "Defect Structure and Transport Properties of Oxide Solid Solutions Containing Cr_2O_3 ," in "The 4th International Conference of Corrosion" 1969, p.379-84
65. D. B. Meadowcroft and F. G. Hicks, "Electrical Conduction Processes and Defect Structure of Chromium Oxide," Proc. Br. Ceram. Soc., 23, 33-41 (1972).
66. K. A. Hay, F. G. Hicks, and D. R. Holmes, "The Transport Properties and Defect Structure of the Oxide $(\text{Fe}, \text{Cr})_2\text{O}_3$ Formed on Fe-Cr Alloys," D. R. Werkst. Korros., 21, 917-24 (1970).
67. E. W. A. Young, P. C. M. Stiphout, and J. H. W. de Wit, "N-type Behavior of Chromium(III) Oxide," J. Electrochem. Soc., 132 [4] 884-86 (1985).
68. W. A. Fischer and H. Dietrich, "Über die Kinetik des Einbaues von gleich und niederwertigen Fremdzusätzen in das Chrom(III) Oxid und ihre Auswirkung auf die elektrischen Eigenschaften," Z. Physik. Chem. N. F., 41, 205-223 (1964).
69. W. A. Fischer and H. Dietrich, "Über die Kinetik des Einbaues von höherwertigen Fremdausätzen in das Chrom(III) Oxid," Z. Physik. Chem. N. F., 41, 287-303 (1964).
70. W. C. Hagel, "Electrical Conductivity of Li-Substituted Cr_2O_3 ," J. Appl. Phys., 36 [8] 2586-87 (1965).
71. R. F. Huang, A. K. Agarwal and H. U. Anderson, "Oxygen Activity Dependence of the Electrical Conductivity of Li-Doped Cr_2O_3 ," J. Am. Ceram. Soc., 67 [2] 146-50 (1984).
72. H. Nagai, T. Fujikawa and K. Shoji, "Electrical Conductivity of Cr_2O_3 Doped with La_2O_3 , Y_2O_3 and NiO ," Trans. Japan Inst. Metals, 24 [8] 581-88 (1983). A. Muan, E. F. Osborn, "Phase Equilibria Among Oxides in Steelmaking," Addison-Wesley Publishing Company, Inc. (1965).
73. L. S. Darken and R. W. Gurry, "The System Iron-Oxygen, I. The Wüstite Field and Related Equilibria," J. Am. Chem. Soc., 67, [8] 1398-1412 (1945).
74. J. H. Becker and H. P. R. Frederikse, "Electrical Properties of Nonstoichiometric Semiconductors," J. Appl. Phys., 33 [1] 447-53 (1962).

Appendix A

COMPUTER PROGRAM FOR RESISTANCE MEASUREMENT

```

10 CLS
20 PRINT "RESISTANCE MEASUREMENT PROGRAM - R(t)  "
30 PRINT "  BY MING-YIH SU ON DEC. 8 1985      "
40 PRINT : PRINT
50 PRINT "THIS PROGRAM IS USED TO :           "
60 PRINT "  1. READ RESISTANCE (R) FROM GENRAD 1658 RLC DIGIBRIDGE "
70 PRINT "  2. CALCULATE CONDUCTIVITY (C) FROM R                "
80 PRINT "  3. SAVE R AND C AS A FUNCTION OF TIME                "
90 PRINT "  4. PRINT RESULTS ON PRINTER                          "
100 PRINT : PRINT
110 DEFINT A-Y
120 DEF SEG = 0 : LIBSEG = VAL("&H" + HEX      (PEEK(1018) + PEEK(1019)*256))
130 FOR LIB = 1 TO 1
140   DEF SEG = LIBSEG
150   ID = PEEK(262) + PEEK(263) * 256 : LENGTH = PEEK(ID)
160   ID   = ""
170   FOR I = 1 TO LENGTH
180     ID   = ID  + CHR(PEEK(ID + I))
190   NEXT I
200   IF ID   = "GP100" THEN GP100 = LIBSEG
210   LIBSEG = VAL("&H" + HEX    (PEEK(254) + PEEK(255) * 256))
220 NEXT LIB
230 IF GP100 = 0 THEN PRINT "Missing GP100 Subroutine Library" : END
240 ' Initialize offsets
250 INIT1 = 256
260 CALL INIT1(INIT2,INIT3,INIT4,INIT5,VERIFY,VERSION,GPRESET,GPNEW,
      GPTIMER,PULSE,HOLD,RTL,RTLHOLD,TONLY,LONLY,EVENT,TRAP,ADDRESS,BUS,
      MESSAGE,TEXT)
270 CALL INIT2(WBYTE,RBYTE,WORD,RWORD,WDWORD,RDWORD,WQWORD,RQWORD,WSTR,
      RSTR,WARRAY,RARRAY,BWRITE,BREAD,WDMA,RDMA,DMA,TERM,NOTERM,CRLF,EOI,
      PARSER)
280 CALL INIT3(CONTROL,IFC,REN,RENCLR,RENLOC,REMOTE,TCS,TCA,STANDBY,LLO,
      DCL,PPU,SPE,SPD,GTL,LOCAL,SDC,GPCLEAR,GPGET,TRIGGER)
290 CALL INIT4(UNLISTEN,UNTALK,MYLISTEN,MYTALK,LISTEN,XLISTEN,ALISTEN,
      TALK,XTALK,BUSCOM,PASS,SPOLL,APOLL,REQUEST,PPOLL,CONFIGURE,RESPONSE,
      MYSTATUS)
300 DIM ZTM(2000),ZR(2000),ZCD(2000),ZTA(2000)
310 INPUT "TOTAL EXPERIMENTAL TIME (MINS) = ";ZTT
320 INPUT "SAMPLING RATE (MINS/DATA) = ";ZRT

```

```

330 INPUT "LENGTH (L) OF SAMPLE (CM) = ";ZLS
340 INPUT "DIAMETER (D) OF SAMPLE (CM) = ";ZDS
350 INPUT "DATA FILE NAME WILL BE : ";F1
360 ZA = 3.14159 * ZDS / 4
370 LPRINT "FILE NAME = ";F1
380 LPRINT
390 LPRINT "TOTAL EXPERIMENTAL TIME = ";ZTT;" MINS"
400 LPRINT "SAMPLING RATE = ";ZRT;" MINS/DATA"
410 LPRINT "LENGTH OF SAMPLE (L) = ";ZLS;" CM"
420 LPRINT "DIAMETER OF SAMPLE (D) = ";ZDS;" CM"
430 LPRINT
440 LPRINT "#";TAB(12);"TIME";TAB(28);"DT(SEC)";TAB(44);"R(OHM)";TAB(60);
    "C /OHM-CM"
450 ZTT = ZTT * 60 : ZRT = ZRT * 60
460 CLS
470 PRINT "EXPERIMENT BEGINS ! DON'T PANIC ! IT IS TAKING DATA NOW !"
480 CALL GPRESET(STATUS)
490 CALL REN(STATUS)
500 CALL IFC(STATUS)
510 '*****
520 '*****  INITIALIZATION OF GenRad 1658 RLC DIGIBRIDGE  *****
530 '*****
540 DEVICE1 = 3 : 'THE ADDRESS OF DIGIBRIDGE IS 3
550 DEF SEG = GP100
555 CALL CRLF
560 INI = "D2S2C0F1L2R4M2X4G0E0"
565 CALL STANDBY(STATUS)
568 CALL LISTEN(DEVICE1,STATUS)
570 CALL MYTALK(STATUS)
590 CALL WSTR(INI ,BYTES,STATUS)
600 I = 0 : K = 0
610 ZTM(0) = TIMER
620 D0 = DATE
630 GOSUB 1040 : 'READ RESISTANCE FROM DIGIBRIDGE
640 ZR(0) = ZR
650 ZCD(0) = ZLS / (ZR * ZA)
660 ZTA(0) = 0
670 PRINT "#";TAB(12);"TIME";TAB(28);"DT(SEC)";TAB(44);"R(OHM)";TAB(60);
    "C /OHM-CM"
680 PRINT I+1;TAB(8);ZTM(I);TAB(24);ZTA(I);TAB(40);ZR(I);TAB(56);ZCD(I)
690 ZTT = ZTM(0) + ZTT
700 ZST = ZTM(0) + ZRT
710 I = I + 1
720 L = ZRT * 50
730 FOR J = 0 TO L
740 NEXT J
750 DT = DATE
760 IF DT = D0 THEN GOTO 780
770 K = K + 1 : D0 = DT
780 ZTM(I) = TIMER + 86400! * K
790 IF ZTM(I) < ZST THEN GOTO 730
800 ZTA(I) = ZTM(I) - ZTM(0)
810 GOSUB 1040 : 'READ RESISTANCE FROM DIGIBRIDGE
820 ZR(I) = ZR

```

```

830 ZCD(I) = ZLS / (ZR(I) * ZA)
840 I1% = I / 20
850 I2 = I - I1% * 20
860 IF I2 <> 0 THEN GOTO 940
870 FOR J = I-20 TO I-1
880 LPRINT J+1;TAB(8);ZTM(J);TAB(24);ZTA(J);TAB(40);ZR(J);TAB(56);ZCD(J)
890 NEXT J
900 CLS
910 PRINT "IT IS TAKING DATA NOW ! PLEASE DO NOT DISTURB !"
920 PRINT
930 PRINT "#";TAB(12);"TIME";TAB(28);"DT(SEC)";TAB(44);"R(OHM)";TAB(60);
    "C /OHM-CM"
940 PRINT I+1;TAB(8);ZTM(I);TAB(24);ZTA(I);TAB(40);ZR(I);TAB(56);ZCD(I)
950 ZST = ZST + ZRT
960 IF ZST < ZTT THEN GOTO 710
970 CALL IFC(STATUS)
980 GOSUB 1200 : 'SAVE DATA INTO DISK
990 GOSUB 1310 : 'PRINT DATA OUT ON PRINTER
1000 END
1010 *****
1020 ***** IEEE-488 ROUTINE FOR DIGIBRIDGE - READ DATA *****
1030 *****
1040 DEF SEG = GP100
1045 CALL UNTALK(STATUS)
1067 CALL GPGET(STATUS)
1070 ZR      = STRING    (20," ")
1075 CALL TALK(DEVICE1,STATUS)
1077 CALL MYLISTEN(STATUS)
1080 CALL RSTR(ZR ,BYTES,STATUS)
1087 CALL UNLISTEN(STATUS)
1090 ZRV = VAL(MID (ZR ,9,7))
1100 UNIT = MID (ZR ,5,2)
1110 IF UNIT = "O" THEN ZRD = 1
1120 IF UNIT = "KO" THEN ZRD = 1000
1130 IF UNIT = "MO" THEN ZRD = 1000000!
1140 ZR = ZRV * ZRD
1150 RETURN
1160 .....
1170 ***** SAVE DATA FILE ROUTINE *****
1180 .....
1190 N = 3 * (I + 1)
1200 CLOSE #1
1210 OPEN F1 FOR OUTPUT AS #1
1220 PRINT #1,N
1230 FOR J = 0 TO I
1240 PRINT #1,ZTA(J),ZR(J),ZCD(J)
1250 NEXT J
1260 CLOSE #1
1270 RETURN
1280 .....
1290 ***** PRINT RESULTS OUT ROUTINE *****
1300 .....
1310 INPUT "DO YOU WANT TO PRINT THE RESULTS OUT (Y/N) ";Q1
1320 IF Q1 = "Y" THEN GOTO 1350

```

```
1330 IF Q1      = "N" THEN RETURN
1340 GOTO 1310
1350 LPRINT "FILE NAME = ";F1
1360 LPRINT
1370 LPRINT "TOTAL EXPERIMENTAL TIME = ";ZTT
1380 LPRINT "SAMPLING RATE = ";ZRT
1390 LPRINT "LENGTH OF SAMPLE (L) = ";ZLS;" CM"
1400 LPRINT "DIAMETER OF SAMPLE (D) = ";ZDS;" CM"
1410 LPRINT
1420 LPRINT "#";TAB(12);"TIME";TAB(28);"DT(SEC)";TAB(44);"R(OHM)";
      TAB(60);"C /OHM-CM"
1430 LPRINT I+1;TAB(8);ZTM(I);TAB(24);ZTA(I);TAB(40);ZR(I);TAB(56);ZCD(I)
1440 RETURN
```

Appendix B

COMPUTER PROGRAM FOR SEEBECK COEFFICIENT MEASUREMENT

```

5 CLS : PRINT
10 PRINT "SEEBECK COEFFICIENT MEASUREMENT PROGRAM"
20 PRINT "    WRITTEN BY MING-YIH SU ON DEC.17 1985"
30 PRINT
40 PRINT "    WHERE E0 -- T0 (ROOM TEMPERATURE) "
50 PRINT "    |         | E1 - T1         "
60 PRINT "    T1 | SAMPLE | T2     E2 - T2         "
70 PRINT "    |         |         DT = T1 - T2         "
80 PRINT "    DV -- VOLTAGE DROP ACROSS
        SAMPLE "
90 PRINT "    TAKE T2 END AS POSITIVE"
100 PRINT "    DV "
110 PRINT "    SEEBECK COEFFICIENT Q = --- (mV/C) "
120 PRINT "    DT         "
130 PRINT
140 PRINT "NOTE 1. THIS PROGRAM AUTOMATICALLY TAKES DATA FROM 1 SYSTEM."
150 PRINT "    2. INPUT FILE NAME WITH DRIVE # ON IT, "
160 PRINT "    i.e. B:F1 for file F1 saved on drive B. "
170 PRINT
180 DEFINT A-Y
190 DEF SEG = 0 : LIBSEG = VAL("&H" + HEX    (PEEK(1018)
    + PEEK(1019) * 256))
200 FOR LIB = 1 TO 1
210   DEF SEG = LIBSEG
220   ID = PEEK(262) + PEEK(263) * 256 : LENGTH = PEEK(ID)
230   ID = ""
240   FOR I = 1 TO LENGTH
250     ID = ID + CHR(PEEK(ID + I))
260   NEXT I
270   IF ID = "GP100" THEN GP100 = LIBSEG
280   LIBSEG = VAL("&H" + HEX    (PEEK(254) + PEEK(255) * 256))
290 NEXT LIB
300 IF GP100 = 0 THEN PRINT "Missing GP100 Subroutine Library" : END
310 ' Initialize offsets
320 INIT1 = 256
330 CALL INIT1(INIT2,INIT3,INIT4,INIT5,VERIFY,VERSION,GPRESET,GPNEW,
    OPTIMER,PULSE,HOLD,RTL,RTLHOLD,TONLY,LONLY,EVENT,TRAP,ADDRESS,
    BUS,MESSAGE,TEXT)
340 CALL INIT2(WBYTE,RBYTE,WORD,RWORD,WDWORD,RDWORD,WQWORD,RQWORD,

```



```

WSTR,RSTR,WARRAY,RARRAY,BWRITE,BREAD,WDMA,RDMA,DMA,TERM,NOTERM,
CRLF,EOI,PARSER)
350 CALL INIT3(CONTROL,IFC,REN,RENCLR,RENLOC,REMOTE,TCS,TCA,STANDBY,
LLO,DCL,PPU,SPE,SPD,GTL,LOCAL,SDC,GPCLEAR,GPGET,TRIGGER)
360 CALL INIT4(UNLISTEN,UNTALK,MYLISTEN,MYTALK,LISTEN,XLISTEN,
ALISTEN,TALK,XTALK,BUSCOM,PASS,SPOLL,APOLL,REQUEST,PPOLL,
CONFIGURE,RESPONSE,MYSTATUS)
370 DIM ZE0(500),ZE1(500),ZE2(500),ZT1(500),ZT2(500),ZDT1(500),ZDV1(500)
400 DIM ZX1(50),ZY1(50)
405 INPUT "SAMPLE NAME = ";SN
410 INPUT "DATA FILE NAME FOR (E0,E1,E2,DV) - SETUP #1 = ";F1
440 INPUT "DATA FILE NAME FOR (DT,DV) - SETUP #1 = ";F1B
470 INPUT "DATA FILE NAME FOR AVERAGED (DT,DV) - SETUP #1 = ";F1C
500 INPUT "SAMPLING RATE (SECONDS/DATA SET) = ";ZRT
510 M = 0
520 J = 0 : 'INDICATOR FOR TOTAL # OF DATA
530 K = 1 : KK = 0 : 'INDICATOR FOR I/O PORT OF SCANNER
540 L = 0 : 'INDICATOR FOR COMPENSATION OF TIMER
550 ZIT = TIMER : 'THE BEGINNING TIME OF EXPERIMENT
560 D0 = DATE
570 ZST = ZIT : 'PRESET DATA TAKING TIME
580 DEVICE1 = 5 : '5 IS THE ADDRESS OF NANOVOLTMETER
590 DEVICE2 = 17 : '17 IS THE ADDRESS OF SCANNER
600 CALL GPRESET(STATUS)
610 CALL REN(STATUS)
620 CALL IFC(STATUS)
630 GOSUB 1540 : 'INITIALIZE NANOVOLTMETER
640 GOSUB 1630 : 'INITIALIZE SCANNER
650 GOSUB 2220 : 'SET I/O PORT TO 0
660 CLS
670 PRINT "EXPERIMENT BEGINS ! DON'T PANIC ! IT IS TAKING DATA NOW !"
680 J = M
690 GOSUB 1720 : 'RESET SCANNER
700 GOSUB 1810 : 'CLEAR BUFFER OF NANOVOLTMETER
710 PRINT "DATA SET";J+1;" ";
720 GOSUB 1910 : GOSUB 1810 : ZE(J) = A!
730 PRINT TAB(20);"E0 = ";ZE0(J)
740 GOSUB 1910 : GOSUB 1810 : ZE1(J) = A!
750 PRINT TAB(20);"E1 = ";ZE1(J)
760 GOSUB 1910 : GOSUB 1810 : ZE2(J) = A!
770 PRINT TAB(20);"E2 = ";ZE2(J)
780 GOSUB 1910 : GOSUB 1810 : ZDV1(J) = A!
790 PRINT TAB(20);"DV1 = ";ZDV1(J)
920 ZJ = J MOD 4
930 IF ZJ = 1 THEN CLS
940 PRINT
950 J = J + 1
960 IF J < M + 10 THEN GOTO 710
970 M = M + 10
980 GOSUB 1910 : 'CHANGE TO CHANNEL #1
990 GOSUB 2040 : 'STOP TRIGGER OF SCANNER
1000 GOSUB 2100 : 'CLOSE CHANNEL #1
1005 GOSUB 2214 : 'RESET I/O PORT TO 000
1006 FOR JJ = 0 TO 4500

```

```

1007 NEXT JJ
1010 K = K + 1 : 'RESET I/O PORT OF SCANNER
1020 IF M = 80 THEN K=1
1030 ON K GOTO 1040,1050,1060,1070,1080,1090,1100,1110,1120,1130
1040 O = "00X" : GOTO 1140
1050 O = "01X" : GOTO 1140
1060 O = "02X" : GOTO 1140
1070 O = "04X" : GOTO 1140
1080 O = "010X" : GOTO 1140
1090 O = "020X" : GOTO 1140
1100 O = "040X" : GOTO 1140
1110 O = "0100X" : GOTO 1140
1120 O = "0200X" : GOTO 1140
1130 O = "0400X" : GOTO 1140
1140 GOSUB 2220 : 'CHANGE I/O PORT OF SCANNER
1150 PRINT : PRINT : PRINT "SAVING DATA FILE (E0,E1,E2,DV) "
1160 GOSUB 2310 : 'SAVE DATA FILE (E0,E1,E2,DV) OF SETUP #1
1190 GOSUB 2640 : 'CALCULATION OF TEMPERATURE FROM VOLTAGE - E TO T
1200 PRINT : PRINT "SAVE DATA FILE (DT,DV) "
1210 GOSUB 3210 : 'SAVE DATA FILE (DT,DV) OF SETUP #1
1240 PRINT : PRINT : PRINT "DOING CALCULATION ! PLEASE WAIT ! "
1250 GOSUB 3720 : 'AVERAGING DATA
1260 GOSUB 4120 : 'SAVE AVERAGED DATA FILE (DT,DV) OF SETUP #1
1281 GOSUB 5150 : 'PRINT DATA OF SETUP #1 OUT
1290 IF M < 40 THEN GOTO 1340
1300 GOSUB 4420 : 'LEAST SQUARE ANALYSIS
1310 GOSUB 4690 : 'CALCULATE R FACTOR
1320 GOSUB 4870 : 'PRINT RESULTS ON SCREEN
1321 GOSUB 5700 : 'PRINT FINAL RESULTS OUT - SETUP #1
1330 IF M = 80 THEN GOTO 1530
1340 ZST = ZST + ZRT
1350 DT = DATE
1360 IF DT = D0 THEN GOTO 1380
1370 L = L + 1 : D0 = DT
1380 ZTIME = TIMER + L * 86400!
1390 ZST2 = ZST - L * 86400!
1400 ZSHR = ZST2 / 3600 : SHR = FIX(ZSHR)
1410 ZSMN = (ZST2 - SHR * 3600) / 60 : SMN = FIX(ZSMN)
1420 SSEC = ZST2 - SHR * 3600 - SMN * 60
1430 ZST = STR(SHR) + "." + RIGHT (STR (SMN),2) + "."
      + RIGHT (STR (SSEC),2)
1440 CLS
1450 PRINT
1460 PRINT "NEXT DATA TAKING TIME =" : ZST
1470 PRINT
1480 PRINT "      CURRENT TIME =" : TIME
1490 IF ZTIME > ZST THEN GOTO 660
1500 FOR JJ = 0 TO 3000
1510 NEXT JJ
1520 GOTO 1350
1530 END
1540 .....
1550 ..... IEEE-488 ROUTINE FOR INITIALIZATION OF NANOVOLTMETER .....
1560 .....

```

```

1570 DEF SEG = GP100
1580 COMINI1 = "R2M0T0P0D0Z0B0K0X"
1590 CALL MYTALK(STATUS)
1600 CALL LISTEN(DEVICE1,STATUS)
1610 CALL WSTR(COMINI1 ,BYTE3,STATUS)
1620 RETURN
1630 *****
1640 ***** IEEE-488 ROUTINE FOR INITIALIZATION OF SCANNER *****
1650 *****
1660 DEF SEG = GP100
1670 COMINI2 = "D0F1L4W010.000P0T2X"
1680 CALL MYTALK(STATUS)
1690 CALL LISTEN(DEVICE2,STATUS)
1700 CALL WSTR(COMINI2 ,BYTES,STATUS)
1710 RETURN
1720 *****
1730 ***** IEEE-488 ROUTINE FOR SCANNER — RESET SCANNER *****
1740 *****
1750 DEF SEG = GP100
1760 COMRST2 = "RX"
1770 CALL MYTALK(STATUS)
1780 CALL LISTEN(DEVICE2,STATUS)
1790 CALL WSTR(COMRST2 ,BYTES,STATUS)
1800 RETURN
1810 *****
1820 ***** IEEE-488 ROUTINE FOR NANOVOLTMETER — READ DATA *****
1830 *****
1840 DEF SEG = GP100
1850 CALL TALK(DEVICE1,STATUS)
1860 CALL MYLISTEN(STATUS)
1870 A = STRING (16," ")
1880 CALL RSTR(A ,BYTES,STATUS)
1890 A! = VAL(MID (A ,5,12))
1900 RETURN
1910 *****
1920 ***** IEEE-488 ROUTINE FOR SCANNER — CHANGE CHENNEL *****
1930 *****
1940 DEF SEG = GP100
1950 CALL GPGET(STATUS)
1960 S = STRING (20," ")
1970 CALL RSTR(S ,BYTES,STATUS)
1980 FOR JJ = 0 TO 300
1990 NEXT JJ
2000 RETURN
2010 *****
2020 ***** IEEE-488 ROUTINE FOR SCANNER — STOP SCAN *****
2030 *****
2040 DEF SEG = GP100
2050 T = "T3X"
2060 CALL MYTALK(STATUS)
2070 CALL LISTEN(DEVICE2,STATUS)
2080 CALL WSTR(T ,BYTES,STATUS)
2090 CALL GPGET(STATUS)
2100 S = STRING (20," ")

```

```

2110 CALL RSTR(S ,BYTES,STATUS)
2120 RETURN
2130 '*****
2140 '***** IEEE-488 ROUTINE FOR SCANNER - CLOSE CHANNEL #1 ,MEASURE TO
2150 '*****
2160 DEF SEG = GP100
2170 CALL MYTALK(STATUS)
2180 CALL LISTEN(DEVICE2,STATUS)
2190 CHANEL1 = "B1C1X"
2200 CALL WSTR(CHANEL1 ,BYTES,STATUS)
2210 RETURN
2211 '*****
2212 '***** IEEE-488 ROUTINEFOR SCANNER - RESET I/O PORT TO 000 *****
2213 '*****
2214 DEF SEG = GP100
2215 O = "00X"
2216 CALL MYTALK(STATUS)
2217 CALL LISTEN(DEVICE2,STATUS)
2218 CALL WSTR(O ,BYTES,STATUS)
2219 RETURN
2220 '*****
2230 '***** IEEE-488 ROUTINE FOR SCANNER - RESET I/O PORT *****
2240 '*****
2250 DEF SEG = GP100
2270 CALL MYTALK(STATUS)
2280 CALL LISTEN(DEVICE2,STATUS)
2290 CALL WSTR(O ,BYTES,STATUS)
2300 RETURN
2310 '*****
2320 '***** SAVE DATA FILE (E0,E1,E2,DV) OF SETUP #1 ROUTINE *****
2330 '*****
2340 N = M * 4
2350 OPEN F1 :OR OUTPUT AS #1
2360 PRINT #1,N
2370 FOR J = 0 TO M-1
2380 PRINT #1,ZE0(J);ZE1(J);ZE2(J);ZDV1(J)
2390 NEXT J
2400 CLOSE #1
2410 RETURN
2640 '*****
2660 '***** E TO T CALCULATION ROUTINE *****
2660 '*****
2670 PRINT : PRINT "DOING CALCULATION ! PLEASE WAIT ! "
2680 A0# = 0
2690 A1# = 5.3994446#
2700 A2# = .012467754#
2710 A3# = -.000019934168#
2720 A4# = 0
2730 ZT0 = 0
2740 FOR J = M - 10 TO M - 1
2750 ZT0 = ZE0(J) * 1000#
2760 ZT0 = 30# - ZT0
2770 ZV0 = A0# + A1# * ZT0 + A2# * (ZT0) + A3# * (ZT0)
      + A4# * (ZT0)

```

```

2780 ZV1 = ZV0 + ZE1(J) * 1000000!
2790 ZV2 = ZV0 + ZE2(J) * 1000000!
2800 GOSUB 3030 : 'CHOOSE B COEFFICIENT
2810 IF ZV1 < 10165 OR ZV2 < 10165 THEN GOSUB 3120
2820 ZT1(J) = B0# + B1# * ZV1 + B2# * (ZV2) + B3# * (ZV3)
      + B4# * (ZV4)
2830 ZT2(J) = B0# + B1# * ZV2 + B2# * (ZV2) + B3# * (ZV3)
      + B4# * (ZV2)
2840 ZDT1(J) = ZT1(J) - ZT2(J)
3010 NEXT J
3020 RETURN
3030 '*****
3040 '***** B0,B1,B2,B3,B4 FOR T > 1050 C *****
3050 '*****
3060 B0# = -30.938374#
3070 B1# = .1410656#
3080 B2# = -.0000049794442#
3090 B3# = 1.7334256D-10
3100 B4# = -1.926216D-15
3110 RETURN
3120 '*****
3130 '***** B0,B1,B2,B3,B4 FOR T < 1050 C *****
3140 '*****
3150 B0# = 41.137317#
3160 B1# = .11599785#
3170 B2# = -.0000018642979#
3180 B3# = 1.2643267D-11
3190 B4# = 8.4828836D-16
3200 RETURN
3210 '*****
3220 '***** SAVE DATA FILE (DT,DV) OF SETUP #1 ROUTINE *****
3230 '*****
3240 N = M * 2
3250 OPEN F1B FOR OUTPUT AS #1
3260 PRINT #1,N
3270 FOR J = 0 TO M-1
3280 PRINT #1,ZDT1(J);ZDV1(J)
3290 NEXT J
3300 CLOSE #1
3310 CLS
3320 PRINT "SETUP #1 " : PRINT
3330 PRINT " #";TAB(12);"T1";TAB(28);"T2";TAB(44);"DT";TAB(60);"DV"
3340 FOR J = M - 10 TO M - 1
3350 PRINT J + 1;TAB(8);ZT1(J);TAB(24);ZT2(J);TAB(40);ZDT1(J);TAB(56);
      ZDV1(J)
3360 NEXT J
3370 RETURN
3720 '*****
3730 '***** AVERAGING 10 DATA INTO 1 ROUTINE *****
3740 '*****
3750 I = 10 : MM = M / 10 : NN = 0
3760 FOR II = 0 TO MM-1
3770 ZX1(II) = 0
3780 ZY1(II) = 0

```

```

3790 FOR JJ = NN TO NN + I - 1
3800 ZX1(IJ) = ZX1(IJ) + ZDT1(JJ)
3830 ZY1(IJ) = ZY1(IJ) + ZDV1(JJ)
3860 NEXT JJ
3870 NN = JJ
3880 ZX1(IJ) = ZX1(IJ) / I
3910 ZY1(IJ) = ZY1(IJ) / I
3940 NEXT IJ
3950 CLS
3960 PRINT "SETUP #1 ";
3970 FOR II = 0 TO MM - 1
3980 PRINT TAB(20); "DT = "; ZX1(II); "DV = "; ZY1(II)
3990 NEXT II
4080 RETURN
4090 *****
4100 ***** SAVE AVERAGED DATA FILE (DT,DV) OF SETUP #1 ROUTINE *****
4110 *****
4120 OPEN F1C FOR OUTPUT AS #1
4130 PRINT #1,MM
4140 FOR J = 0 TO MM-1
4150 PRINT #1,ZX1(J),ZY1(J)
4160 NEXT J
4170 CLOSE #1
4180 RETURN
4390 *****
4400 ***** LEAST SQUARE ANALYSIS *****
4410 *****
4420 U1! = 0 : U2! = 0
4430 V1! = 0 : V2! = 0
4480 FOR II = 0 TO MM-1
4490 U1! = U1! + ZX1(II)
4500 V1! = V1! + ZY1(II)
4510 U2! = U2! + ZX1(II) * ZX1(II)
4520 V2! = V2! + ZX1(II) * ZY1(II)
4610 NEXT II
4620 A1! = (V2! - U1! * V1! / MM) / (U2! - U1! * U1! / MM)
4650 B1! = (V1! - A1! * U1!) / MM
4680 RETURN
4690 *****
4700 ***** CALCULATION OF R FACTOR ROUTINE *****
4710 *****
4720 U1! = 0 : U2! = 0
4750 FOR II = 0 TO MM-1
4760 U1! = U1! + (ZY1(II) - A1! * ZX1(II) - B1!)
4770 U2! = U2! + (A1! * ZX1(II) + B1! - V1!) / MM
4820 NEXT II
4825 IF U1! > U2! THEN R1! = 9999 : GOTO 4860
4830 R1! = SGN(B1!) * SQR(1 - U1! / U2!)
4860 RETURN
4870 *****
4880 ***** PRINT RESULTS ON SCREEN ROUTINE *****
4890 *****
4900 C1! = -B1! / A1! : Q1! = A1! * 1000
4930 CLS

```

```

4940 PRINT "SETUP #1 : ","EQUATION : DV = B + A * DT "
4950 PRINT TAB(24);"A = ";A1!
4960 PRINT TAB(24);"B = ";B1!
4970 PRINT TAB(24);"DT(0) = ";C1!
4980 PRINT TAB(24);"R = ";R1!;"Q = ";Q1!;"mV/C"
5110 RETURN
5120 '*****
5130 '***** PRINT DATA OF SETUP #1 OUT ON PRINTER ROUTINE *****
5140 '*****
5150 LPRINT TAB(10);"SETUP #1",DATE ,TIME ,F1
5155 LPRINT TAB(10);"SAMPLE NAME = ";SN
5160 LPRINT
5170 LPRINT TAB(10);" #";TAB(22);"E0";TAB(38);"E1";TAB(54);"E2";
      TAB(70);"DV"
5180 FOR J = M - 10 TO M - 1
5190 LPRINT TAB(10);J+1;TAB(18);ZE0(J);TAB(34);ZE1(J);TAB(50);
      ZE2(J);TAB(66);ZDV1(J)
5200 NEXT J
5210 LPRINT
5220 LPRINT TAB(10);" #";TAB(22);"T1";TAB(38);"T2";TAB(54);"DT";
      TAB(70);"DV"
5230 FOR J = M - 10 TO M - 1
5240 LPRINT TAB(10);J+1;TAB(18);ZT1(J);TAB(34);ZT2(J);TAB(50);ZDT1(J);
      TAB(66);ZDV1(J)
5250 NEXT J
5260 LPRINT
5270 LPRINT TAB(20);"DT = ";ZX1(MM-1);"DV = ";ZY1(MM-1)
5280 LPRINT : LPRINT : LPRINT
5290 RETURN
5670 '*****
5680 '***** PRINT FINAL RESULTS OUT ROUTINE - SETUP #1 *****
5690 '*****
5700 LPRINT TAB(10);"SETUP #1",DATE ,TIME ,F1
5705 LPRINT TAB(10);"SAMPLE NAME = ";SN
5710 LPRINT
5720 FOR II = 0 TO MM - 1
5730 LPRINT TAB(20);"DT = ";ZX1(II);"DV = ";ZY1(II)
5740 NEXT II
5750 LPRINT
5760 LPRINT TAB(10);"EQUATION : DV = B + A * DT "
5770 LPRINT TAB(24);"A = ";A1!
5780 LPRINT TAB(24);"B = ";B1!
5790 LPRINT TAB(24);"DT(0) = ";C1!
5800 LPRINT TAB(24);"R = ";R1!;"Q = ";Q1!;"mV/C"
5810 LPRINT : LPRINT
5820 RETURN

```